FABRICATION OF A WEDGE SHAPED MID-LINE BLOCK AND THE STUDY OF ITS CHARACTERISTICS

MASTER OF PHILOSOPHY
THESIS

Supervised by

Professor Dr.Md.Adnan Kiber
DEPARTMENT OF APPLIED PHYSICS & ELECTRONICS
UNIVERSITY OF DHAKA
(FORMER ASSOCIATE PROFESSOR DEPARTMENT OF PHYSICS UNIVERSITY OF DHAKA)

Submitted by

Alok kumar dey
Exam.Roll No.: 10
Registration No.: 279
Session: 1997-1998

পদার্থ বিজ্ঞান বিভাগ
ঢাকা বিশ্ববিদ্যালয়
ঢাকা-১০০০, বাংলাদেশ
ফোন : ৯৬৬১৯২০/৪৯৪২
ফ্যাক্স : ৮৬১৫৫৮৩

DEPARTMENT OF PHYSICS
UNIVERSITY OF DHAKA
DHAKA-1000, BANGLADESH
Phone : +880-2-9661920 Ext. 4942
Fax : +880-2-8615583
E-mail : physics@univdhaka.edu

DECLARATION

This is to certify that Alok Kumar Dey has written the thesis titled "Fabrication of a wedge shaped mid-line block and the study of its characteristics." under my direct supervision. He has written the thesis of his M. Phil. degree on Physics.

I have gone through the thesis thoroughly and am recommending its examination by the appropriate authorities.

I further affirm that the work reported in this thesis is original and no part or whole of the dissertation has been submitted to, any form in any other University or institution for any degree.

Adnan 25/6/05

Supervisor

Dated : 25/06/2005

Prof. Dr, Md. Adnan Kiber
Department of Applied Physics & Electronics
University of Dhaka (Former associate professor
Department of Physics University of Dhaka)

Dedicated
To
My Elder Brother & Late Parents

ACKNOWLEDGEMENT

At the very beginning, I would like to acknowledge my deep sense of gratitude to my supervisor Dr.Md. Adnan Kiber, Professor Department of Applied Physics & Electronics University of Dhaka (Former Associate Professor, Department of Physics, University of Dhaka) for constant guidance, valuable advice, encouragement and keen supervision throughout this research work which pave the way to complete my thesis.

I am very much grateful to Dr. Syed Raza Hussain, Chief Physicist, Delta Medical Center Ltd. Dhaka, and express my thankfulness for his encouragement and valuable suggestions and help.

With full gratitude and respect I would like to acknowledge Dr. Khondkar Siddique-e-Rabbani, Professor, Department of Physics University of Dhaka, for his suggestion and encouragement all through this research work.

With a grateful heart I would like to acknowledge to Mr. Jahangir Alam, Medical Physicist, Delta Medical Center Ltd. Dhaka for his great contribution during carrying out my work. In a true sense, I would like to express that without his direct help I can't finish my thesis work at all.

I would also like to express my gratefulness to Mr. Rafi Uddin Lecturer, Department of Physics, Bangladesh University of Engineering & Technology (BUET) for helping.

I am very grateful to my intimate friends, such as, Nasrul, Noman, Iqubal Mamun, Shahin and Saiful who have mentally inspired me to accomplish my research work.

I would like to extend my grateful thanks to the staffs and technicians of Delta Medical Center Ltd. Dhaka who have helped me during my working period. I would like to give thankfulness specially technicians, named Md. Rashed ul Islam, Suraya Begum and Md. Sajder Hossain.

From the core of my heart I would like to thank my friend Emon Nir for his inspiration and help about my thesis work.

Above all I am grateful to my whole family, especially to my two elder brothers Kamal Kanti & Dipak Dey for their continuous mental support and inspiration to continue my thesis work.

Abstract

Cervical cancer is common among female in Bangladesh. Radiotherapy is one of the important and widely used modality for the treatment of this cancer. Uniform dose delivery is very essential for the treatment. The main goal is to deliver the maximum dose at the cancer affected areas and the minimum dose below the tolerance level in the surrounding normal tissues like rectum and urinary bladder. So proper planning is very important to accomplish this critical task.

This planning is often challenging because the different organs like rectum and urinary bladder of this area have different radiation tolerance levels. To overcome this problem, a block named "wedge shaped mid-line block"(WMLB) is proposed to use for the treatment of cervix cancer. WMLB stops the radiation dose up to position "A" in the cervix and delivers optimum dose to the parametrium and the distance between points "A" to "B". Point A is defined to be 2 cm superior to the external cervical os and 2 cm lateral to the cervical canal. Point B is defined 3 cm lateral to point A.

The wedge shaped mid-line block consists of a rectangular block at center and wedge shaped slope on both sides. The central rectangular portion with an area 10×4cm² and thickness of 5.5 HVLS (Half value layer surface) ensure nearly 100% shielding up to point A and the wedge shaped portion from point A to point B on both sides of the uterine canal gives an overall area of 10×10cm² at 80 cm source to surface distance (SSD). Beyond the point B and up to the edge of the beam, there is no shielding, since the contribution of intracavitary dose is minimal. Conventional rectangular block shields the rectum area and urinary bladder; the resultant dose fall off is very rapid beyond point A. To overcome this problem, "Wedge shaped Mid-line

Block"(WMLB) is used to protect the unnecessary central axis radiation dose to the critical organs.

We have fabricated a "wedge shaped mid-line block" in our laboratory. We made a Styrofoam image of the block by a block cutter (styroformer). This image was placed on a plane table and covered by some thin wet plaster of Paris except at bottom. After it had hardened, the foam image was removed and a negative image of the block was made. Then the molten alloy (lead, tungsten and tin alloy, having melting point of 70°C) was poured into it and allowed it to harden. In this way the "Wedge Shaped Mid-Line Block" (WMLB) was fabricated.

In developed countries, expensive Multi leaf collimators Co_{60} machine is used which have beam-modifying system and the beam is controlled by a computer. In developing countries like us, single leaf collimator Co_{60} machine is used, as it is relatively cheap. Single leaf machine requires different types of block shielding to control the shape and intensity of the irradiating beam as required.

We studied and characterized the response and distribution of dose delivery of the fabricated WMLB for Co_{60} irradiating gamma beam. The dose measured by a 0.6cc Farmer ion chamber and measured with a PTW UNIDOSE electrometer. We studied the dose distribution for different field size (10×10,15×15,20×20 and 25×25) for open field scanning and isodose curve was found as expected. We also studied the block field scanning and found 96% attenuation up to point A, which is a good result.

CONTENTS

Chapter 1

Chapter 2

Chapter 3

Chapter 4

Chapter 5

5. Materials and Methods

Chapter 6

6. Results and Discussion

Chapter 1

1. Introduction

Chapter 1

1.Introduction

1.1 General

Physics has been playing a vital role for the creation of modern civilization. This basic science now possesses numerous well-established branches, which deal with non-living objects. The capability of sequential logical analysis, the flexibility of sorting out of any complicated problem and approach to the interpretation of any physical mechanism with deep inside, physics has extended its branches in the field of life science. Biophysics and medical physics are the two main branches of physics in life science, which involves in the understanding the basic physical activities and rules of different health and diseased conditions in the body and thus helping in designing suitable methods and instruments for diagnosis and therapy.

It can be argued that the start of Radiotherapy was Rontgen's discovery of x-rays since that was directly linked to Becquerels discovery of radioactivity which in turn led to the discovery of radium by Marie and Pierre Curie. This was followed in 1901 by Pierre curies self-exposure experiment (the first Brachytherapy radiobiology) devised following Becquerels accidental radium burn and Pierre Curies analysis of this event as being similar to an x-ray burn. Radiotherapy treatment started from these discoveries and incidents [1].

Radiation therapy is used for the treatment of cancer. Cancer is a critical disease. There are different types of cancers occurs in different parts or organs in the body. Some of them are incurable and some are curable with the respect of their stage and position by using radiotherapy, chemotherapy and surgery where necessary. After chemotherapy and surgery, radiation therapy is used for completing the treatment (if malignant sell is spread). Furthermore, radiation therapy is alone used for many cases. For this purpose Gamma radiation and X-rays are used. Gamma radiation and X-rays are electromagnetic wave, which has long-term biological effect in

human body. Again it is used for the treatment of cancer. So extreme care have to include in the treatment planning. This work is to develop a treatment planning protocol for the treatment of the cervical region cancer for cervix cancer patients with special reference to Bangladeshi population.

Cervical cancer is the second commonest female cancer worldwide with almost more than half a million cases per annum [1]. In many developing countries it is the commonest cancer in females with a five-year survival rate of only 20% to 30% whilst in developed countries it is 50% [1]. The spread of cervical cancer is by local invasion and via the lymphatic system to pelvic and para-aortic nodes. Therefore, this disease should be amenable to loco-regional therapy by surgery or radiotherapy or combination.

Uniform dose delivery to the treatment volume is prerequisite for effective management of cancer by radiotherapy. The main goal is to give maximum dose at lesions (tumor volume) and the minimum dose (below the tolerance level) in surrounding normal tissues. Otherwise, the normal tissues by which buildup non-malignant regions or organs will be affected and may get damaged. As a result many side effect should occur and patient may die. So it is essential to measure the dose at tumor position and normal tissue position to achieve the goal.

Therefore, before treating cervix cancer or malignant lesion with radiation, a proper plan for determining the best method of delivering radiation dose to the tumor is mandatory. The aim of the treatment planning is to ensure that the tumor receives a uniform radiation dose while healthy normal tissue and normal critical structures receives as low dose as possible (below the tolerance level).

For this critical job at first one needs to determine accurately the tumor volume or malignant tissue volume which is to be treated and then design the appropriate radiation fields for delivering radiation to that volume. This planning is often a challenging process; to treat the tumor

volume it is required in achieving an optimum and reproducible data for radiation treatment technique. The dose distribution in the treatment volume should be as homogeneous as possible which sufficiently minimize the radiation dose to the surrounding healthy tissue.

Accurate patient dosimetry i.e. planning is only possible when sufficiently accurate dosimetric data are available from the experimental measurements. Such data collection includes body contour outline, density of relevant internal structures, location and extent of the target volume. Acquisition of these data is necessary whether the dosimetric calculations are performed with a computer or manually. To avoid undesirable radiation hazard in normal tissue position and for getting more accurate dose at the tumor volume is the key point of the proposed research project.

1.2 Aim of the present study

We want to develop a treatment planning protocol to treat cervical cancer patients. It is difficult, because the different organs of this area have different radiation tolerance level. So teletherapy and brachytherapy is generally used to treat cervical cancer. The dose optimization to the fornix and the parametrium region are basic requirement of the treatment planning. Fornix's is an organ, which can tolerate the high dose like 140Gy but the radical dose of the parametrium is only 50Gy. So, to minimize the dose distribution to the respective organ both teletherapy and brachytherapy irradiation is necessary. Brachytherapy is a tool of irradiation, which can deliver high dose to a short distance. Due to anatomical structure, parametrium cannot be treated by brachytherapy with required dose.

Now a days, wedge shaped mid-line block is being used during teletherapy, which stops the radiation dose up to position "A" in the cervix and delivers optimum dose to the parametrium and the distance between points "A" to "B". Point A is defined to be 2 cm superior to the external

cervical os and 2 cm lateral to the cervical canal. Point B is defined 3 cm lateral to point A. The dose to the fornix is delivered by two insertions of brachytherapy depending on the stage of the cancer [2].

The wedge shaped mid-line block consists of a rectangular block at center and wedge shaped slope on the sides. The central rectangular portion with an area 10×4cm² and thickness of 5.5 HVLS (Half value layer surface) ensure nearly 100% shielding up to point A the wedge shaped portion from point A to point B on both sides of the uterine canal gives an overall area of 10×10cm² at 80 cm source to surface distance (SSD). Beyond the point B and up to the edge of the beam, there is no shielding, since the contribution of intracavitary dose is minimal. To estimate the thickness of the block between point A and B a lateral 100% dose profile was generated for Fletcher- Suit applicator [2] at point A level using computer. The fall off of dose between point A and B was estimated in percentage by normalizing the point A dose to100%. The thickness of the alloy block required for external beam in order to compensate the fall off of dose.

Conventional rectangular block shields the rectum area and urinary bladder; the resultant dose fall off is very rapid beyond point A. To overcome this problem, "Wedge shaped Mid-line Block"(WMLB) is used to protect the unnecessary central axis radiation dose to the critical organ. The dose limitation of the rectum (anal canal) and bladder region should be maintained by using the newly developed idea for the treatment protocol. After using WMLB, intracavitary therapy will be necessary for completing the treatment. The aim of the work is to design and fabricate a wedge shaped mid-line block and study its radiation absorption characteristics and dosimetric measurements for a standard data for the treatment in Bangladesh.

1.3 Previous Works

Many scientists have worked many different ways to treat the gynecological cancer patients. Their system was different but goal was the same. Some of the previous works, which are most relevant to the present study, are discussed in the subsequent pages.

Cunningham and et.al [3] evaluated the rectal, rectosigmoidal and bladder doses from intracavitary brachytherapy in the treatment of carcinoma of the cervix. Contrast radiography on a radiography simulator was used to image the rectum and bladder and dose rates were determined at predesignated reference points with the aid of computer calculated dose distributions. Forty-three patients have been reviewed in order to ascertain the correlation between radiation injury and dose at reference points in the rectum and bladder.

Alecu and Alecu [4] measured the in-vivo rectal dose with diodes to avoid misadministration during intracavitary high dose rate brachytherapy for carcinoma of the cervix. A device containing an energy compensated silicon diode was specially designed for these measurements. During the treatment planning process the rectal points are identified by means of the three dimensional TPS. Just before treatment delivery, the diodes mounted on the plastic rod are inserted within the rectal marker, making sure that the tip of the rod coincides with the end of the marker. During treatment the diode readings are monitored. Measurements have been performed for 50 treatments delivered with a Fletcher-Suit-Delclos applicator. In order to validate *in vivo* dosimetry program, measurements in phantom have also been performed for intracavitary implants with different configurations of the FSD applicator, i.e. different intrauterine tandems and ovoids as well as various dwell positions and time patterns. A pelvic phantom was designed and fabricated out of a tissue equivalent material. The applicator and the

rectal marker have been inserted into the phantom at the same relative positions.

Mohan et.al. [5] have computed the radiation dose distributions for shielded cervical applicators. For shielded sources, because of a lack of symmetry and because of a rapid variation of dose as a function of position relative to the source, extensive measured data in three dimensions are required. They have developed the dose at a given point from a source in a shielded ovoid was calculated by multiplying the dose from an unshielded source by the "effective attenuation factor" of the shields. The unshielded-source data was calculated which is the product of source strength and time of implant, distance dependent geometry factor and a tabulated quantity called the "relative dose rate factor". Relative dose-rate factor was obtained by dividing measured dose rate by the product of geometry factor and source strength.

Weeks [6] determined the dose distribution for an ovoid with tungsten shielding designed using Monte Carlo simulation. Standard ^{137}Cs tube source, tungsten shielding and aluminum ovoid applicators were each modeled as a collection of solid objects. Dose was calculated in planes above, below, in front of and on the sides of the colpostat. The Monte Carlo results were compared with the results from a parameterized calculation algorithm and good agreement was obtained. The dose distribution matrix derived from the parameterized algorithm can be used for clinical treatment planning.

Muench and Nath [7] measured the dose distributions produced by shielded applicators using ^{241}Am for intracavitary irradiation of tumors in the vagina. In this dosimetry study four source configurations for a vaginal applicator have been investigated in detail. These configurations were: (i) a 5Ci applicator that contains one 5Ci source, (ii) a 5-5Ci applicator that contains two 5Ci sources adjacent to each other (iii) a 5-4-5Ci applicator which contains a 5Ci source next to a center line containing two 2Ci

sources, following by another 5Ci source on the other side of the center line, all in a plane, (iv) a 5-5-5Ci applicator which contains three 5Ci sources adjacent to one another in a plane. Dose rates at various points around the ^{241}Am sources were measured using a lithium fluoride (LiF) thermoluminescence dosimetry (TLD) system. For this experiment LiF chips were placed in shallow (0.48cm diameter and 0.1cm deep) holes drilled in a solid water phantom. In a typical experiment ~80 TLD chips were placed in a 20cm×20cm solid water sheet and irradiated. This sheet was part of a 20cm tall stack of 20cm×20cm solid water sheets. Against one side of the stake was placed a water filled, solid water walled tank in which ^{241}Am sources were mounted. At least 8cm of scattering material (water or solid water) was present in all directions around the source. For each source configuration dose distributions in two orthogonal planes were measured. The experiment for each plane was repeated up to three times to achieve better statistical accuracy.

Palta et.al. [8] have studied the dosimetric characterization of the 18-MV photon beam from the Semen's Mevatron 77 linear accelerator. Percentage depth dose, dose in the build up region, field size dependence of output, transmission through lead, tray attenuation, and isodose curves for the open and wedged fields were measured using an ionization chamber in water and polystyrene phantoms. A two-piece filter made from stainless steel and tungsten is used to flatten the x-ray beam over the complete range of field sizes available on the machine (2×2 to 40×40cm^2). All water phantom measurements were made using a computer-controlled data acquisition system. The system consists of a water phantom, two-dimensional scanner, ionization chamber, and computer/controller. A 0.1cm^3 air gas, cylindrical ionization chamber, PTW 30-350, was used for all the in-water measurements. Depth dose in the buildup region, between the surface and the depth of maximum dose, were measured in a polystyrene phantom using

a PTW 30-330 parallel plate ionization chamber (1.5mm plate separation) with a Keithley 602 electrometer.

Krithivas and Rao [9] had studied the dosimetric characteristics of a 24-MV x-ray from a Varian Clinec 2500 linear accelerator. Particular attention was paid for measurements and applications relating to depth of maximum dose and scatter correction factors. Scatter factors were determined for field sizes ranging from 5×5 to 40×40cm^2 [Phantoms of various sizes and materials and a variety of detectors were used throughout the investigations]. The following measurements were used for collecting the data; (1) water phantom scatter (model RFA-3, Therades, Sweden); (2) acrylic (density=1.198 g/cm^3) and Sub-committee on Radiation Dosimetry (SCRAD) type polytyrene (density=1.05 g/cm^3) phantoms; (3) silicon diode (part of RFA-3 above) and Physikalische-Technische Werkstatten (PTW model 30-350, nuclear Associates, Inc) and Farmer-type (NEL-2505) ion chambers of collecting volumes 0.1 and 0.6cm^3, respectively; and (4) keithley model 614 electrometer.

Chapter 2

2. Anatomical importance of Cervix Region and its surroundings

Chapter 2

2. Anatomical importance of cervix region

2.1 Introduction

Cervical cancer is the second common female cancer. High dose radiation field is used for the treatment of this cancer. For the effective result the dose should be uniform and radiate to the tumor volume only. The main goal is maximum dose at lesions (tumor volume) and minimum dose (below the tolerance level) in surrounding normal tissues and vital organs like rectum and urinary bladder. So it is very essential to know the anatomical structure of the cervix region and surrounding critical organs.

Before the treatment, a proper plan is necessary which ensure the best method of delivering radiation to the tumor volume. The aim of the treatment plan is to ensure that the tumor receives a uniform radiation dose while healthy tissue and surrounding critical structures receives as low dose as possible. For creating a proper plan we have to know the anatomical structure of the affected organ and also to know the surrounding anatomical structure.

2.2 Anatomical structure of the uterine cervix

The cervix uteri are about 2.5 cm in length; it is narrower and hence more cylindrical than the body, and is a little wider in the middle than above or below. Owing to its relationships it is less freely moveable than the body, so that its long axis and that of body are seldom in the same straight line. The long axis of the uterus as a whole represents the form of a curved line with its concavity forward, and the organ is described as being anteflexed. In extreme cases there may be an angular bend at the region of the internal os – acute anteflexion. When the bladder is empty the long axis of the cervix meets the long axis of the vagina at an angle, which faces antero—inferiorly, and the whole uterus is therefore turned anteriorly on the vagina, or anteverted.

The cervix projects through the anterior wall of the vagina, which divides it into upper, supravaginal and lower vaginal regions (fig 2.1).

The supravaginal part of the cervix is separated in front from the bladder by cellular connective tissue, the parametrium, which extends also on to the sides of the cervix, and laterally between the layers of the broad ligaments. The uterine arteries reach the lateral aspects of the cervix in this tissue, whilst on each side the ureter runs downwards and forwards in it at a distance of about 2 cm from the cervix. The relationship of the arteries and the ureters is not always symmetrical, and in particular one or other of the ureters may be somewhat anterior to the cervix. Posteriorly the supravaginal cervix is covered with peritoneum, which is prolonged below on to the posterior vaginal wall, whence it is reflected to the rectum, forming the recto-uterine pouch (fig 2.1). It is in relation with the rectum, from which it may be separated by the terminal coil of the ileum.

The vaginal part of the cervix projects into the anterior wall of the vagina forming the vaginal fornix's (fig 2.1). On its projecting rounded extremity there is a small, depressed, circular aperture, the external os of the uterus, through which the cavity of the cervix communicates with that of the vagina. In woman who have borne children the external os is bounded by two lips, anterior and posterior, of which the anterior is the shorter and thicker, although, because of the slope of the cervix, it projects lower than the posterior. Normally both lips are in contact with the posterior vaginal wall.

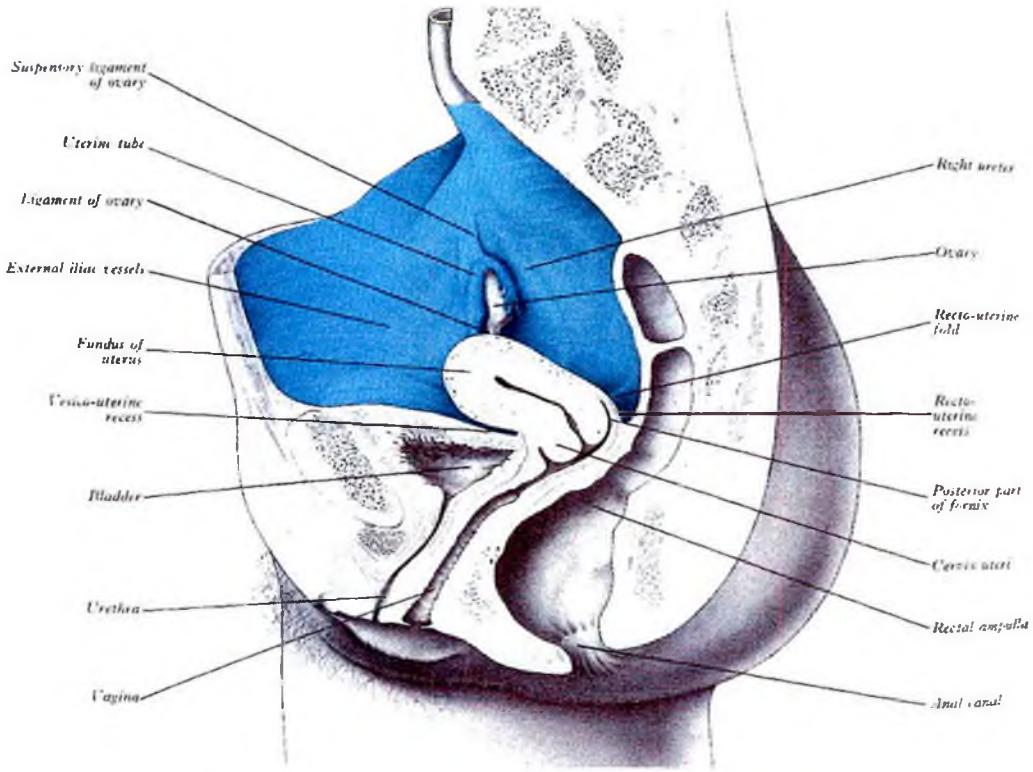

Fig. 2.1 A medial sagittal section through a human female pelvis. The peritoneum is shown in blue.

The cavity of the uterus (fig 2.2) is small in comparison with the size of the organ, partly due to its thick wall.

The cavity of the body is a mere slit in sagittal section because the anterior and posterior walls are almost in contact. In coronal section it is seen to be triangular in shape, the base being formed by the internal surface of the fundus between the orifices of the uterine tubes, the apex by the internal os of the uterus; through this orifice the cavity of the body communicates with the canal of the cervix.

The canal of the cervix is somewhat fusiform, flattened from before backwards, and broader in the middle than at the ends. It communicates above, through the internal os, with the cavity of the body, and below,

feature of both the anterior and posterior walls of the canal and from each a number of small oblique palmate folds ascend laterally, giving the appearance of branches from the stem of a free (arbor vitae uteri). The folds on the two walls are not opposed but fit between one another so as to close the cervical canal.

The total length of the uterine cavity from the external os to the fundus is about 6cm.

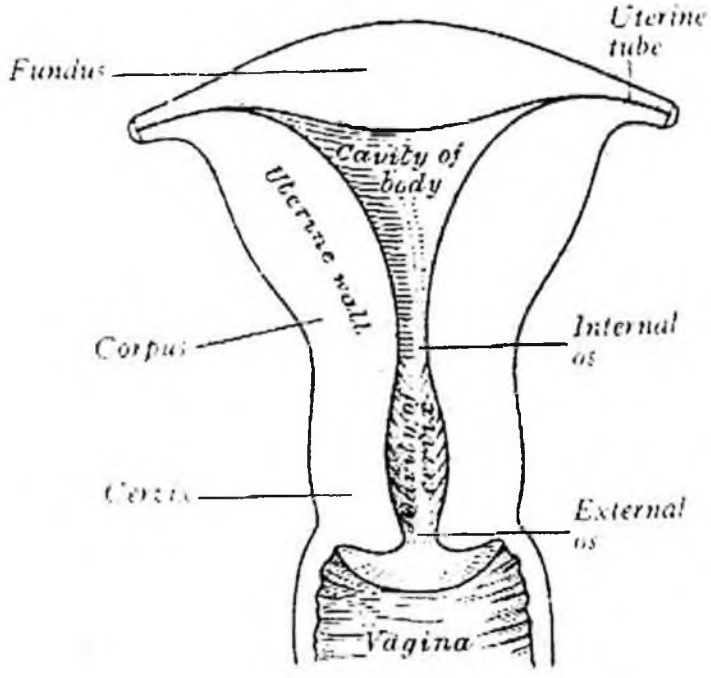

Fig. 2.2 Sectional diagram showing the interior divisions of the uterus and its continuity with the vagina.

Approximately the upper third of the cervix has been termed the isthmus, because it presents certain features which differentiate it from the rest [10,11,12] Although it is unaffected in the first month of pregnancy, it is gradually taken up into the body of the uterus during the second month and forms the 'lower uterine segment. The fetal membranes, through firmly blended with the rest of the uterine mucosa, are not attached to the lower uterine segment. In the non-pregnant uterus the isthmus undergoes

changes associated with menstruation similar to, but less pronounced than those, which occur in the body of the organ. Histologically the isthmus resembles the body more than it resembles the cervix; its lining epithelium is low cylindrical in type and is ciliated; its mucous coat is thinner and the glands are fewer in number than they are in the cervix [2].

2.3 Anatomical Importance of A Point and B Point in Therapeutic Procedure

The Manchester system is one of the oldest and most extensively used systems in the world. It is characterized by doses to four points: point A, point B, a bladder point and a rectum point. The duration of the implant is based on the dose rate calculated at point a, although the dose at the other points are taken into consideration in evaluating a treatment plan. With the availability of the treatment planning computers, most users of the Manchester system examine the isodose distributions in the frontal and sagittal planes in addition to obtaining dose at the four designated points. Point A still remains the point of dose prescription.

Point A was originally defined as 2 cm superior to the lateral vaginal fornix and 2cm lateral to the cervical canal (Fig 2.3). Later, it was redefined to be 2cm superior to the external cervical os (or cervical end of the tandem), and 2cm lateral to the cervical cannel. Point B is defined 3 cm lateral to point A.

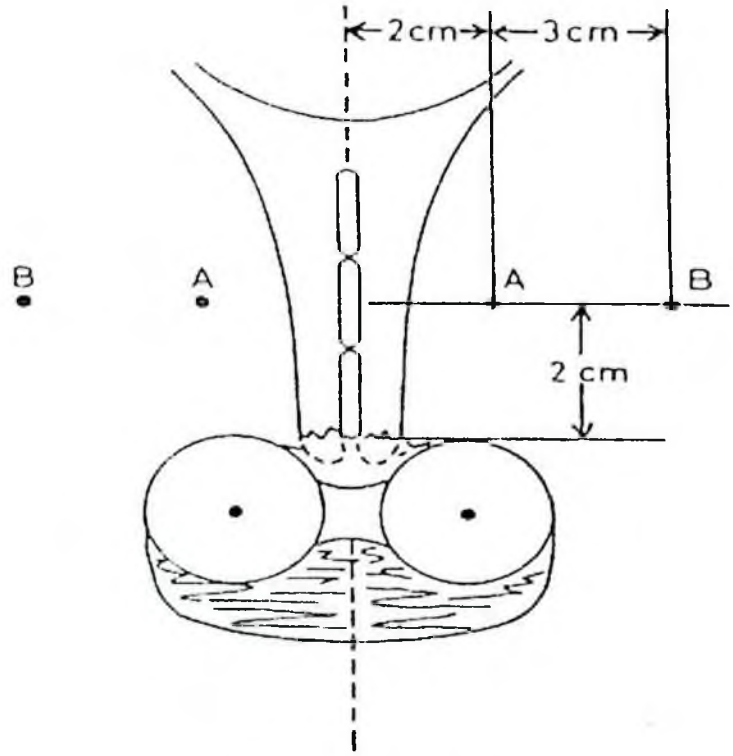

Fig. 2.3 Original definition of points A and B according to the Manchester system.

Ideally, the point A represents the location where the uterine vessels cross the ureter. It is believed that the tolerance of these structures is the main limiting factor in the irradiation of the uterine cervix. The anatomic significance of point A, however, has been questioned by several investigators [13,14,15]. The critics point out the following limitations of point A: (a) it relates to the position of the sources and not to a specific anatomic structure; (b) dose to point A is very sensitive to the position of the ovoid sources relative to the tandem sources, which should not be the determining factor in deciding on implant duration; and (c) depending on the size of the cervix, point A may lie inside the tumor or out side the tumor (Fig 2.4). Thus, dose prescription at the point A could risk under dosage of large cervical cancers or over dosage of small ones [2].

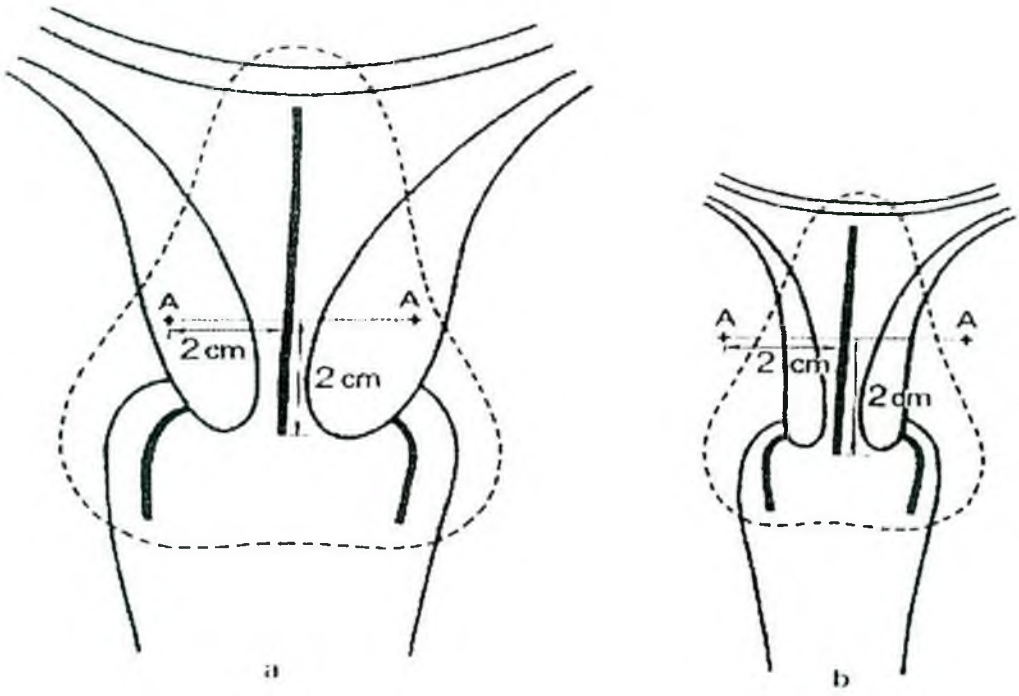

Fig. 2.4 Variation of point A relative to anatomy. (a) Point A inside large cervix, resulting in under dosage. (b) Point A outside small cervix, resulting over dosage.

2.4. Surrounding Critical Organs

2.4.1 The urinary bladder

The urinary bladder reservoir varies in its size, shape and position and relations according to the amount of fluid that it contains, as well as with the state of distension of neighboring viscera. When empty, it is entirely within the lesser pelvis, but as it becomes distended it expands upwards and forwards into the abdominal cavity.

The empty bladder is roughly tetrahedral in form and thus has a base, neck, apex, superior surface and two inferolateral surfaces. The fundus or base is triangular and directed backwards and downwards. In the female (fig 2.1) it is closely related to the anterior wall of the vagina. In the male it is related to the rectum, but its upper part is separated from the rectum by the

rectovesical pouch of peritoneum, and below that the seminal vesicles and different ducts separate the two viscera . In the triangular interval between the two deferent ducts,

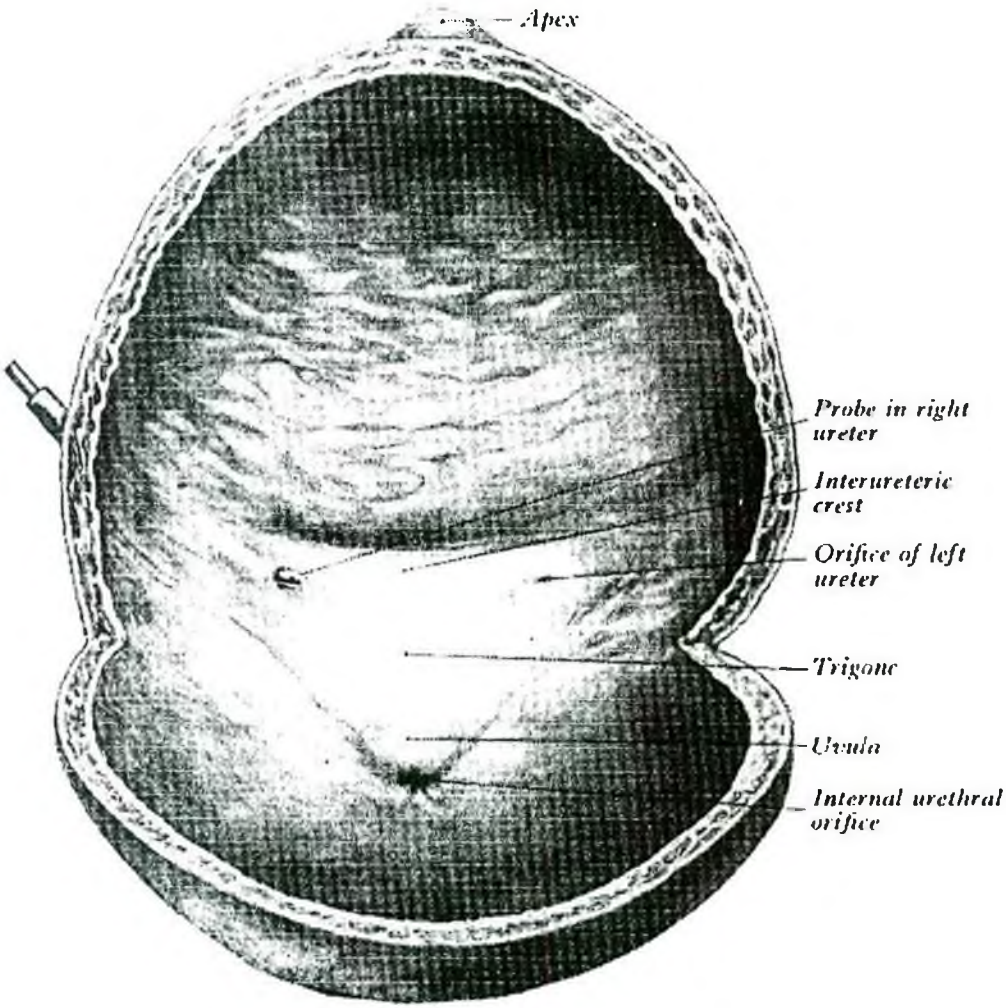

Fig. 2.5 Anterior aspect of the interior of the urinary bladder.

the bladder and the rectum are separated only by the rectovesical fascia ; the inferior part of this triangular interval may often be obliterated by the approximation of the deferent ducts above the prostate. Although the fundus (or base) of the bladder should be, by definition, the lowest region of the bladder, it is the neck which is in fact the lowest and also the most fixed part of the bladder; it lies 3 to 4 cm behind the lower part of the symphysis pubis

of the bladder; it lies 3 to 4 cm behind the lower part of the symphysis pubis (i.e. a little above the plane of the inferior aperture of the lesser pelvis). It is pierced by the internal urethral orifice and is subject to but little alteration in position with varying conditions of the bladder and rectum. There is no special constriction of the bladder at the site of the neck. In the male the neck rests on, and its wall is in direct continuity with, the base of the prostate; in the female it is related to the pelvic fascia, which surrounds the upper of the urethra. The apex in both sexes is directed forwards towards the upper of the symphysis pubis, and from it the median umbilical ligament is continued upwards on the posterior surface of the anterior abdominal wall to the umbilicus; the peritoneum folded over this ligament is the median umbilical fold. The superior surface, triangular shape, is bounded on each side by a lateral border that runs from the apex to the entrance of the ureter in to the bladder, and by a posterior border which corresponds with a line joining the entrances of the ureters in to the bladder. In the male the superior surface is completely covered with peritoneum, which extends slightly on to the base and is continued behind into the rectovesical pouch, at the sides into the paravesical fossae, and at the front in to the median umbilical fold. It is in contact with the sigmoid colon and the terminal coils of the small intestine. In the female the superior surface is almost entirely covered with peritoneum, but near its posterior border the peritoneum is reflected from it to the uterus at the level of the internal os (i.e. the junction of the body and cervix of the uterus), forming the vesico-uterine pouch. The posterior part of the superior surface, devoid of peritoneum, is separated from the supravaginal part of the uterine cervix by areolar fibrous tissue. Each inferolateral surface in the mail is separated anteriorly from the pubis and puboprostatic ligaments by an adipose mass termed the retropubic pad; further posteriorly it is separated by fascia from the levator ani and obturator internus. In the female the relations are the same, except that the

puboprostatic are replaced by the pubovesical ligaments. The inferolateral surfaces are not covered by peritoneum.

As the bladder fills, its borders become rounded off and it assumes an ovoid form. In front it displaces the parietal peritoneum on the suprapubic region of the abdominal wall, so that the inferolateral surfaces (now becoming the anterior surface of the distended bladder) rest against the anterior abdominal wall without the intervention of peritoneum for some distance above the symphysis pubis; this distance varies with the degree of distension of the bladder, but commonly, when the bladder is distended to an average degree, it measures about 5cm, through in excessive distension it may extend as far as the umbilicus or even higher. Thus the full bladder may be approached surgically by incisions or punctures through the anterior abdominal wall a little above the symphysis pubis without traversing the peritoneum. The summit of the full bladder is directed upwards and forwards above the point of attachment of the median umbilical ligaments, so that the peritoneum, which follows the ligament, forms a supravesical recess of varying depth between the summit and the anterior abdominal wall; the recess often contains coils of small intestine.

At birth , the bladder lies at a relatively higher level than in the adult; the internal urethral orifice is at the level of the upper bladder of the symphysis pubis and the bladder is an abdominal, rather than a pelvic organ, extending about two-thirds of the distance up to the umbilicus. It progressively descends until it reaches its adult position shortly after puberty [12].

2.4.2 The Rectum

The rectum (fig 2.6 and 2.7) is continuous above with the sigmoid colon at the level of the third sacral vertebra, the junction being indicated by the lower end of the sigmoid mesocolon. From its origin it descends, following

the concavity of the sacrum and coccyx, forming an anteroposterior curve known as the *sacral flexure* of the rectum. It thus passes at first

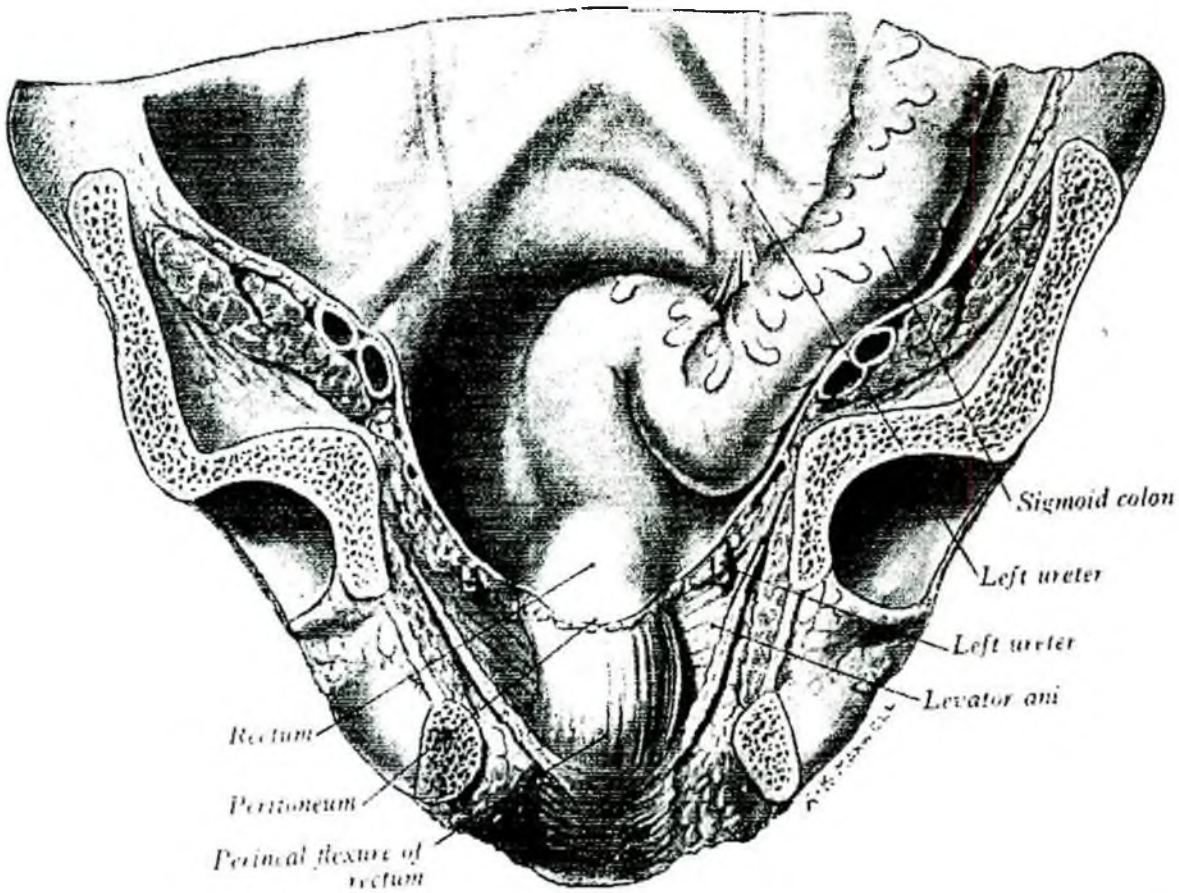

Fig.2.6 Oblique coronal section through the pelvis to expose the anterior aspect of the rectum.

downwards and backwards, then downwards, and finally downwards and forwards to become continuous with the anal canal by passing through the pelvic diaphragm. The *anorectal junction* is situated 2 to 3 cm in front of and slightly below the tip of the coccyx; from this level, which is the male is opposite the apex of the prostate, the anal canal passes downwards and backwards from the lower end of the rectum, the backward bend of the gut at the anorectal junction being termed the *perineal flexure* of the rectum. In

addition to its anteroposterior curve, the rectum deviates from the midline in the form of three lateral curves; the upper one is convex to the right, the middle one (which is the most prominent) bulges to the left, and the lower one is convex to the right; the beginning and end of the rectum are in the median plane (fig 2.7).

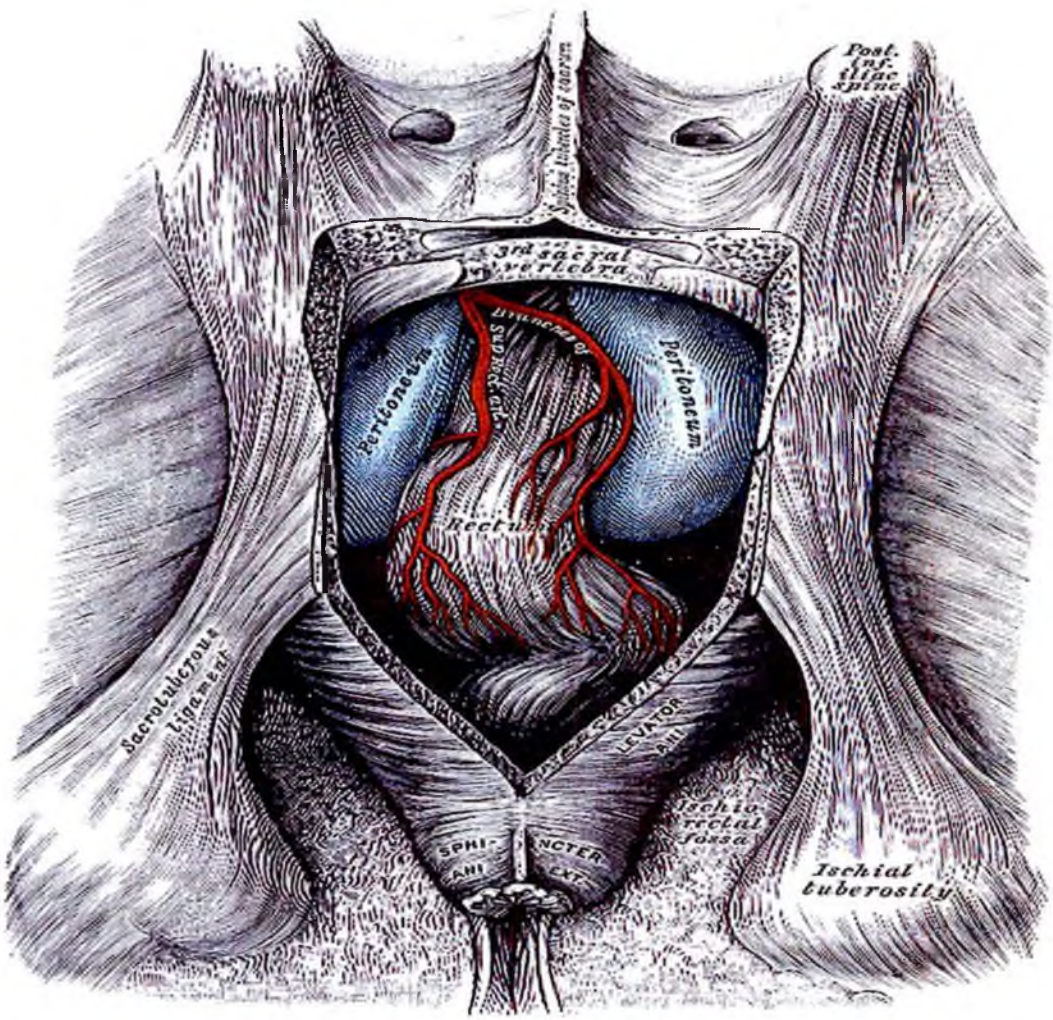

Fig.2.7 Posterior aspect of the rectum exposed by removal of the lower part of the sacrum and coccyx.

The rectum is about 12 cm long and its upper part has the same diameter as the sigmoid colon (about 4 cm in the empty state), but its lower

part is dilated to form the *rectal ampulla.* The rectum differs from the sigmoid colon in that it has no sacculations, appendices epiploicae or mesentery, while the taeniae coli bend about 5 cm above the junction of the rectum and sigmoid colon to form two wide muscular bands which descend, one on the anterior and the other on the posterior wall of the rectum. The peritoneum is related only to the upper two-thirds of the rectum, covering at first its front and sides, but lower down its front only; from the latter it is reflected on to the bladder in the male, forming the rectovesical pouch of peritoneum, and on to the posterior wall of the vagina in the female, forming the recto-uterine pouch. The level of peritoneal reflexion is higher in the male, the rectovesical pouch being about 7.5 cm from the anus (the height to which the index finger inserted through the anus can reach); in the female the recto-uterine pouch is about 5.5 cm from the anus. In the male fetus the peritoneum extends on the front of the rectum as far as the lower end of the prostate (fig 2.7). On the sigmoid colon, as on the gut generally, the peritoneum is intimately attached to the muscle coat, but as it descends on the rectum, the peritoneum becomes more loosely attached and separated from the muscle by fatty tissue, and thus allows considerable expansion of this part of the gut.

In the empty state of the rectum, the mucous membrane of its lower part presents a number of longitudinal folds, which are effaced by distension of the rectum. Besides these, there are permanent *transverse* or *horizontal folds* of a semilunar shape, which are most marked when the rectum is distended. Two forms of horizontal folds have been recognized 68[76]. One, consisting of mucous membrane, the circular and some longitudinal muscle coat, is marked on the outer surface of the rectum by an indentation. The other form is devoid of longitudinal muscle coat and external surface marking. Commonly three folds are present, but their number is variable. The upper one is situated near the commencement of the rectum and may be on the left

or the right side; occasionally it may encircle the gut and the lumen of the gut is then somewhat constricted at this site. The middle fold is the largest and most constant and is situated immediately above the ampulla of the rectum; it projects from the anterior and right walls of the rectum just below the level at which the peritoneum is reflected from the anterior surface of the rectum; the circular muscle in this fold is more marked than in the others. The lowest fold is inconstant and lies on the left side, about 2.5 cm below the middle fold; sometimes a fourth fold is present on the left side, about 2.5 cm above the middle fold described above.

It has been suggested [12,16] that the rectum consists functionally of two parts, one above and the other below the middle fold, the upper part containing faeces and being free to distend towards the peritoneal cavity, while the lower part occupies a more confined situation, enclosed in a tube of condensed extraperitoneal tissue and (except during defaecation) empty in normal individuals, though in cases of chronic constipation, or after death, it may contain faeces. It may be noted that the part of the rectum above the middle fold is usually considered to be developed from the hindgut while the part below, together with the upper part of the anal canal, is derived from the cloaca (post-allantoic gut). Others, [12] however, consider that the sigmoid colon acts as the faecal reservoir, that in normal individuals the rectum is empty (though it may contain faeces in cases off chronic constipation), and that the passage of faeces into the rectum normally excites the desire to defaecate. It has been shown experimentally, by registering the pressure in balloons inserted into the rectum and anal canal, that considerable distension of the rectum results in a desire to defaecate and relaxation of the anal sphincters. [12,17].

Chapter 3

3. Radiotherapy Instruments

3.1 Introduction

Cancer patients are treated by radiation, surgery or chemotherapy or consideration. A treatment method proving increasingly effective is radiation, used by itself or in combination with other modalities. The principal radiation modality for the treatment of deep-seated tumors is X or γ rays of high energy and high penetrating power.

Such X rays are created when high-energy electrons are stopped in a target material such as tungsten. Alternatively, the electrons themselves may be used directly to treat more superficial cancers. The electron linear accelerator (linac), a therapeutic x ray machine that produces high energy X rays or makes use of the electrons themselves, is widely used for radiation therapy. A linear accelerator accelerates charged particles in a straight line, in contrast to the circular orbits that characterize the betatron and cyclotron.

γ-Rays are produced by using radionuclides. Radionuclides such as radium-226, cesium-137, and cobalt-60 have been used as sources of γ rays for teletherapy. These γ rays are emitted from the radionuclides as they undergo radioactive disintegration.

3.2 Linear Accelerator

3.2.1 Introduction

The Linear Accelerator (linac) is a device that uses high frequency electromagnetic waves to accelerate charged particles such as electrons to high energies through a linear tube. The high-energy electron beam itself can be used for treating superficial tumors, or it can be made to strike a target to produce x-rays for treating deep-seated tumors.

The thick concrete walls of the treatment room shield the technologist and other staff from the penetrating radiation. The linac is mounted in a

gantry, which rotates on a stand containing electronic and other system. The linac can be rotated into position about the horizontal gantry axis for use in treatment. The radiation beam emerging from the collimator is always directed through and centered on the gantry axis. The beam central axis intersects the gantry axis at a point in space called the iso-center. In majority of cases, the couch is positioned so that the patient's is centered at the isocenter. Usually, the patient lies supine or prone on the treatment couch (sometimes called patient support assembly). The couch incorporates three linear motions and a rotation motion about the isocenter to facilitate positioning the patient for treatment. Side and ceiling LASERS project small dots or lines that intersect at the isocenter. These facilitate positioning the patient in conjunction with reference marks, often tattoos, placed on the patient's skin. The digital position indicators display the treatment field size together with collimator and gantry rotation angles. In our case a constant radiation Source-gantry Axis-Distance (SAD), usually 100 cm, in employed. Alternatively, some treatment techniques use a constant radiation Source-Skin (of patient) – Distance (SSD), usually for large fields at distances of 100 cm or greater.

The technologist operator views the patient, and presets and monitors the treatment from a control console outside the treatment room. Much of the auxiliary electronics (as well as control and monitoring devices) is housed in the electronic card rack cabinet mounted at the console. A nearby modulator cabinet houses auxiliary electronics for the larger linacs.

There are several types of linear accelerator designed, but the ones used in radiotherapy accelerate electrons either by traveling or stationary electromagnetic waves of frequency in the microwave region (~3000 megacycles/sec) the difference between traveling wave and stationary wave accelerators is the design of the accelerator structure. Functionally, the

traveling wave structures require a terminating, or "dummy," load in order to absorb the residual power at the end of the structure, thus preventing a backward reflected wave. On the other hand, the standing wave structures so that the combination of forward and reverse traveling waves will give rise to stationary waves. In the standing wave design, the microwave power is the beam aperture. However, it is more expensive and requires installation of a circulator or (isolator) between the power source and the structure to prevent reflections from reaching the power source.

Figure-4.1 is a block diagram of a medical linear accelerator showing major components and auxiliary systems. A power supply provides DC power to the modulator, which includes the pulse forming network and a switch tube known as hydrogen thyratron. High voltage pulses from the modulator section are flat-topped DC pulses of a few microseconds in duration. These pulses are delivered to the magnetron or klystron and simultaneously to the electron gun. Pulsed microwaves produced in the mgnetron or klystron and injected into the accelerator tube or structure via a wave-guide system. At the proper instant electrons, produced by an electron gun, are also pulse injected it to the accelerator structure.

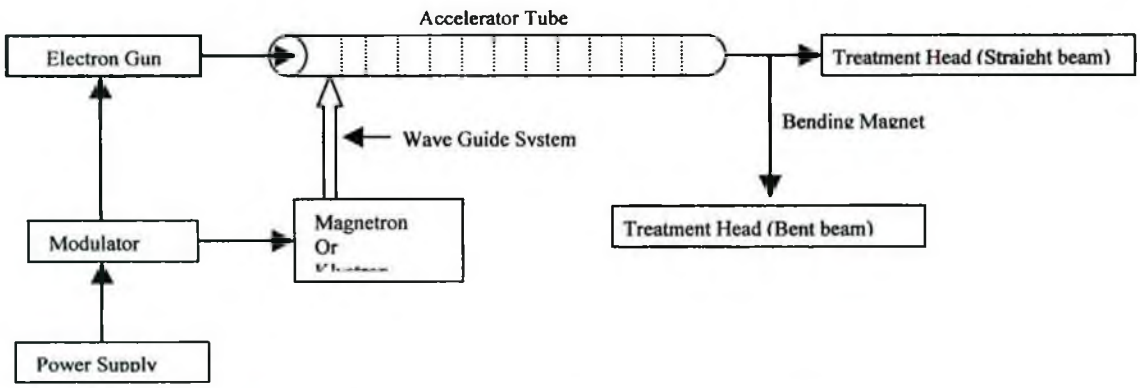

Fig.3.1A block diagram of typical medical linear accelerator

The accelerator structure (or accelerator wave guide) consists of a copper tube with its interior divided by copper discs or diaphragms of varying aperture and spacing. This section is evacuated to a high vacuum. As the electrons are injected into the accelerator structure with an initial energy of about 50 keV, the electrons interact with the electromagnetic field of the microwaves. The electrons gain energy from the sinusoidal electric field by an acceleration process analogous to that of a surf rider.

As the high-energy electrons emerge from the exit window of the accelerator structure, they are in the form of a pencil beam of about 3 mm in diameter. In the low energy linacs (up to 6 MV) with relatively short accelerator tube, the electrons are allowed to proceed straight on and strike a target for x-ray production. In the higher energy linacs, however, the accelerator structure is too long and, therefore, is placed horizontally or at an angle with respect to the horizontal. The electrons are then bent through a suitable angle (usually about 90^0 or 270^0) between the accelerator structure and the target. The precision bending of the electron beam is accomplished by the beam transport system consisting of bending magnets, focusing coils, and other components.

3.2.2 The Magnetron

The magnetron is a device that produces microwaves. It functions as a high power oscillator, generating microwave pulses of several microseconds duration and with a repetition rate of several hundred pulses per second. The frequency of the microwaves with in each pulse is about 3000MHz.

The magnetron has a cylindrical construction, having a central cathode and an outer anode with resonant cavities machined out of a solid piece of copper. The space between the cathode and the anode is evacuated. The cathode is heated by an inner filament and the electrons are generated buy thermionic emission. A static magnetic field is applied perpendicular to

the plane of the cross section of the cavities and a pulsed DC electric field is applied between the cathode and the anode. The electrons emitted from the cathode are accelerated toward the anode by the action of the pulsed DC electric field. Under the simultaneous influence of the magnetic field, the electrons move in complex spirals toward the resonant cavities, radiating energy in the forma of microwaves. The generated microwave pulses are led to the accelerator structure via the wave-guide.

3.2.3 The Klystron

The klystron is not a generator of microwaves but rather a microwave amplifier. It needs to be driven by a low power microwave oscillator.

The electrons produced by the cathode are accelerated by a negative pulse of voltage into the first cavity, called the buncher cavity, which is energized by low power microwaves. The microwaves set up an alternating electric field across the cavity. The velocity of the electrons is altered by the action of this electric field to a varying degree by a process known as velocity modulation. Some electrons are speeded up while others are slowed down and some are unaffected. This results in bunching of electrons as the velocity-modulated beam passes through a field free space in the drift tube.

As the electron bunches arrive at the catcher cavity, they induce charges on the ends of the cavity and thereby generate a retarding electric field. The electrons suffer deceleration, and by the principle of conservation of energy, the kinetic energy of electrons in converted into high power microwaves.

3.2.4 The Linac X-Ray Beam

Bremsstrahlung X-rays are produced when the electrons are incident on a target of a high-Z material such as tungsten. The target is water-cooled and is thick enough to absorb most of the incident electrons. As a result of bremsstrahlung-type interactions, the electron energy is converted into a

spectrum of X-ray energies with maximum energy equal to the incident electron energy. The average photon energy of the beam is approximately one-third of the maximum energy.

It is customary for some of the manufacturers to designate their linear accelerators that have both electron and X-ray treatment capabilities by the maximum energy of the electron beam available. For example, the Varian Clinac 18 unit produces electron beams of energy 6, 9, 12, 15, and 18 MeV and X-rays of energy 10 MV (million electron volts).

3.2.5 The Electron Beam

The electron beam, as it exits the window of the accelerator tube is a narrow pencil about 3 mm in diameter. In the electron mode of linac operation, this beam, instead of striking the target, is made to strike an electron scattering foil in order to spread the beam as well as get a uniform electron fluence across the treatment across the treatment field. The scattering foil consists of a thin metallic foil, usually of lead. The thickness of the foil is such that most of the electrons are scattered instead of suffering bremsstrahlung. However, a small fraction of the total energy is still converted into bremsstrahlung and appears as X ray contamination of the electron beam.

In some linacs, the broadening of the electron beam is accomplished by electromagnetic scanning of the electron pencil beam over a large area. Although this minimizes the X-ray contamination, some X-rays are still produced by electrons striking the collimator walls or other high atomic number materials in the electron collimation system.

3.2.6 Treatment Head

The treatment head consists of a thick shell of high density shielding material such as lead, tungsten, or lead-tungsten alloy. It contains an X-ray target, scattering foil, flattening filter, ion chamber, fixed and movable

collimator, and light localizer system. The head provides sufficient shielding against leakage radiation in accordance with radiation protection guidelines.

3.2.7 Target and Flattening Filter

The linear accelerators produce electrons in the mega voltage range, the X-ray intensity is peaked in the forward direction. To make the beam intensity uniform across the field, a flattening filter is inserted in the beam. This filter is usually made of lead, although tungsten, uranium, steel, aluminum, or a combination has also been used or suggested.

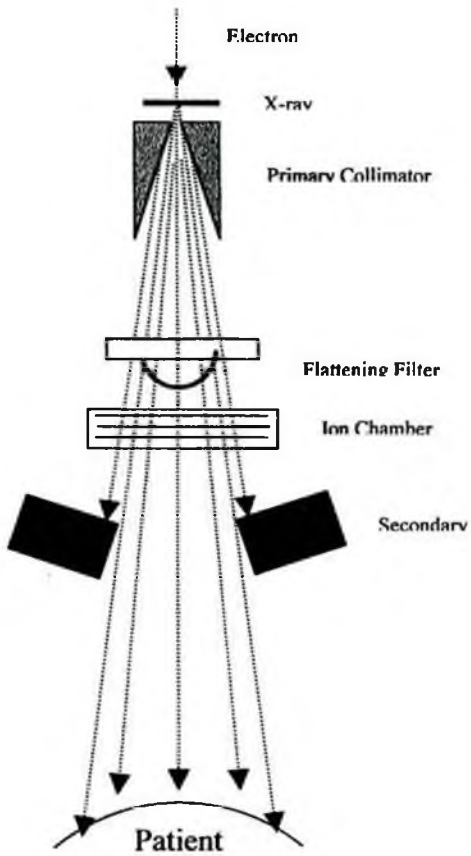

Fig.3.2 Schematic diagram of LINAC

3.2.8 Beam Collimation and Monitoring

The treatment beam is first collimated by a fixed primary collimator located immediately beyond the X ray target. In the case of X rays, the collimated beam then passes through the flattening filter. In the electron mode, the filter and X-ray target are moved out of the way.

The flattened X-ray beam or the electron beam is incident on the dose monitoring chambers. The monitoring system consists of several ion chambers or a single chamber with multiple plates.

The function of the ion chamber is to monitor dose rate, integrated dose, and field symmetry. Since the chambers are in a high-intensity radiation field and the beam is pulsed, it is important to make sure that the ion collection efficiency of the chambers remains unchanged with changes in the dose rate. Bias voltages in the range of 300 to 400V are applied across the chamber electrodes, depending on the chamber design. Contrary to the beam calibration chambers, the monitor chambers in the treatment head are usually sealed so that their response is not influences by temperature and pressure of the outside air. However, these chambers have to be periodically checked for leaks.

After passing through the ion chambers, the beam is further collimated by a continuously movable X-ray collimator. This collimator consists of two pairs of lead or tungsten blocks (jaws) which provide a rectangular opening from 0×0 cm^2 to the maximum field size 40×40 cm^2 or a little less projected at a standard distance such as 100 cm from the X-ray source (focal spot on the target). The collimator blacks are constrained to move so that the block edge is always along a radial line passing through the target.

The field size definition is provided by a light localizing system in the treatment head. A combination of mirror and a light source located in the space between the chambers and the jaws projects a light beam as if emitting from the X-ray focal spot. Thus the light field is congruent with the radiation of field alignment.

Whereas the X-ray collimation systems of most medical linacs are similar, the electron collimation systems vary widely. Since electrons scatter readily in air, the beam collimation must be achieved close to the skin surface of the patient. There is a considerable scattering of electrons from the collimator surfaces including the movable jaws. Dose rate can change by a factor of two or three as the collimator jaws are opened to maximum field size limits. If the electrons are collimated by the same jaws, as for X-rays, there will be as extremely stringent requirement on the accuracy of the jaw opening, since output so critically depends on the surface area of the collimator. This problem has been solved by keeping the X-ray collimator wide open and attaching an auxiliary collimator for electrons in the form of trimmers extended down to the skin surface. In other systems, the auxiliary electron collimator consists of a set of attachable cones of various sizes.

It should be mentioned that due to the electron scattering the dose distribution in an electron field is significantly influenced by the collimation system provided with the machine.

3.2.9 Gantry

Most of the accelerators currently produced are constructed so that the source of radiation can rotate about a horizontal axis. As the gantry rotates, the collimator axis (supposedly coincident with the central axis of the beam) moves in a vertical plane. The point of intersection of the collimator axis and the axis of rotation of the gantry is known as the iso-center.

The isocentric mounting of the radiation machines has advantages over the units that move only up and down. The latter units are not suitable for isocentric treatment techniques in which beams are directed from different directions but intersect at the same point, the isocenter, placed inside the patient. However, the nonisocentric units are usually swivel mounted, i. e., the treatment head can be swiveled or rotated in any direction while the gantry can move only upward or downward. Although these units are not as flexible, they are mechanically simpler, more reliable, and less expensive than the isocentric models [18].

3.3 Cobalt-60 Unit

3.3.1 Source

The ^{60}Co source is produced by irradiating ordinary stable ^{59}Co with neutrons in a reactor. The nuclear reaction can be represented by $^{59}Co(n,\gamma)^{60}Co$.

The ^{60}Co source, usually in the form of a solid cylinder, discs, or pallets, is contained inside a stainless-steel capsule and sealed by wilding. This capsule is placed into another steel capsule, which is again sealed by welding. The double-welded seal is necessary to prevent any leakage of the radioactive material.

The ^{60}Co source decays to ^{60}Ni with emission of β particles (E_{max}=0.32 MeV) and two photons per disintegration of energies 1.17 and 1.33 MeV[4]. These γ rays constitute the useful treatment beam. The β particles are absorbed in the cobalt metal and the stainless steel capsules resulting in the emission of the bremsstrahlung X-rays and a small amount of characteristic X-rays. However, these X-rays of average energy around 0.1 MeV do not contribute appreciably to the dose in the patient because they are strongly attenuated in the material of the source and the capsule. The other "contaminants" to the treatment beam are the lower-energy γ rays produced

by the interaction of the primary γ radiation with the source itself, the surrounding capsule, the source housing, and the collimator system. The scattered components of the beam contribute significantly (~10%) to the total intensity of the beam. All these secondary interactions thus, to some extent, result in heterogeneity of the beam. In addition, electrons are also produced by these interactions and constitute what is usually referred to as the electron contamination of the photon beam.

A typical teletherapy ^{60}Co source is a cylinder of diameter ranging from 1.0 to 2.0 cm and is positioned in the cobalt unit with its circular end facing the patient. The fact that the radiation source is not a point source complicates the beam geometry gives rise to what is known as the geometric penumbra.

3.3.2 Source Housing

The housing for the source is called the source head. It consists of a steel shell filled with lead for shielding purposes and a device for bringing the source in front of an opening in the head from which the useful beam emerges. Also, a heavy metal alloy sleeve is provided to form an additional primary shield when the source is in the off position.

A number of methods have been developed for moving the source from the off position to the on position. It will suffice her to mention briefly four different mechanisms: (a) the source mounted on a rotating wheel inside the source head to carry the source from the off position to the on position; (b) the source mounted on a heavy metal drawer plus its ability to slide horizontally through a hole running through the source head-in the on position the source faces the aperture for the treatment beam and in the off position the source moves to its shielded location and a light source mounted on the same drawer occupies the on position of the source; (c) mercury is allowed to flow into the space immediately below the source to

shut off the beam; and (d) the source is fixed in front of the aperture and the beam can be turned on and off by a shutter consisting of heavy metal jaws. All of the above mechanisms incorporate a safety feature in which the source is returned automatically to the off position in case of a power failure.

3.3.3 Beam Collimation and Penumbra

A collimator system is designed to vary the size and shape of the beam to meet the individual requirements. The simplest form of a continuously adjustable diaphragm consists of two pairs of heavy metal blocks. Each pair can be moved independently to obtain a square or a rectangle-shaped field. Some collimators are multivane type, i.e., multiple blocks to control the size of the beam. In either case, if the inner surface of the blocks is made parallel to the central axis of the beam, the radiation will pass through the edges of collimating blocks resulting in what is known as the transmission penumbra. The extent of this penumbra will be more pronounced for larger collimator openings because of grater obliquity of the rays at the edges of the blocks. The effect has been minimized in some designs by shaping the collimator blocks so that the inner surface of the blocks remains always parallel to the edge of the beam. In these collimators, the blocks are hinged to the top of the collimator housing so that the slope of the blocks is coincident with the included angle of the beam. Although the transmission penumbra can be minimized with such an arrangement, it cannot be completely removed for all field sizes.

The term penumbra, in a general sense, means the region, at the edge of a radiation beam, over which the dose rate changes rapidly as a function of distance from the beam axis. The transmission penumbra, mentioned above, is the region irradiated by photons, which are transmitted through the edge of the collimator block.

Another type of penumbra, known as the geometric penumbra, is illustrated in Fig.-4.3. The geometric width of the penumbra (P_d) at any depth (d) from the surface of a patient can be determined by considering similar triangles ABC and DEC. From geometry we have

$$\frac{DE}{AB}=\frac{CE}{CA}=\frac{CD}{CB}=\frac{MN}{OM}=\frac{OF+FN-OM}{OM} \quad \text{.....3.1}$$

If AB = s, the source diameter, OM = SDD, the source to diaphragm distance, OF = SSD, the source to surface distance, then from the above equation, the penumbra (DE) at depth d is given by

$$P_d=\frac{s(SSD+d-SDD)}{SDD} \quad \text{.....3.2}$$

The penumbra at the surface can be calculated by substituting d = 0 in Equation-3.2

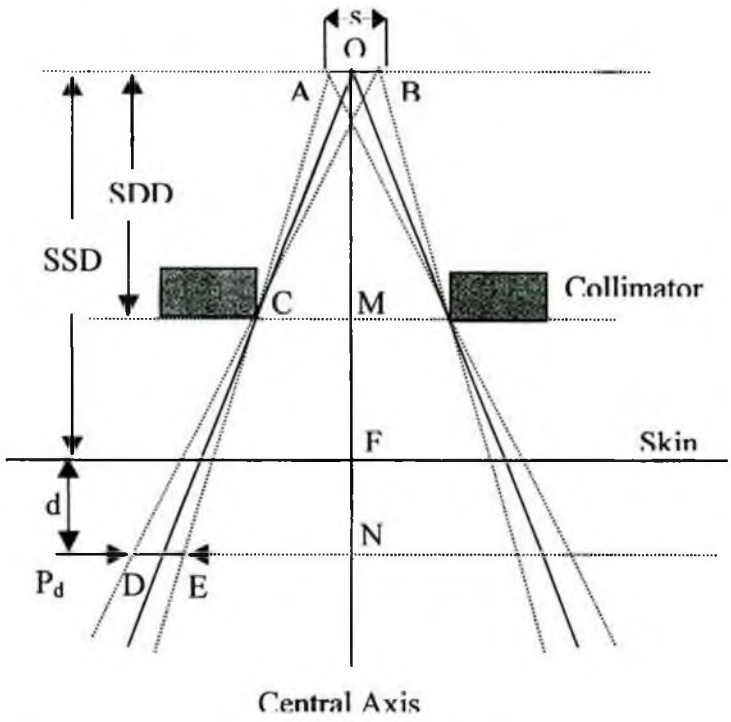

Fig.3.3 Diagram for calculating geometry penumbra

As Equation-3.2 indicates, the penumbra width increases with increase in source diameter, SSD, and depth but decreases with an increase in SDD. The geometric penumbra, however, is independent of field size as long as the movement of the diaphragm is in one plane, i.e., SDD stays constant with increase in field size.

Since SDD is an important parameter in determining the penumbra width, this distance can be increased by extendable penumbra trimmers. These trimmers consist of heavy metal bars to attenuate the beam in the penumbra region, thus "sharpening" the field edges. The penumbra, however, is not eliminated completely but reduced since SDD with the trimmers extended is increased. The new SDD is equal to the source to trimmer distance. An alternative way of reducing the penumbra is to use secondary blocks, placed close to the patient, for redefining or shaping the field. The blocks should not be placed closer than 15 to 20 cm from the patient because of excessive electron contaminants produced by the block-carrying tray.

The combined effect of the transmission and geometric penumbras is to create a region of dose variation at the field edges. A dose profile of the beam measured across the beam in air at a given distance from the source would show dosimetrically the extent of the penumbra. However, at a depth in the patient the dose variation at the field border is a function of not only geometric and transmission penumbras but also the scattered radiation produced in the patient [19].

3.4 Description of Ion Chamber and Electrometer

3.4.1 Ionization Chamber

Ionization chamber is basically a gas field detector system. An ionization chamber consists of two co-axial electrodes that are insulated from each other. The inner surface of the chamber wall is coated by a special material to make it electrically conducting. This forms one electrode (anode). The other electrode (cathode) is a rod of low atomic number material such as graphite or aluminum held in the center of the chamber but electrically insulated from it.

The photons interact with the wall material and release electrons. These electrons ionize the air in the cavity. A suitable voltage is applied between the two electrodes to collect the ions produced in the air cavity. Estimation of absorbed dose in soft tissue or any other medium can be obtained by measurements of ionization in a small gas filled cavity in the medium. The conversion of ionization in the gas filled cavity to absorbed dose in the medium is accomplished by application of the Bragg-Gray principle.

Although there are several dosimeters available, using calibrated ionization chamber of good stability and a sensitive electrometer, the highest dosimetric accuracy can be obtained including dosimetry, and hence ionization dosimetry is the recommended method of dosimetry in radiotherapy.

3.4.2 Ionization Chamber Dosimetric System

An ionization chamber dosimetric system contains an ionization chamber and a charge-measuring device called electrometer. The basic parts

of an ionization chamber dosimetric system are shown in Figure-3.4. In the present study, a 0.1 cc micro ion chamber type 23323 in conjunction with a PTW UNIDOS electrometer has been used for dose measurements. The collecting electrode of the ionization chamber is connected to a charge/current-measuring device called the electrometer. The cable should be long enough so that the electrometer can be placed outside the room at the control console of the teletherapy unit.

The PTW ionization chamber type 23323 is a standard sealed chamber for therapy dosimeter. It is watertight and equipped with a flexible stem so that it can be used in variable temperature surrounding.

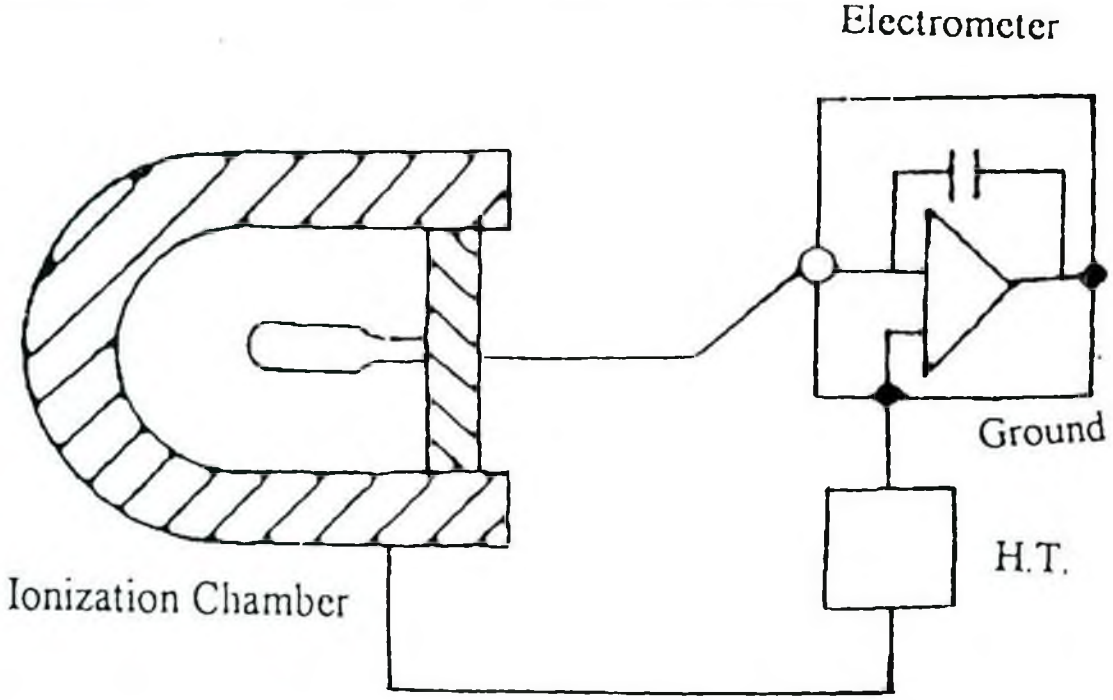

Fig.3.4 Parts of an ionizaton chamber dosimetric system

UNIDOS is a highly sensitive electrometer. It is a micro-processor controlled universal field class dosimeter. It can determine the dose by measuring the charge or by numerically integrating the dose rate, the measurement of which is based on the measurement of current. The first method is called direct dose mode, the second method integrated dose mode. The integrated dose mode enables simultaneous measurement of the dose and the dose rate

3.5. Water phantom in radiotherapy instruments

3.5.1 Necessity of water phantom in radiotherapy

In addition to a phantom for routine calibrations, a larger phantom is required for acceptance tests and machine commissioning measurements[3,51]. Once an ionometric dosimetry system has been selected, one must decide on a water phantom. The phantom material should have the same density as tissue and the same number of electrons per gram. Water and wet tissues absorb photons in almost the same way because water have the same effective atomic number i.e number of electrons per gram, and mass density as tissues, and for this reason water has been used in many dose distribution.

It is recommended that a water phantom is extended 5 cm beyond the radiation field on all sides and 10 cm beyond the deepest point of measurement [3,51]. Since most accelerators have field sizes up to 40×40 cm^2, a water phantom of 50×50×40 cm^3 seem to be required. Due to some difficulties we have made a phantom of 45×45×30 cm^3 size but we have calculated the doses up to the field size of 35×35 cm^2. Although we have calculated doses up to field size of 40X40 cm^2 for observed the variation some discrepancy.

Ideally, for a given material to be tissue or water equivalent, it must have same effective atomic number, number of electrons per gram, and mass

density. $\bar{Z}$ is the effective atomic number of an element with which photons interact the same way as with the given composite material. Since photoelectric effect is highly Z dependent, $\bar{Z}$ is considered for photoelectric interactions. The effective atomic number of a compound is calculated by the following equation

$$\bar{Z} = \left(a_1 Z_1^{2.94} + a_2 Z_2^{2.94} + \cdots\cdots\cdots + a_n Z_n^{2.94}\right)^{\frac{1}{2.94}} \quad \text{(3.3)}$$

Where a_1, a_2, a_3,.....a_n are the factorial contribution of each element to the total number of electrons in the mixture.

Since the Compton effect is the predominant mode of interaction for megavoltage photon beams in the clinical range, the necessary condition for water equivalence for such beams is the same electron density (number of electrons per cubic centimeter) as that of water.

The electron density (ρ_e) of a material may be calculated from its mass density (ρ_m) and its atomic composition according to the formula:

$$\rho_e = \rho_m N_A \left(\frac{Z}{A}\right) \quad \text{(3.4)}$$

$$\text{where } \frac{Z}{A} = \sum_i a_i \left(\frac{Z_i}{A_i}\right) \quad \text{(3.5)}$$

N_A is the Avogadro's number and a_i is the fraction by weight of the each element of atomic number Z_i and atomic weight A_i. Electron densities of various human tissues and body fluids are given in Table-3.1.

Table-3.1: No. Of electrons per gram of various body material

Material	Density (g/cm^3)	Effective atomic number	No. of electrons per gram
Fat	0.916	5.92	$3.48x10^{23}$
Muscle	1.00	7.42	$3.36x10^{23}$
Water	1.00	7.42	$3.34x10^{23}$
Air	0.001293	7.64	$3.01x10^{23}$
Bone	1.85	13.80	$3.00x10^{23}$

Table-3.2 gives the properties [4,21] of various phantoms, which have been frequently used for radiation dosimetry. Of the commercially available phantom materials, **Lucite** and **polystyrene** are the most frequently used as dosimetry phantoms.

Table-3.2: Physical properties of various phantom materials

Material	Chemical composition	Mass density (g/cm^3)	No. Of electrons ($x10^{23}$)	Z_{eff}^* (Photoelectric)
Water	H_2O	1	3.34	7.42
Polystyrene	$(C_8H_8)_n$	1.03-1.05	3.24	5.69
Plexiglas (Perspex, Lucite)	$(C_8O_2H_8)_n$	1.16-1.20	3.24	6.48
Polyethylene	$(CH_2)_n$	0.92	3.44	6.16
Paraffin	C_nH_{2n+2}	0.87-0.91	3.44	5.42
Mix D	Paraffin-60.8 Polyethylene-30.4 MgO-6.4 TiO_2-2.4	0.99	3.41	7.05
M 3	Paraffin-70.00 MgO-29.00 $CaCO_3$-0.94	1.06	3.34	7.35
Solid Water	Expoxy resin based mixturc	1.00	3.34	---

Z_{eff} for photoelectric effect is given by Equation (3.3)

(We have used Perspex for fabrication of our water phantom.)

3.5.2. Elementary Description of Fabricated Water Phantom

A multi-purpose, water filled phantom was developed for dosimetry measurement in radiotherapy treatment. The phantom accommodates common designs of thimble ionization chamber, and both the chamber position and orientation are adjustable. We have used Perspex for fabrication of water phantom. The specifications of our water phantom are given below:

Outer Dimensions

Length	: 45 cm
Width	: 33 cm
Height	: 45 cm

Inner Dimensions

Length	: 42 cm
Width	: 30 cm
Height	: 43.5 cm
Tank Material	: 1.5 cm thick Perspex
Density of Material	: ~1.147 gm/cm^3
Tank Volume	: 55 liters
Tank Weight (Empty)	: 15 Kg
Tank Weight (Filled)	: 70 Kg
Construction	: Cemented

The water phantom is designed for calibration measurements in radiotherapy using horizontal beam. It has 10×10 cm^2 entrance window, which is 5.0 cm thick in one wall.

Chapter 4

4.Introductory Description of Radiotherapy Procedure

4.1 Interaction of radiation with matter

Attenuation of a photon beam by an absorbing material is caused by five major types of interactions. One of these, is photo disintegration. This reaction between photon and nucleus is only important at very high photon energies (>10 MeV). The other four process are:

1) Coherent scattering
3) The photoelectric effect
2) The Compton effect and
3) The pair production

4.1.1 Coherent scattering

The coherent scattering, also known as classical scattering or Rayleigh scattering, is illustrated in (Fig.4.1). The process can be visualized by considering the wave nature of electromagnetic radiation. This interaction consists of an electromagnetic wave passing near the electron and setting it into oscillation. The oscillating election reradiates the energy at the same frequency as the incident electromagnetic wave. These scattered x-rays have the same wavelength as the incident beam.

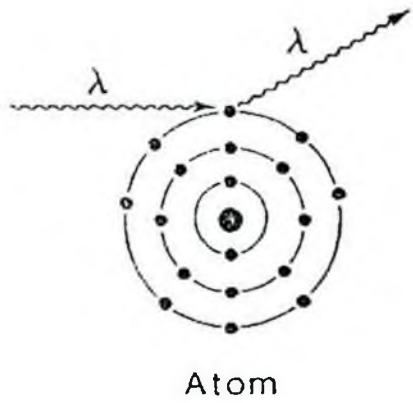

Figure 4.1 Diagram illustrating the process of coherent scattering. The scattered photon has the same wavelength as the incident photon. No energy is transferred.

Thus no energy is change into electronic motion and no energy is absorbed in the medium. The only effect is the scattering of the photon at small angles. The coherent scattering is probable in high atomic number materials and with photons of low energy. The process is only of academic interest in radiotherapy.

4.1.2 Photoelectric effect

The photoelectric effect is a phenomenon in which a photon interacts with an atom and ejects one of the orbital electrons from the atom (Fig.4.2). In this process, the entire energy $h\upsilon$ of the photon is transferred to the atomic electron. The kinetic energy of the ejected electron (called the photoelectron) is equal to $h\upsilon - E_B$, where E_B is the binding energy of the electron. Interactions of this type can take place with electrons in the K, L, M or N shells.

After the electron has been ejected from the atom, a vacancy is created in the shell, thus leaving the atom in an excited state. The vacancy can be filled by an outer orbital electron with the emission of characteristic x-rays. There is also the possibility of emission of Auger electrons, which are

monoenergetic electrons produced by the absorption characteristic x-rays internally by the atom. Since the K shell binding energy of soft tissues is only about 0.5 keV, the energy of the characteristic photons produced in biologic absorbers is very low and can be considered to be locally absorbed. For higher-energy photons and higher atomic number materials, the characteristic photons are of higher energy and may deposit energy at large distances compared with the range of the photoelectrons. In such cases, the local energy absorption is reduced by the energy emitted as characteristic radiation (also called fluorescent radiation), which is considered to be remotely absorbed.

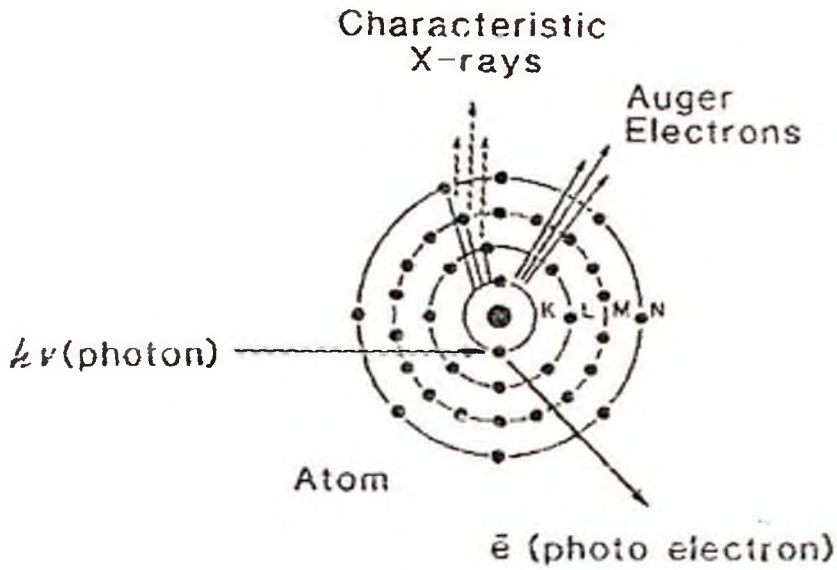

Figure 4.2 Illustration of the photoelectric effect

The probability of photoelectric absorption depends on the photon energy as illustrated in (Fig.4.3), where the mass photoelectric attenuation coefficient (τ/ρ) is plotted as a function of photon energy. Data are shown for water, representing a low atomic number material similar to tissue, and for

lead, representing a high atomic number material. Since on logarithmic pic...paper, the graph is almost a straight line with a slope of approximately –3, we get the following relationship between τ/ρ and photon energy.

$$\tau/\rho \propto 1/E^3$$

The graph for lead has discontinuities at about 15 and 88 keV. Theses are called absorption edges and correspond to the binding energies of L and K shells. A photon with energy less than 15 keV does not have enough energy to eject an L electron. Thus, below 15 keV, the interaction is limited to the M or higher-shell electrons. When the photon has an energy that just equals the binding energy of the L shell, resonance occurs and the probability of photoelectric absorption involving the L shell becomes very high. Beyond this

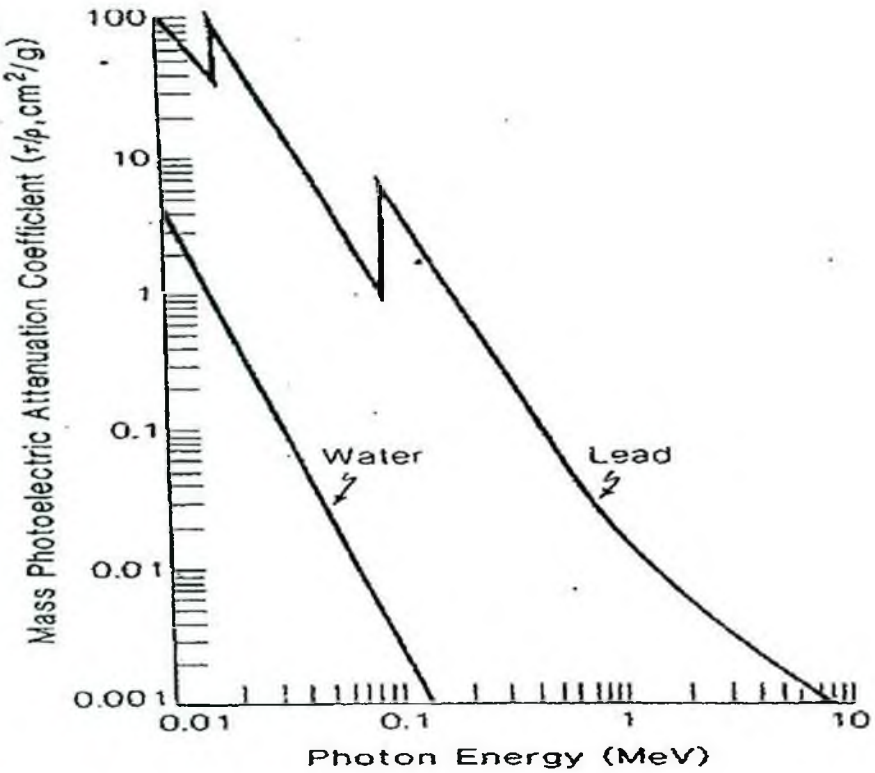

Figure 4.3. Mass photoelectric attenuation coefficient (τ/ρ) plotted against photon energy.

point, if the photon energy is increased, the probability of photoelectric attenuation decreases approximately as $1/E^3$ until the next discontinuity, the K absorption edge. At this point on the graph, the photon has 88 keV energy, which is lust enough to eject the K electron. As seen in Figure the absorption probability in lead at this critical energy increases dramatically, by a factor of about 10.

The discontinuities or absorption edges for water are not shown in the graph because the K absorption edge for water occurs at very low photon energies (~0.5 keV).

The data for various materials indicate that photoelectric attenuation depends strongly on the atomic number of the absorbing material. The following approximate relationship holds:

$$\tau / \rho \alpha Z^3$$

This relation forms the basis of many applications in diagnostic radiology. The difference in Z of various tissues such as bone, muscle, and fat amplifies differences in x-ray absorption, provided the primary mode of interaction is photoelectric. This Z^3 dependence is also exploited when using contrast materials such as $BaSO_4$ mix and Hypaque. In therapeutic radiology, the low-energy beams produced by superficial and orthovoltage machines cause unnecessary high absorption of x-ray energy in bone as a result of this Z^3 dependence.

4.1.3 Compton effect

In the Compton process, the photon interacts with an atomic electron as though it were a "free" election. The term *free* here means that the binding energy of the electron is much less than the energy of the bombarding photon. In this interaction, the electron receives some energy from the photon and is emitted at an angle θ (fig.4.4) .The photon, with reduced energy, is scattered at an angle Φ.

The Compton process can be analyzed in terms of a collision between two particles, a photon and an electron. By applying the laws of conservation of energy and momentum, one can drive the following relationships [20].

$$E = h\nu_0 \frac{\alpha(1-\cos\phi)}{1+\alpha(1-\cos\phi)}$$

$$h\nu' = h\nu_0 \frac{1}{1+\alpha(1-\cos\phi)}$$

$$\cos\theta = (1+\alpha)\tan\phi/2$$

where $h\nu_0$, $h\nu'$, and E are the energies of the incident photon, scattered photon, and electron, respectively and, $\alpha = h\nu_0/m_0c^2$, where m_0c^2 is the rest energy of the electron (0.511MeV). If $h\nu_0$ is expressed in MeV, then $\alpha = h\nu_0/0.511$

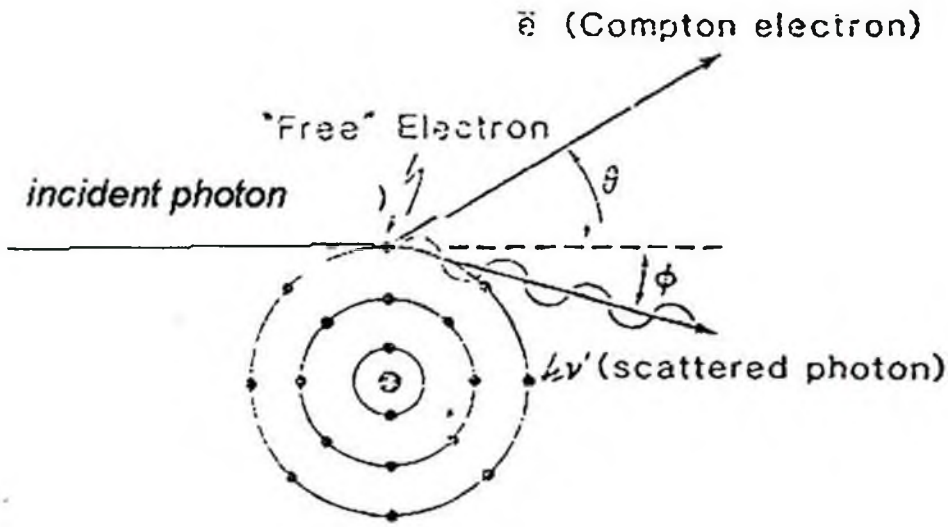

Figure 4.4. Diagram illustrating the Compton effect.

4.2 Interaction of X and Gamma Rays in the Body

4.2.1 Introduction

The dominant mode of interaction of x- and gamma ray photons in a particular region of the body varies with the energy of the photons and with the effective atomic number and electron density (electrons per kilogram) of the region. For purposes of dosimetry, the body may be divided into regions:

(1) Fat
(2) Muscle (or soft tissue excluding fat)
(3) Bone and
(4) Air-filled cavities.

The effective atomic number, average density and electron density are listed in Table-4.1 for these constituents of the body.

Table-4.1: Effective atomic number, physical density and electron density for air water and body constituents.

Material	Effective atomic no.	Density (kg/cu m)	Electron density (electrons/kg)
Air	7.6	1.29	3.01×10^{26}
Water	7.4	1.00	3.34×10^{26}
Soft tissue	7.4	1.00	3.36×10^{26}
Fat	5.9-6.3	0.91	$(0.34\text{-}3.48) \times 10^{26}$
Bone	11.6-13.8	1.65-1.85	$(3.00\text{-}3.19) \times 10^{26}$

4.2.2 F-Factor

An exposure of 1R provides an absorbed dose of 0.869 rad in air:

$$D_{air}(rad) = 0.869\ X\ (R) \quad \ldots\ldots\ldots\ldots\ldots\ldots\ldots\ldots\ldots\ldots \quad (4.1)$$

The dose to a medium such as soft tissue is related to the dose in air at the same location by the ratio of energy absorption in the medium to energy absorption in air:

$$D_{med} = D_{air}\frac{[(\mu_{en})_m]_{med}}{[(\mu_{en})_m]_{air}} \quad \ldots\ldots\ldots\ldots\ldots\ldots\ldots\ldots\ldots\ldots \quad (4.2)$$

$$D_{med} = 0.869\frac{[(\mu_{en})_m]_{med}}{[(\mu_{en})_m]_{air}} \quad \ldots\ldots\ldots\ldots\ldots\ldots\ldots\ldots\ldots\ldots \quad (4.3)$$

In equation (4.3), $[(\mu_{en})_m]_{med}$ is the mass energy absorption coefficient to the medium for photons of the energy of interest. This coefficient describes the rate of energy absorption in the medium and $[(\mu_{en})_m]_{air}$ describes the rate of energy absorption in air. In equation (4.3), the expression may be simplified to

$$D_{med} = (f)(X) \quad \ldots\ldots\ldots\ldots\ldots\ldots\ldots\ldots\ldots\ldots \quad (4.4)$$

Where, $f = 0.869\frac{[(\mu_{en})_m]_{med}}{[(\mu_{en})_m]_{air}}$ $\ldots\ldots\ldots\ldots\ldots\ldots\ldots\ldots\ldots\ldots$ (4.5)

The expression denoted as f is known as the f-factor and varies with the nature of the absorbing medium and the energy of the radiation.

The f-factor is used to compute the absorbed dose D in rad in a medium receiving an exposure X in roentgens. The f-factor is plotted in Fig.4.5 for air, water, fat, muscle and compact bone as a function of photon energy.

4.2.3. Interaction with Fat

X and gamma rays photons with energy less than about 35 keV interact in soft tissue primarily by the photoelectric effect, with a probability for interaction that varies roughly as Z^3 [29]. Compared to muscle and bone, fat has a higher concentration by weight of hydrogen (~11%) and carbon (~57%) and a lower concentration of nitrogen (~1%), oxygen (30%) and high-Z trace elements (<1%)[30]. Hence, the effective atomic number of fat (Z_{eff} = 5.9-6.3) is less than that for soft tissue (Z_{eff} = 7.4) or bone (Z_{eff} = 11.6-13.8), and low-energy photons are attenuated less rapidly in fat than in an equal mass of soft tissue or bone [30,31]. The reduced attenuation in fat is reflected in a lower f-factor for photons of low energy in this body constituent (Fig.4.5).

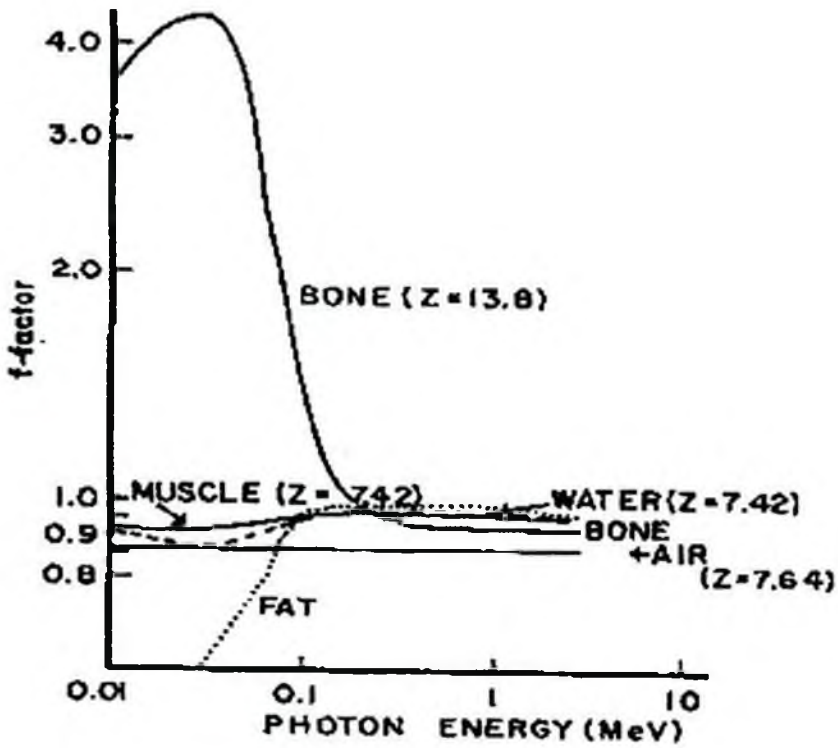

Figure 4.5. The f-factor for conversion between roentgens and rads for air, water and different constituents of the body, plotted as a function of photon energy.

X- and gamma rays photons of higher energy interact primarily by Compton scattering, with a probability that varies with the electron density of the attenuating medium but not with the atomic number. The electron density of hydrogen is about twice that of other elements [29], because the nucleus of hydrogen contains no neutrons. Since more hydrogen is present in fat than in other body constituents, more Compton interactions occur in fat than in an equal mass of muscle or bone. For photons of intermediate energy, therefore, the f-factor for fat exceeds that for other body constituents.

The f-factor cannot be defined rigorously for X- and gamma rays photons with energy greater than about 3 MeV, because the roentgen is not applicable to photons of higher energy. Consequently, f-factors in Fig.4.5 are plotted to only 3 MeV. The attenuation of X- and gamma rays photons in fat may be estimated from attenuation measurements in mineral oil or polyethylene, because the effective atomic numbers, densities and electron densities of these materials are close to those for fat [29].

4.2.4Interaction with Soft Tissue

The effective atomic number and density of body fluids and soft tissue, excluding fat, are almost identical to those for water, because soft tissue is roughly 75% water and body fluids are (85-100)% water. Soft tissue often is simulated by a water filled phantom or by Plexiglas, Mix-D or pressed wood (e.g., Masonite).

Hydrogen is absent from air, but contributes about 10% of the weight of muscle. Consequently, the electron density is greater for muscle than for air, and the f-factor muscle exceeds that for air (Fig. 4.5).

4.2.5 Interaction with Bone

The effective atomic number and physical density (kg/cu m) are greater for bone than for soft tissue. Hence, X- and gamma rays photons attenuated more rapidly in bone than in an equal volume (not necessarily mass) of soft tissue, and the absorbed dose is reduced to structures beyond bone. On the other hand, the absorbed dose to soft tissue adjacent to or enclosed within bone may be increased by photoelectrons liberated as photons interact with high-Z atoms (e.g., atoms of phosphorus and calcium) in bone.

4.2.6 Dose to Soft Tissue near an Interface between Soft Tissue and Bone

Under conditions of electron equilibrium, the absorbed does D in rad to compact bone is

$$D = (f)(X) \quad \text{.....} \quad (4.6)$$

where X is the exposure in roentgens and f is the f-factor for the bone exposed to photons of a particular energy (Fig.4.5). To compute the absorbed dose to soft tissue beyond the range of electrons escaping from bone, the f-factor for soft tissue is used in equation (4.6). The absorbed dose to soft tissue near bone is less than the absorbed dose in bone but greater than the absorbed dose in soft tissue beyond the range of electrons from bone. In tissue irradiated by diagnostic or orthovoltage X rays, the region of increased dose to soft tissue extends over a distance of 100μ or less from an interface between soft tissue and bone. These transition zones of increased doses are illustrated in Figures 4.6 to 4.8 for X-ray beams of different qualities.

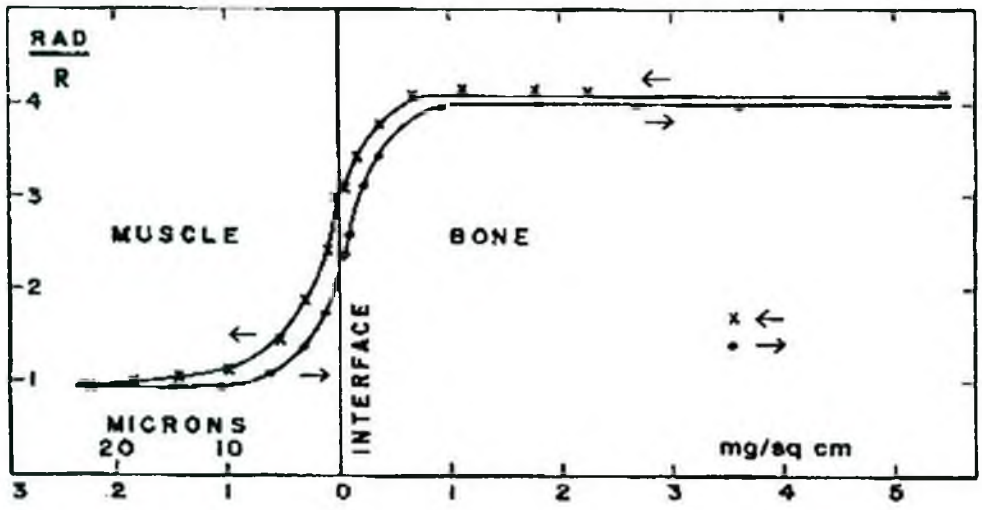

Figure 4.6. The f-factor (rad/R) for 50kVp, 0.08 mm Cu HVL X-rays near an interface between soft tissue and bone. Arrows indicate the direction of the X-ray beam.

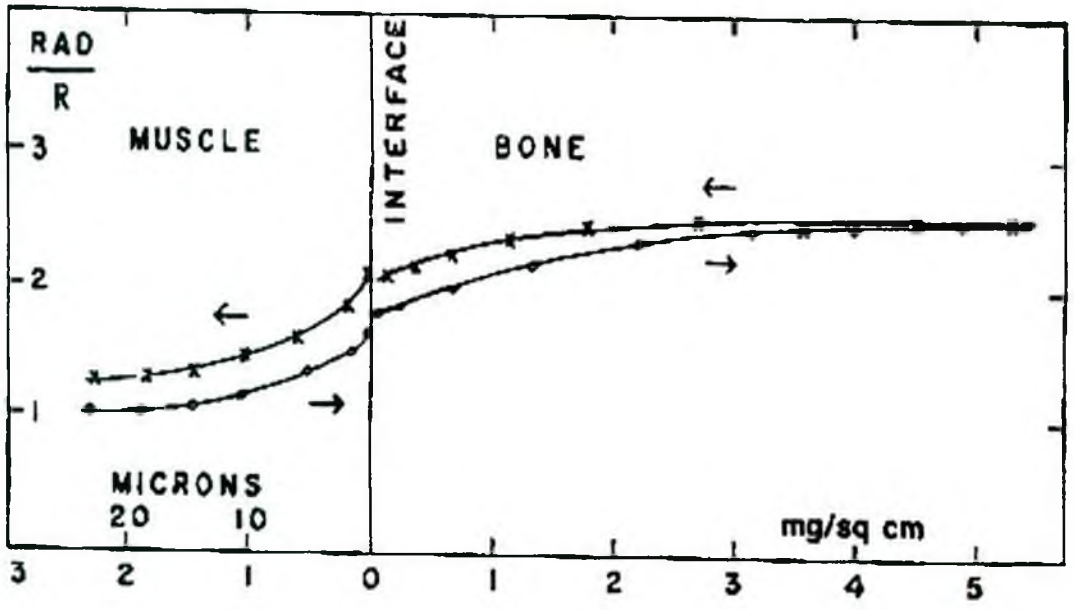

Figure 4.7. The f-factor (rad/R) for 140 kVp, 0.7 mm Cu HVL X-rays near an interface between soft tissue and bone. Arrows indicate the direction of the X-ray beam.

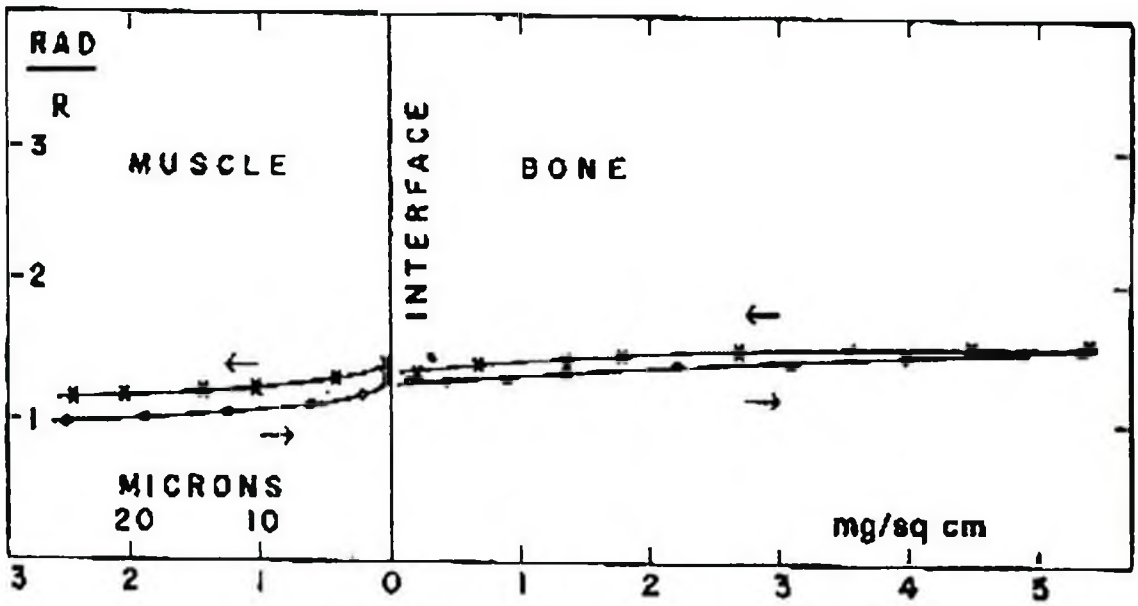

Figure 4.8. The f-factor (rad/R) for 220-kVp 2.1 mm Cu HVL X-rays near an interface between soft tissue and bone. Arrows indicate the direction of the X-ray beam.

The radiation dose delivered to soft tissue near an interface between soft tissue and bone may be computed with an f-factor intermediate between those for soft tissue and bone. The f-factor for photons of different energies are plotted in Figure 4.9 as a function of the distance form the interface.

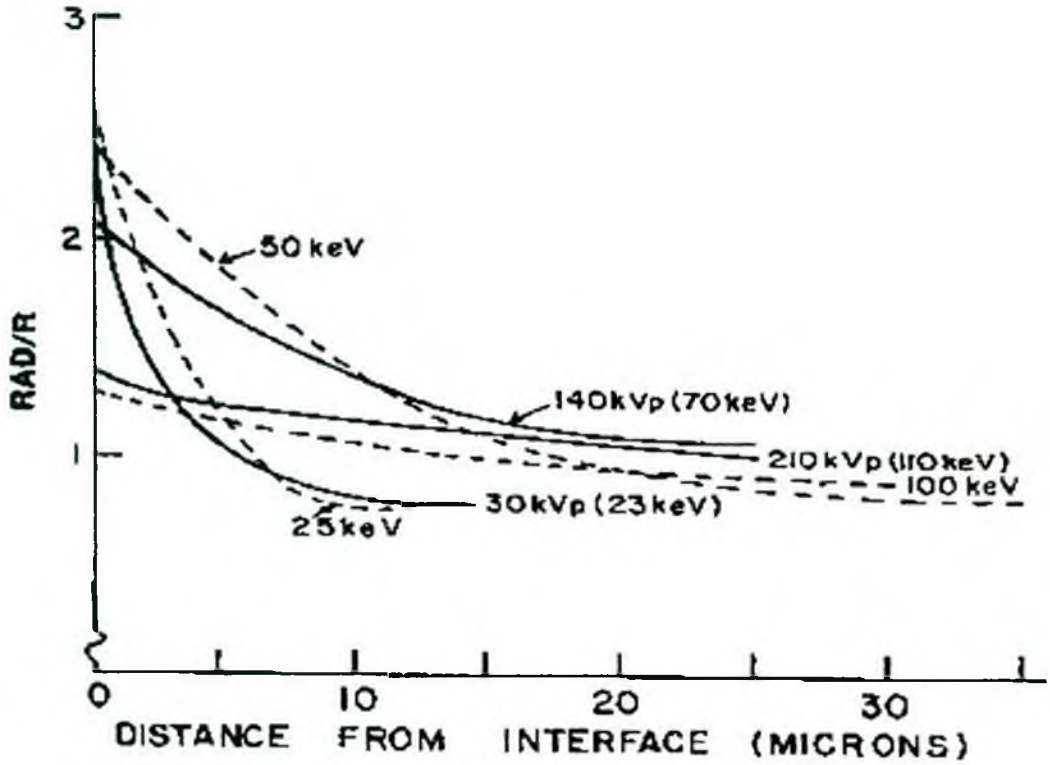

Figure 4.9. Calculated and measured f-factors as a function of the distance in soft tissue from an interface between soft tissue and bone.

4.2.7 Dose to Soft Tissue within Bone

Soft tissue that occupies cavities within bone includes the soft tissue components of the Haversian system. These components include osteocytes about 5μ in diameter, connective tissue along the walls of Haversian canals, and blood vessels in the walls of the canals. Hacersian canals vary from 50 to 100μ in diameter. In trabecular bone, spaces occupied by bone marrow are relatively large, averaging about 400μ across.

The absorbed dose in small (diameter<1μ) inclusions of soft tissue within compact bone is close to that computed with equation (4.6) and an f-factor

for bone. The dose to larger (diameter>1μ) soft tissue inclusions is less than that estimated with equation (4.6) an f-factor for bone. In larger inclusions, the absorbed dose varies from a maximum at the bone-tissue interface to a minimum at the center of the inclusion (Fig. 4.10).

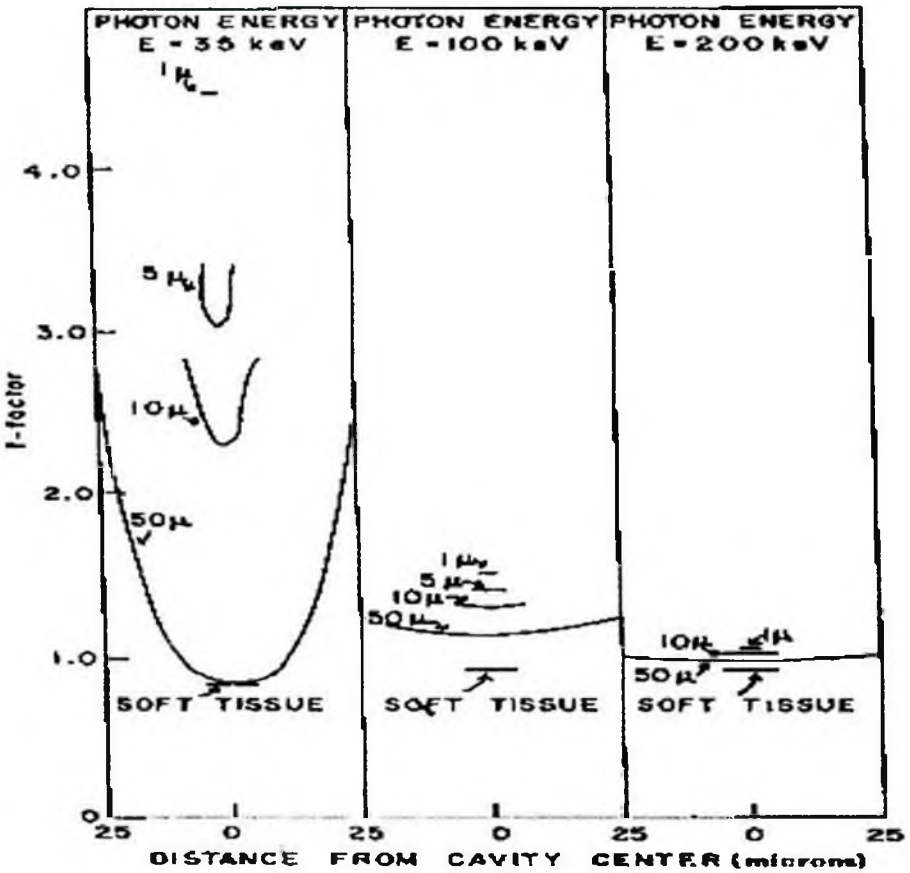

Figure 4.10. The f-factor for phantoms of various energies, as a function of the distance from the center of cavities of different sizes. A layer of bone around cavity provides electron equilibrium.

The absorbed dose across these larger inclusions is difficult to determine. Average f-factors in Table 4.2 were computed by Spiers[32] for osteocytes, for typical soft tissue inclusions excluding bone marrow and for the soft tissue lining of a typical Havesian canal. The average f-factors are highest for

osteocytes because these components occupy very small cavities. Haversian canals, on the average, are much smaller than spaces in trabecular bone that contain bone marrow, and the average dose to bone marrow usually is not much greater than that delivered to soft tissue in the absence of bone. The increase in average absorbed dose in bone marrow spaces of different sizes is plotted in Figure 4.11 as a function of the energy of incident photons. For marrow cavities of all sizes, the increase in dose is less than 50% of the dose to soft tissue without bone.

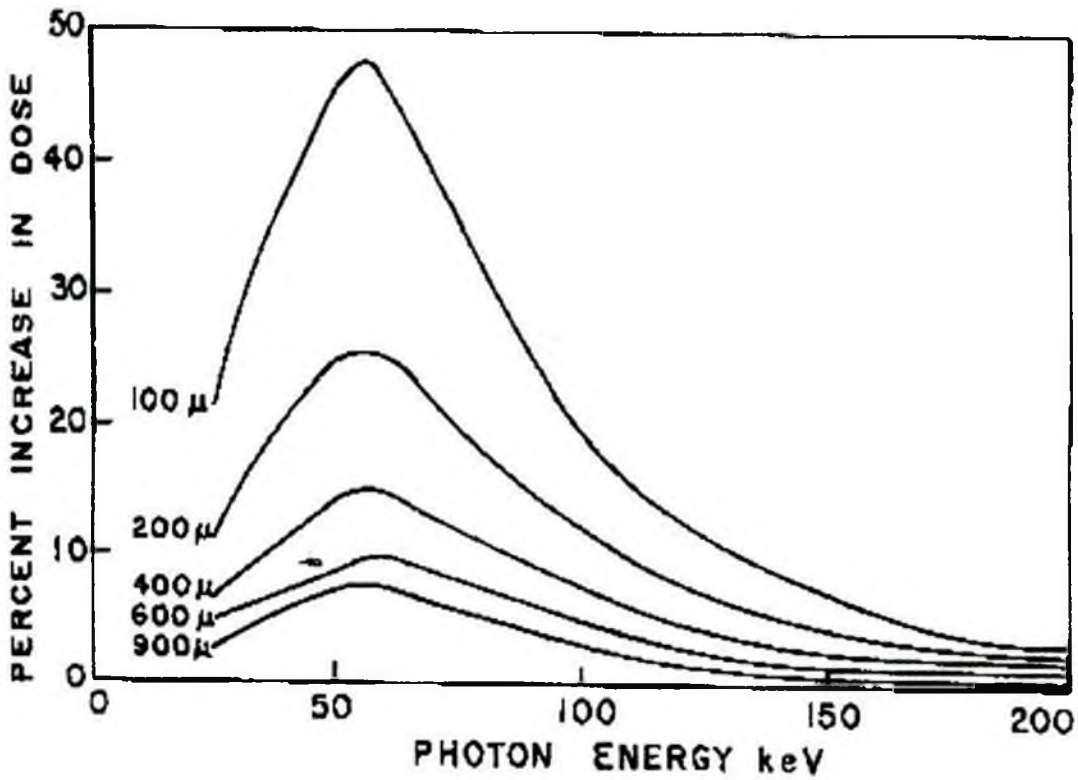

Figure 4.11. Percent increase in average absorbed dose to bone marrow cavities, averaged over cavities of various sizes.

Table 4.2: Average f-factors for inclusions of soft tissue in bone[32]

Photon Energy (keV)	Osteocyte 5 μ diameter	Typical soft tissue in bone	10 μ lining of 50 μ Haversian canal
25	2.80	1.73	1.50
35	3.12	2.05	1.76
50	3.25	2.27	1.89
75	2.40	1.85	1.60
100	1.52	1.36	1.26
200	1.05	1.03	1.02

The probability of pair production increases with the atomic number of the attenuating medium. Consequently, the dose delivered by high-energy photons is greater in bone than in soft tissue. For example, the dose delivered by 10-MeV photons is about 15% greater in bone than in soft tissue receiving an identical exposure. Electrons released during pair production interactions have an average range of about 2-3 cm in soft tissue and more than 1 cm in bone. For a thickness of bone less than that required for electron equilibrium, it is difficult to estimate the dose to bone and to soft tissue inclusions within bone.

4.2.8 Dose to Soft Tissue beyond Bone

The dose delivered to soft tissue by X or gamma ray is reduced by bone interposed between the soft tissue and the surface. The reduction in absorbed dose to soft tissue is influenced by:

1. The increased attenuation of primary photons in bone caused by the higher atomic number and density of this constituent of tissue.

2. Changes in the amount of radiation scattered to soft tissue beyond the location of bone. These changes depend upon many factors, including field size, quality of radiation and the distance between the bone and the soft tissue of interest.

Low energy X or γ ray photons are attenuated primarily by photoelectric interactions, and the attenuation of these photons is much greater in bone than in an equal mass of soft tissue or fat. For photons of higher energy, Compton scattering replaces photoelectric absorption as the on the electron density of the attenuating medium, but not on its atomic number. The electron density is slightly less for bone than for soft tissue or fat, and the energy absorbed per gram of bone is slightly less than the energy absorbed per gram of muscle or fat exposed to photons of intermediate energy. However, the physical density (kg/cu m) of compact bone is almost twice the density of fat or muscle. Therefore, the energy absorbed per unit volume of compact bone is almost twice that absorbed in an equal volume of fat or muscle exposed to an identical number of X or γ ray photons of intermediate energy.

The effect of bone the radiation exposure and absorbed dose at various depths within a patient exposed to diagnostic or orthovaltage X rays illustrated in Figure-4.12. The radiation exposure, which always is measured in a small volume of air, is reduced at locations B, C and D by bone interposed between the locations and the surface. The reduction in exposure at these locations reflects primarily the increased attenuation of photons in overlying bone, the dose absorbed in bone is increased at A, B and C, because the attenuation of diagnostic or orthovoltage X rays increases with the atomic number of the attenuating medium. The absorbed dose is

reduced to soft tissue beyond bone because a greater number of photons are removed from the beam by the overlying bone.

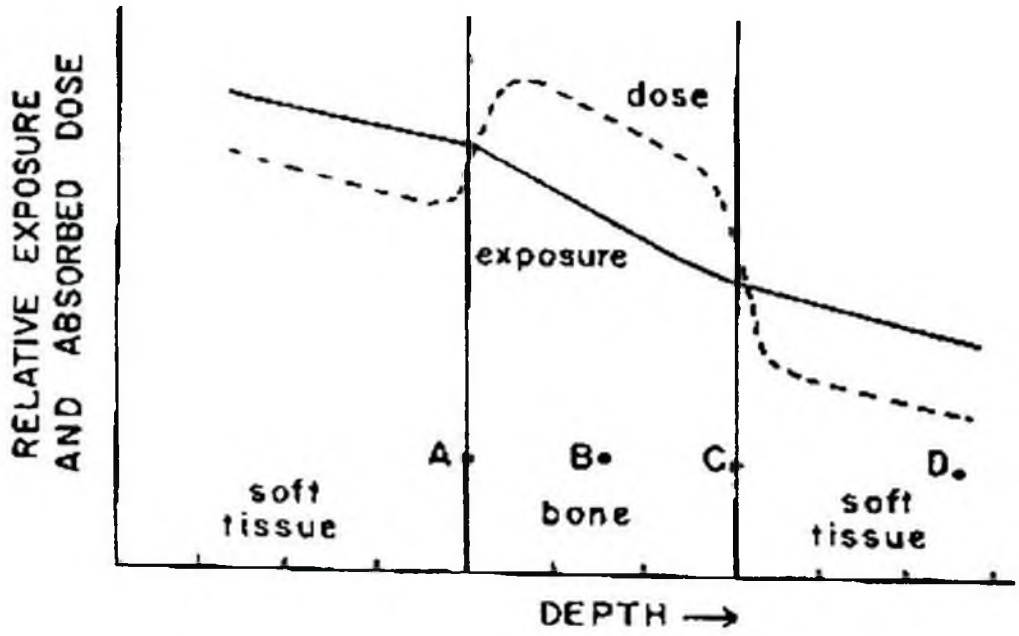

Figure 4.12. Radiation exposure and absorbed dose plotted as a function of depth in soft tissue containing bone.

4.3 Determination of Absorbed Dose to Water

4.3.1 Reference Conditions and Correction Factors

The calibration factor for an ionisation chamber is the ratio of the true value of the quantity to be measured to the indicated value under reference conditions. The reference condition is described by a set influence quantities for which the calibration factor is valid without further correction factors. Influence quantities are defined as quantities not being the subject of the measurement but yet influencing the quantity under measurement. They may be of different nature as, for example, temperature, humidity and mains

voltage; they may arise from the dosimeter (e.g. ageing, zero drift, and warm-up) or may be quantities related to the radiation field (e.g. radiation quality, dose rate, field size, depth in a phantom). In calibrating a dosimeter as many influence quantities as possible are kept at reference conditions. However, some influence quantities, e.g. temperature, pressure, humidity, dose rate and polarity effect, must generally be corrected for to yield the 'influence' corresponding to the reference conditions [3]. Reference conditions for both calibration of ionisation chambers and measurement of absorbed dose, related to the radiation field, are Tables 4.3 and 4.4.

Table-4.3: Reference conditions of the irradiation geometry for the calibration of an ionisation chamber 'free in air'.

Radiation beam	Radiation quality	Distance from the source to the center of chamber cavity	Field size in cm × cm
Low energy X-ray (10 kV-100 kV)	0.03 mm Al<HVL≤2 mm Al	Usual treatment (calibration) distance	3 × 3
Medium energy X-ray (100 kV-300kV)	2 mm Al< HVL <3 mm Cu	Usual treatment (calibration) distance	10 × 10
Co-60 gamma radiation	$(\bar{h}\nu) = 1.25$ MeV	1 m	10 × 10

Table-4.4: Reference condition of the irradiation geometry for absorbed dose measurements using an ionisation chamber in a phantom.

Radiation beam	Beam quality	Reference depth in phantom in cm[a]	Effective point of measurement of the ionisation chamber	SSD	Field size in cm × cm
Low energy X-rays	0.03 mm Al < HVL ≤ 2 mm Al	Surface	Front surface of the plane parallel chamber	Usual treatment distance	3 × 3
Medium energy X-rays	2 mm Al < HVL ≤ 3 mm Cu	5	Center of cylindrical chamber		10 × 10
^{137}Cs gamma rays		5	0.35r[b]		10 × 10
^{60}Co gamma rays		5	0.5r[b]		10 × 10
High energy X-rays	$TPR_{10}^{20} \leq 0.70$	5	0.75r[b]		10 × 10
	$TPR_{10}^{20} > 0.70$	10	0.75r[b]		10 × 10
Electrons	$\overline{E_0}/MeV < 5$	R_{100}	0.5r[b]		10 × 10[c]
	$5 \leq E_0/MeV < 10$	R_{100} or 1[d]	0.5r[b]		10 × 10[c]
	$10 \leq E_0/MeV < 20$	R_{100} or 2[d]	0.5r[b]		10 × 10[c]
	$20 \leq E_0/MeV < 50$	R_{100} or 3[d]	0.5r[b]		15 × 15[c]

[a] Depth of $P_{eff.}$ [c] Field sizes for energy range measurements are different.

[b] The distance $^{z}p_{eff} - {}^{z}p$ is given, see Fig. 11 (Reference-21, p-38 [d] The larger depth should always be chosen.

As a general recommendation is given in reference[21], when using therapy accelerators and X-ray units, it is strongly recommended that an additional monitoring dosimetry system be used during the experimental procedure to account for fluctuations in the radiation output.

4.3.2 Warm-up Effect

Before measurements are made with an ionisation chamber system, enough time should be allowed for the chamber to reach thermal equilibrium and for the measuring system to warm up.

4.3.3 Leakage Current

The leakage current should be measured and should be insignificant compared to that current obtained for the real measurements. It should be observed that the leakage might be much larger during an irradiation than the leakage without irradiation [21].

4.3.4 The Polarity Effect

The polarity effect of the chamber must be checked, particularly for plane parallel ionisation chambers, and found to be within the given limits in Table-1 of the reference [3] page-10,. This effect may be large for electrons of low energy. The mean value of the currents (or charges) measured at both polarities of the chamber voltage is considered to be the best approximation of the true ionisation current. However, in practical situations, only one

polarity is generally used, as the correction using the chambers discussed here should small

4.3.5 Temperature and Pressure

Since the ionisation chamber is not sealed and communicate to the outside atmosphere, its response is affected by air temperature and pressure. In accordance with the gas laws, the density of air in the chamber volume will likewise depend on these atmospheric conditions. The density or the mass of air in the chamber volume will increase as the temperature decreases or pressure increases. Since exposure is given by the ionisation charge collected per unit mass of air, the chamber reading for a given exposure will increase as the temperature decreases or as the pressure increases.

Standard laboratories calibrate chambers under the conditions present at the time of calibration. This factor is then converted to specific atmospheric conditions, namely, 1013 millibar (760 mm Hg) pressure and 22°C temperature. The correction $C_{T,P}$ for conditions other than the above reference conditions can be calculated.

$$C_{T,P} = \left(\frac{1013}{P}\right) \times \left(\frac{273.5 + t}{295.5}\right) \quad \text{..... (4.7)}$$

where P is the pressure in millibar and t is temperature in degree Celsius. The second bracketed term gives the ratio of temperature t to the reference temperature (22°C), both converted to the absolute scale of temperature (in Kelvin) by adding 273.5 to the Celsius temperatures.

4.3.6 Humidity

The humidity of the ambient air has-except when hygroscopic wall materials are used such as A-150 plastic or nylon–only a minor influence on the charge produced in the chamber cavity. If the calibration factor is related to a relative humidity of 50% then in a range of 20% to 70% relative humidity no correction is needed for temperatures ranging between 15°C and 25°C. If, on the other hand, the calibration factor is related to dry air and measurements are taken between 20% and 70% relative humidity and in a temperature range of 15°C to 25°C, a correction factor k_h = 0.997 is adequate for ^{60}Co gamma radiation [22].

4.3.7 Recombination

The incomplete efficiency in collecting charge in the cavity volume due to ion recombination requires the use of a correction factor. The effect depends on the geometry of the chamber, the applied collection voltage, and the rate of charge production by the radiation. In the case of pulsed radiation, especially with scanned beams, the correction factor for recombination becomes rather important. On the other hand, for continuous radiation (gamma ray beams) the effect is usually very small.

It is possible to derive a correction factor p_s theoretically, using the theory of Boag[23-26] but as the magnitude of the correction depends on the position of the central electrode and this could accidentally be changed without an external change in the chamber, it is recommended here that an experimental procedure be used to determine the recombination factor.

The so-called 'two-voltage' method [27] is, owing to its simplicity, the method to be used. It is based on two measurements of the collected charge, Q_1 and Q_2, using different voltages V_1 (the normal operating bias voltage) and V_2 for the same irradiation conditions. The ratio V_1/V_2 should be equal to or greater than 3. Many of the commercially available ionization chamber instruments provide multiple bias voltages while some others can easily be modified to do so.

The recombination correction factor p_s at the normal operating bias voltage V_1 can then be obtained from a quadratic equation that has been fitted to the numerical solutions of the expressions for pulsed and pulsed scanned radiation

$$p_s = a_0 + a_1\left(\frac{Q_1}{Q_2}\right) + a_2\left(\frac{Q_1}{Q_2}\right)^2 \quad \text{.....} \quad (4.8)$$

where a_i are constants.

4.3.8 Chamber calibration factor, N_x

This factor which is characteristic of the chamber, its volume, and its build up cap- is determined by exposing it to a ^{60}Co beam of known exposure rate and /or comparing its response with a chamber of known exposure calibration factor for ^{60}Co. Specially constructed spherical, graphite ionization chambers of known volume are used to calibrate the cobalt beam in terms of exposure rate. N_x provided by the U.S. calibration laboratories is normalized to 22°C and 760 mm Hg. Calibration of the electrometer, if

detached, is provided separately. Exposure measured in ^{60}Co beam is given by

$$X = M.N_x.N_{el}. \quad \ldots\ldots\ldots\ldots\ldots\ldots\ldots\ldots\ldots\ldots\ldots\ldots \quad (4.9)$$

Where X is the exposure at a point corresponding to the center of the chamber when the chamber is not there; M is the reading corrected for temperature and pressure and N_{el} is the electrometer calibration factor, if separate from the chamber. The above equation functionally defines N_x.

4.3.9 Cavity-gas calibration factor, N_{gas}

It is defined as dose to the gas in the chamber per unit charge or electrometer reading. D_{gas} is simply given by $J_{gas} = \left(\frac{\overline{W}}{e}\right)$, where J_{gas} is the charge per unit mass of cavity gas and $\left(\frac{\overline{W}}{e}\right)$ is the average energy expended per unit charge of ionization produced in the gas.

4.3.10 Wall correction factors, A_{wall}, β_{wall}, P_{wall}

The A_{wall} correction factor occurs in the N_{gas} formula and accounts for attenuation and scatter of photons in the wall and build-up cap of the chamber when exposed in air to ^{60}Co γ ray beam.

β_{wall} is the quotient of absorbed dose to collision part of kerma in the wall under the conditions of transient electronic equilibrium . β_{wall} accounts for the difference between the point of interaction and the point of energy deposition. Its value is taken to be 1.005 for ^{60}Co[4].

P_{wall} is a correction factor that accounts for the difference between the composition of the chamber wall and the phantom as it pertains to photon beam interactions in the user's beam. This factor depends on beam energy, wall thickness, wall composition, and the fraction α of the cavity ionization contributed by electrons originating in the chamber wall.

4.3.11.The perturbation correction factor, p_u

For electron radiation perturbation correction factor takes into account the difference in scattering in the phantom material and in the air cavity [3]. For photon beams it must be considered that electrons are produced and stopped differently in the chamber wall material and in water. In the computation it is always assumed that the measurement in the water phantom is carried out without a buildup cap. The perturbation correction effect p_u can then be approximately calculated from the equation by Almond and Svensson [28].

$$p_u = \frac{\alpha S_{wall,air}\left(\frac{\overline{\mu}_{en}}{\rho}\right)_{w,wall} + (1-\alpha)S_{w,air}}{S_{w,air}} \qquad \text{..... (4.10)}$$

where α is the fraction of the total ionization produced in the air in the cavity by electrons arising in the chamber wall and $S_{wall,air}$ is the stopping power ratios for different chamber materials.

Chapter 5

5. Materials and Methods

5.1 Introduction

Before treating by radiotherapy the vital organs within a radiation field, which is not our target, is to be protected by shielding, is one of the major concerns.

For proper treatment the dose should be homogeneous. For this critical task special filters or absorbing blocks are placed in the path of a beam to modify its isodose distribution. The most commonly used beam-modifying device is the *wedge filter*. This is a wedge-shaped absorber, which causes a progressive decrease in the intensity across the beam, resulting in a tilt of the isodose curves from their normal positions. In actual wedge filter design, the sloping surface is made either straight or sigmoid in shape; the latter design is used to produce straighter isodose curves.

Relatively superficial tumors, extending from the surface to a depth of several centimeters, can be irradiated by two "wedged" beams directed from the same side of the patient. It is seen that in the region of overlap of the beams, the dose distribution is nonuniform. The dose is the highest in the superficial or proximal region of overlap and falls off to lower values toward the deeper areas. By inserting appropriate wedge filters in the beam and positioning them with thick ends adjacent to each other, the angled field distribution can be made fairly uniform.

The main goal of the radiotherapy for cervix cancer treatment is to maximize the dose at lesions (tumor volume) and minimize the dose below the tolerance level in surrounding normal tissue like as rectum and urinary bladder during the ca-cervix treatment planning. Conventional rectangular block shields the rectum area and urinary bladder and the resultant dose fall off is very rapid beyond point A. To overcome this problem, an alternative method has been developed to protect the unnecessary central axis radiation

dose to the critical organ by the device of "Wedge shaped Mid-line Block"(WMLB). The dose limitation of the rectum (anal canal) and bladder region should be maintained by using the newly developed idea for the treatment protocol.

5.2 Block in the Treatment Planning

5.2.1 Field blocks

The shaping of treatment fields is primarily dictated by tumor distribution-local extensions as well as regional metastases. Not only should the dose to vital organs not exceed their tolerance but also the dose to normal tissue, in general, should be minimized. As long as the target volume includes, with adequate margins, the demonstrated tumor as well as its presumed occult spread, significant irradiation of the normal tissue outside this volume must be avoided as much as possible. These restrictions can give rise to complex field shapes, which require intricate blocking.

The frequency and complexity of field shaping vary from institution to institution. However, if complex techniques involving elaborate blocking are used often, it is necessary to establish a rational system of field shaping.

5.2.1.1Block Thickness

Shielding blocks are most commonly made of lead. The thickness of lead required to provide adequate protection of the shielded areas depends on the beam quality and the allowed transmission through the block. A primary beam transmission of 5% through the block is considered acceptable for most clinical situations. If n is the number of half-value layers to achieve this transmissions,

$$\frac{1}{2^n} = 0.05$$

or

$$2^n = \frac{1}{0.05} = 20$$

or

$$n \log 2 = \log 20$$

or $$n = \frac{\log 20}{\log 2} = 4.32$$

Thus a thickness of lead between 4.5 and 5.0 half-value layers would give less than 5% primary beam transmission and is, therefore, recommended for most clinical shielding.

Shielding against primary radiation for superficial and orthovoltage beams is readily accomplished by thin sheets of lead that can be placed or molded on to the skin surface. However, as the beam energy increases to the megavoltage range, the thickness of lead required for shielding increases substantially. The lead blocks are then placed above the patient supported in the beam on a transparent plastic tray, called the *shadow tray.* Table 5.1 gives the recommended lead shield thickness for various quality beams.

Although the primary beam transmission can be reduced further by using extra thick blocks, the reduction in dose in the shielded region may not be that significant due to the predominance of scattered radiation from the adjoining open areas of the field.

5.2.1.2 Block Divergence

Ideally, the blocks should be shaped or tapered so that their sides follow the geometric divergence of the beam. This minimizes the block transmission penumbra (partial transmission of the beam at the edges of the block). However, divergent blocks offer little advantage for beams with large geometric penumbra. For example, in the case of ^{60}Co, the sharpness of the beam cutoff at the block edge is not significantly improved by using divergent blocks. Also, for some clinical situations this sharpness is not critical or worth the time required for making divergent blocks, which have to be invariably custom designed for a given treatment setup. Therefore, most institutions keep a stock of straight-cut blocks of various shapes and dimensions.

Divergent blocks are most suited for beams having small focal spots. Since the sides of these blocks follow beam divergence, one can reduce the lateral dimensions by designing the shields for smaller source-to-block distances without increasing the block transmission penumbra.

Table 5.1

Recommended Minimum Thickness of Lead for Shielding

Beam Quality	Required Lead thickness
1.0 mm Al HVL	0.2 mm
2.0 mm Al HVL	0.3 mm
3.0 mm Al HVL	0.4 mm
1.0 mm Cu HVL	1.0 mm
3.0 mm Cu HVL	2.0 mm
4.0 mm Cu HVL	2.5 mm
^{137}Cs	3.0 cm
^{60}CO	5.0 cm
4 MV	6.0 cm
6 MV	6.5 cm
10 MV	7.0 cm
25 MV	7.0 cm

Approximate values to give $\leq$ 5% primary transmission.

5.2.2 FIELD SHAPING

5.2.2.1 Custom Blocking

Although a number of systems have been used for field shaping, the one introduced by Powers et al. [33] is most commonly used in radiotherapy This system uses a low melting point alloy, Lipowitz metal (brand name, Cerrobend), which has a density of 9.4 g/cm^3 at 20^0**C** (~83% of lead density). This material consists of 50% bismuth, 26.7% lead, 13.3% tin, and 10.0% cadmium [34]. The main advantage of Cerrobend over lead is that it melts at about 70^{0}C (compared with 327^{0}C for lead) and, therefore can be easily cast into any shape. At room temperature, it is harder than lead.

The minimum thickness of Cerrobend blocks required for blocking may be calculated from Table 5.1 using its density ratio relative to lead (e.g., multiply lead thickness by 1.21). In the megavoltage range of photon beams, the most commonly used thickness is 7.5 cm, which is equivalent to about 6 cm of pure lead.

The procedure for constructing Cerrobend blocks starts with a simulator radiograph or a port film on which the radiotherapist draws the outline of the treatment field indicating areas to be shielded. The film is then used to construct divergent cavities in a Styrofoam block that are used to cast Cerrobend blocks. Styrofoam-cutting device that consists of an electrically heated wire, which pivots about a point simulating the source or the x-ray target. The film, the Styrofoam block, and the wire apparatus are so adjusted that the actual treatment geometry (same source to film and source to block distances) is obtained. The lower end of the wire traces the outline on the film.

If "positive" blocks such as lung blocks are to be made, cavities are cut into the Styrofoam with the heated segment of the wire and subsequently filled with melted Cerrobend. If a "negative" block with central area open and peripheral areas blocked is desired, an inner cut is first made to outline the field opening. An outer rectangular cut is then made to define the collimator field 1-2-cm margin. The three Styrofoam pieces thus made are placed on a Lucite plate and carefully aligned relative to the central axis. The intermediate piece, corresponding to the areas to be shielded, is then removed and Cerrobend is poured into the cavity.

It is important that the Cerrobend is poured slowly to prevent formation of air bubbles. Also, Styrofoam block should be pressed tightly against a rubber pad at the bottom to avoid leakage of the metal. The inside walls of the cavity may be sprayed with silicone for easy release of the Styrofoam pieces from the block.

The blocks can be mounted on a Lucite plate, which is premarked with the central axis cross hair. Blocks can also be placed on a template made on a clear film by tracing the outline of the field at the shadow tray position while the port film outline is placed at the distance at which the radiograph was taken.

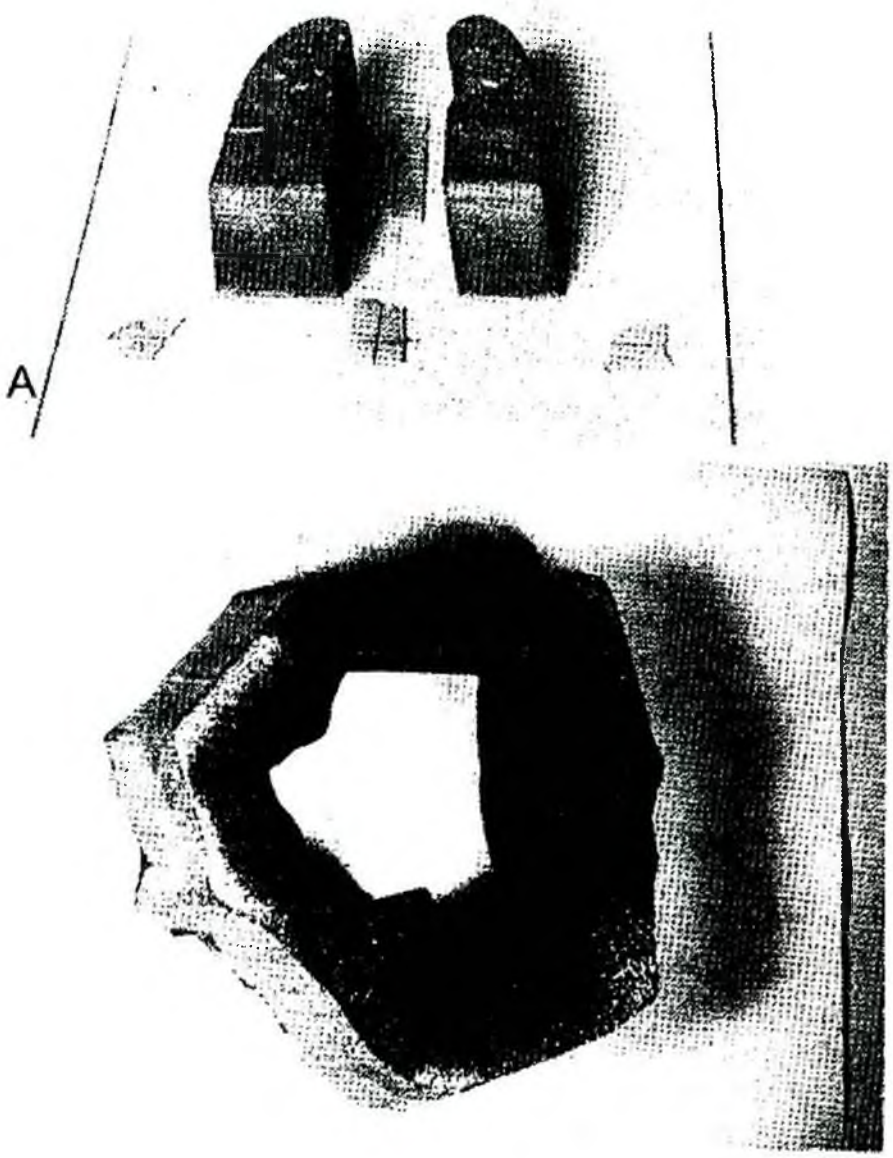

Figure 5.1. ***A*** and ***B*** shows examples of Cerrobend blocks, one constructed for shielding lungs and the other for a head and neck field.

5.2.2.2 Independent Jaws

Asymmetric fields are sometimes used to block off a part of the field without changing the position of the isocenter. Although blocking is often used to generate irregular field shapes, rectangular blocking can be easily done by independently movable collimators, or jaws. This feature is very convenient when matching fields or beam splitting. In the latter case, the beam is blocked off at the central axis to remove divergence. Whereas half-beam blocks have been used as beam splitters in the past, this can now be done simply by moving in the independent jaws.

Most modern machines are equipped with independently movable jaws. Some machines have one independent jaw, others have two independent pairs, and some have all four jaws as independent. Operationally, the independent jaw option is interlocked to avoid errors in the setting of symmetric fields, in which case the opposite jaws open or close symmetrically.

One of the effects of asymmetric collimation is the change in the physical penumbra and the tilt of the isodose curves toward the blocked edge (Fig. 5.3). This effect is simply the result of blocking, which eliminates photon and electron scatter from the blocked portion of the field, thereby reducing the dose near the edge. The same effect would occur on the isodose curves if the blocking were done with a lead or Cerrobend block on a tray.

When asymmetric fields are used, special considerations must be given to the beam flatness and the dosimetric parameters used to calculate monitor units. Khan et al. [2] have proposed a system of dose calculations for fields generated by asymmetric collimators.

5.2.2.3 Multileaf Collimators

A multileaf collimator (MLC) for photon beams consists of a large number of collimating blocks or leaves that can be driven automatically, independent of each other, to generate a field of any shape (Fig.5.3). The thickness of the leaves along the beam direction is sufficient to provide acceptably low beam transmission (e.g., $\leq$ 1%). The width of each leaf is usually about 1 cm as projected at the isocenter. The field edges are, therefore, formed stepwise, 1 cm wide.

Some MLC systems have double-focused leaves form a cone of irregular cross-section diverging from the source position and move on a spherical shell centered at the source. The rationale behind a double-focused MLC is to provide a sharpe beam cutoff at the edge. However, for high-energy beams this objective is achieved only to a limited extent, because the dose falloff at the edge is largely determined by scattered photons and electrons. Because double-focused MLCs are difficult to manufacture, some systems have been designed with rounded leaf edges and directions of travel perpendicular to the central ray. The purpose of rounded edges is to provide constant beam transmission through a leaf edge, regardless of its position in the field.

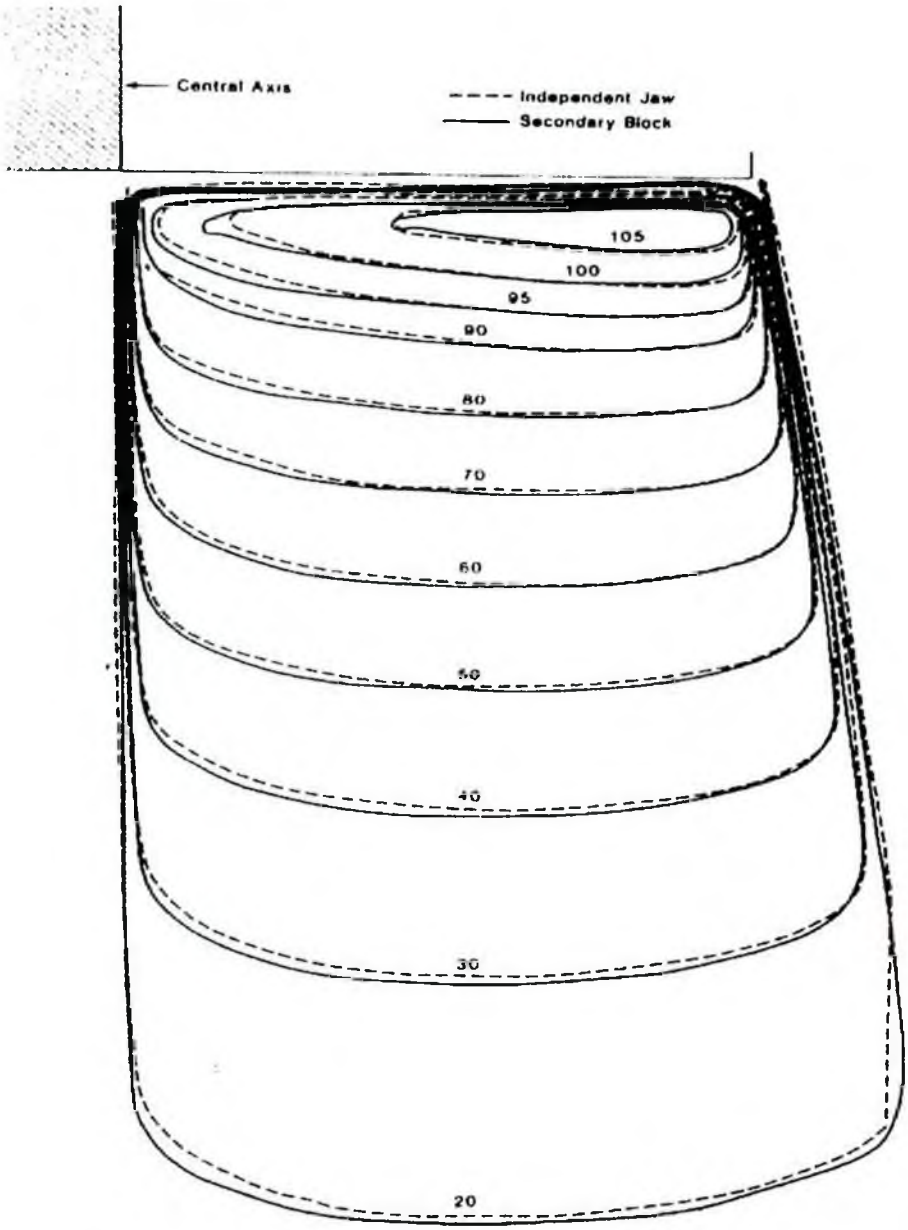

Figure 5.2. Comparison of isodose distribution with half the beam blocked by an independent jaw versus a block on a tray. Notice close agreement as well as the tilt of the isodose curves towards the blocked edge.

An important consideration in the use of MLCs for stationery fields is the conformity between the planned field boundary, which is continuous,

and the jagged stepwise boundary created by the MLC. The degree of conformity between the two depends not only on the projected leaf width but also on the shape of the target volume and the angle of rotation of the collimator. Optimization of MLC rotation and setting has been discussed by Brahme [35]. His analysis shows that the best orientation of the collimator is when the direction of motion of the leaves is parallel with the direction in which the target volume has the smallest cross-section.

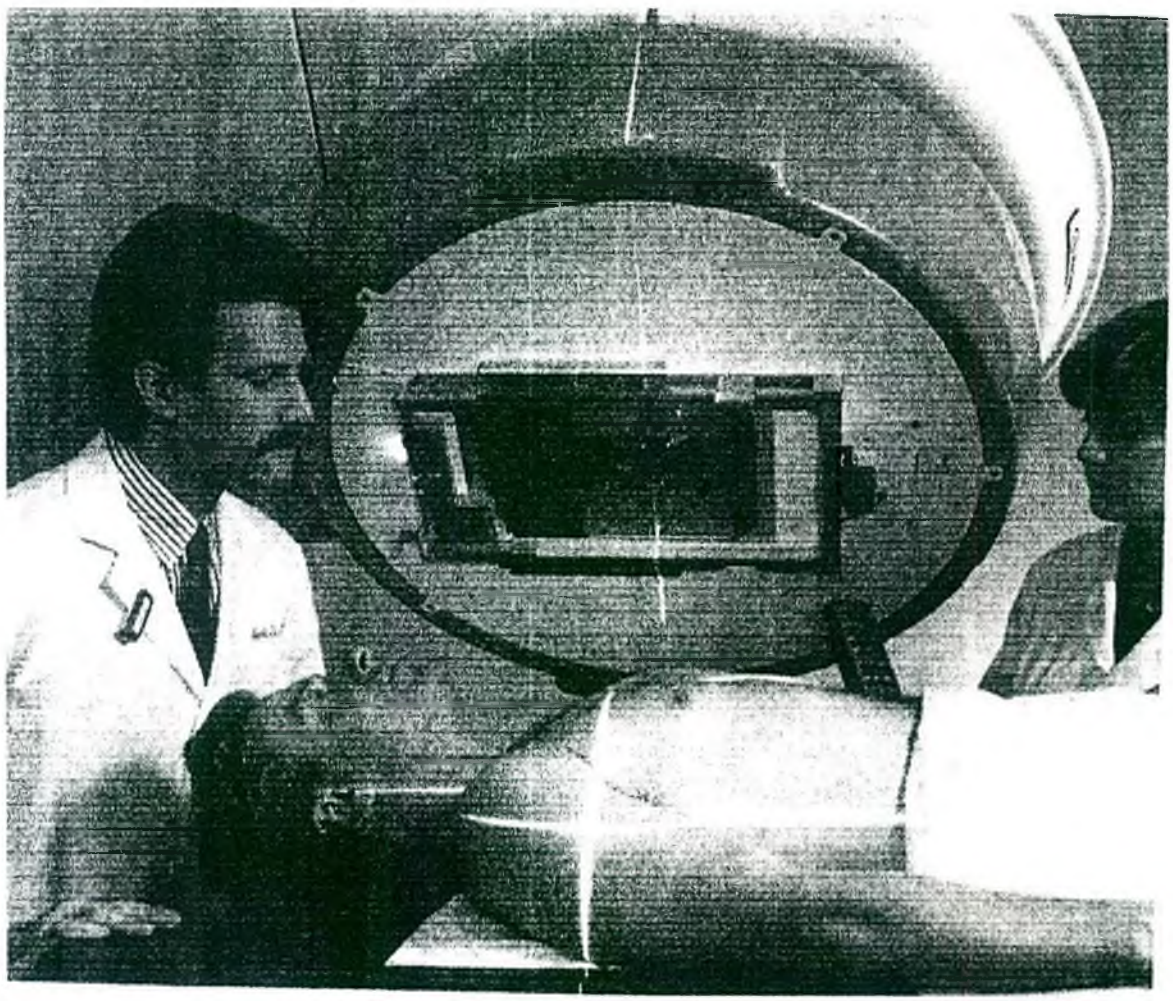

Figure 5.3. Varian multileaf collimator.

There are several potential applications of the MLC system: replacement of custom Cerrobend blocking; automatic beam shaping for multiple fields; dynamic conformal radiotherapy for which beams are shaped as they are rotated; and modifying dose distributions within the field by computer-

controlled dwell time of the individual leaves. Many of these functions are still under development and are not available routinely in the clinic. For more details the reader is referred to a review article by Mohan [36].

5.3 Wedge Filters

5.3.1. Introduction

Frequently, special filters or absorbing blocks are placed in the path of a beam to modify its isodose distribution. The most commonly used beam-modifying device is the *wedge filter*. This is a wedge-shaped absorber, which causes a progressive decrease in the intensity across the beam, resulting in a tilt of the isodose curves from their normal positions. As shown in Figure 5.4 the isodose curves are tilted toward the thin end, the degree of tilt depends on the slope of the wedge filter. In actual wedge filter design, the sloping surface is made either straight or sigmoid in shape; the latter design is used to produce straighter isodose curves.

The wedge is usually made of a dense material, such as lead or steel, and is mounted on a transparent plastic tray, which can be inserted in the beam at a specified distance from the source (Fig.5.5). This distance is arranged such that the wedge tray is always at a distance of at least 15 cm from the skin surface, so as to avoid destroying the skin-sparing effect of the megavoltage beam.

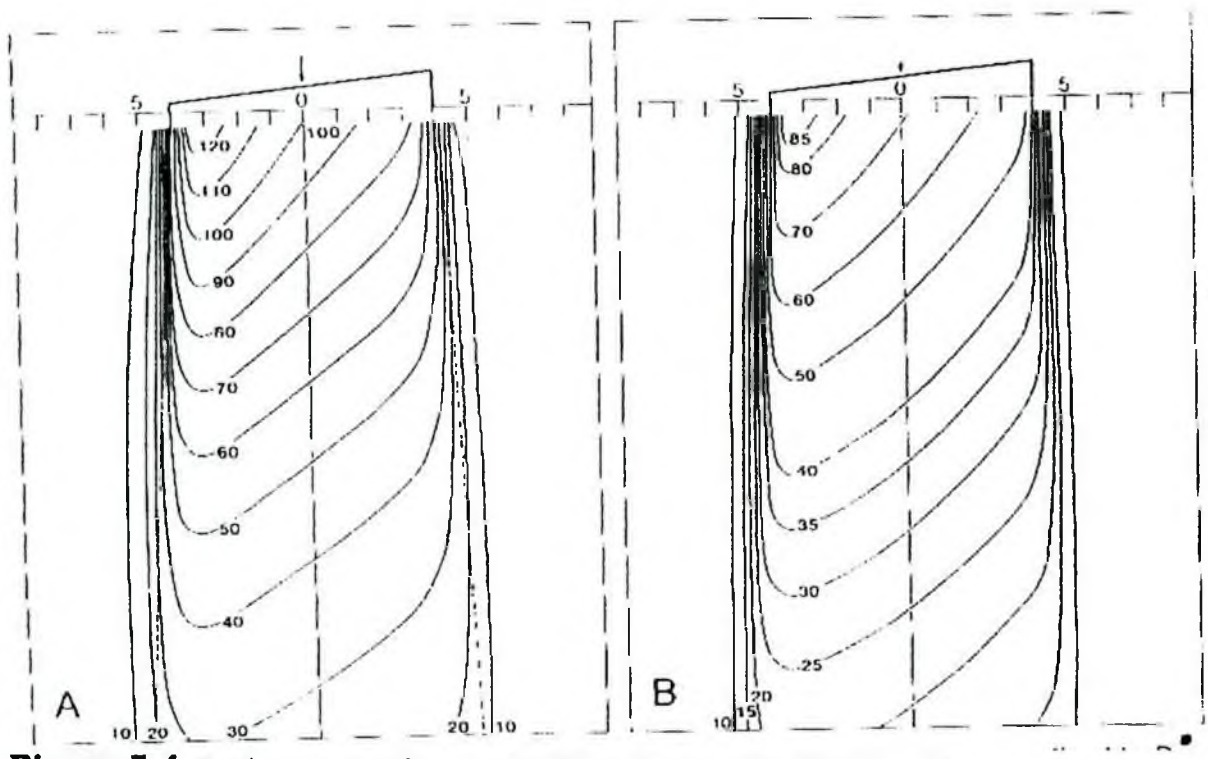

Figure 5.4. Isodose curves for a wedge filter. A, normalized to D_{max}. B, normalized to D_{max} without the wedge. ^{60}Co wedge angle=45^0, field size=8×10cm , SSD=80.

5.3.2 Wedge Isodose Angle

The term *wedge isodose angle* (or simply *wedge angle*) refers to "the angle through which an isodose curve is titled at the central ray of a beam at a specified depth". In this definition, one should note that the wedge angle is the angle between the isodose curve and the normal to the central axis, as shown in Figure 5.4. In addition, the specification of depth is important since; in general, the presence of scattered radiation causes the angle of isodose tilt to decrease with increasing depth in the phantom. However, there is no general agreement as to the choice of reference depth. Some choose depth as a function of field size (e.g., half or two-third of the beam width) while others define wedge angle as the angle between the 50% isodose curve and the normal to the central axis. The latter choice, however, becomes impractical when higher energy beams are used. For example, the

central axis depth of the 50% isodose curve for a 10-MV beam lies at about 18cm for a 10 X 10-cm fields and 100-cm SSD. This depth is too large in the context of most wedge filter applications. The wedge filters are mostly used for treating superficial tumors, e.g., not more than 10 cm deep. Therefore, the current recommendation is to use a single reference depth of 10 cm for wedge angle specification.

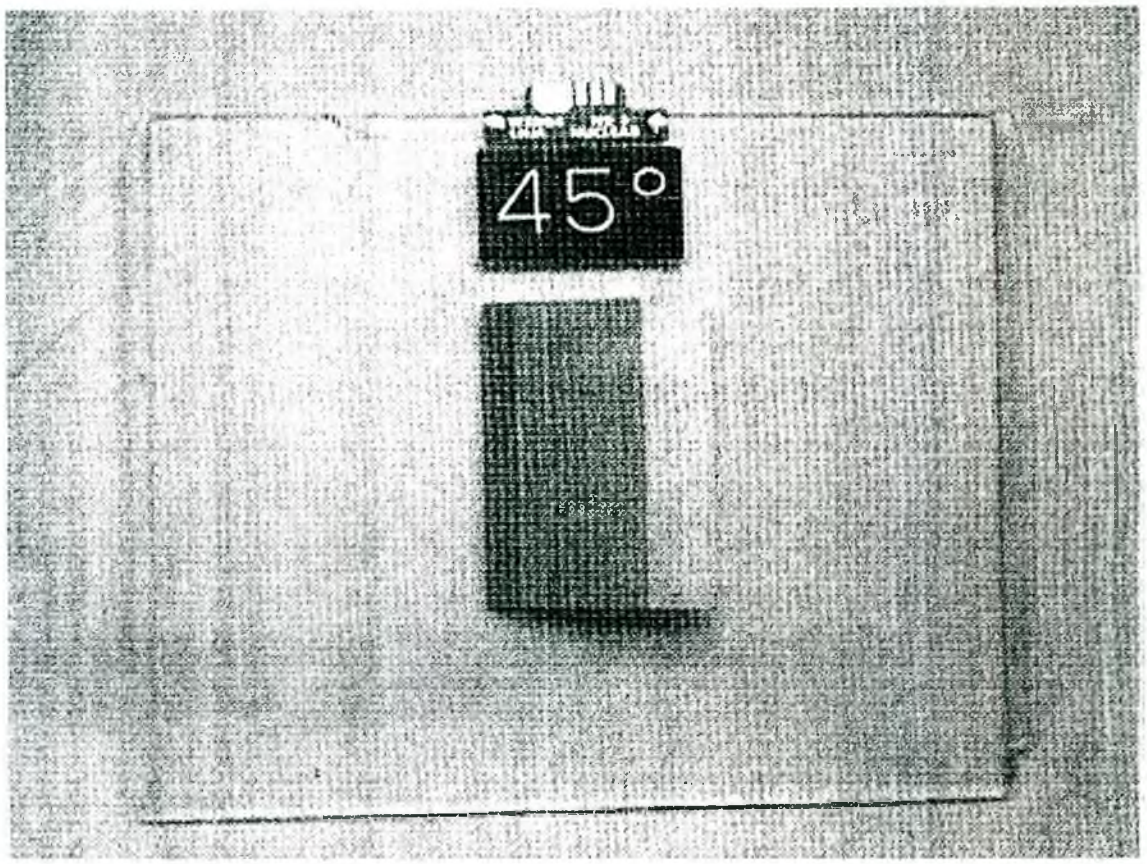

Figure 5.5. Photograph of a 45⁰ wedge filter for a 4-MV x-ray linac.

5.3.3 Wedge Transmission Factor

The presence of a wedge filter decreases the output of the machine, which must be taken into account in treatment calculations. This effect is characterized by the *wedge transmission factor* (or simply *wedge factor*), defined as the ratio of doses with and without the wedge, at a point in phantom along the central axis of the beam. This factor should be measured

in phantom at a suitable depth beyond the depth of maximum dose (e.g., 5 to n10 cm).

The wedge factor is sometimes incorporated into the isodose curves, as shown in Figure 5.4*B*. In this case, the depth dose distribution is normalized relative to the D_{max} without the wedge. For example, the isodose curve at depth of D_{max} is 72%, indicating that the wedge factor is already taken into account in the isodose distribution. If such a chart is used for isodose planning, no further correction should be applied to the output corresponding to the open beam should be used.

A more common approach is to normalize the isodose curves relative to the central axis D_{max} with the wedge in the beam. As see in Figure 11.6*A*, the 100% dose is indicated at the depth of D_{max}. With this approach, the output of the beam must be corrected using the wedge factor.

5.3.4 Wedge Systems

Wedge filters are of two main types. The first may be called the *Individualized wedge system*, which requires a separate wedge for each beam width, optimally designed to minimize the loss of beam output. A mechanism is provided to align the thin end of the wedge with the border of the light field (Fig 5.6*A)*. The second system uses a *universal wedge,* i.e., a single wedge serves for all beam widths. Such a filter is fixed centrally in the beam while the field can be opened to any size. As illustrated in Figure 5.6*B*, only a small part of this wedge, i.e., *ABC*, is effective in producing the given wedge angle. The rest (*ACDE*), being unwedded, does not contribute to the isodose tilt but unnecessarily reduces the beam intensity. Since the individualized system economizes on the beam output, it is preferred for use in cobalt teletherapy. The universal wedge, on the other hand, is useful for linear accelerator beams where the output is plentiful. From the setup and

treatment planning points of view, the universal wedge is simpler to use than the individualized filter

5.3.5 Effect on Beam Quality

In general, the wedge filter alters the beam quality by preferentially attenuating the lower-energy photons (beam hardening) and, to a lesser extent, by Compton scattering which results in energy degradation (beam softening). For the ^{60}Co beam, because the primary beam is essentially

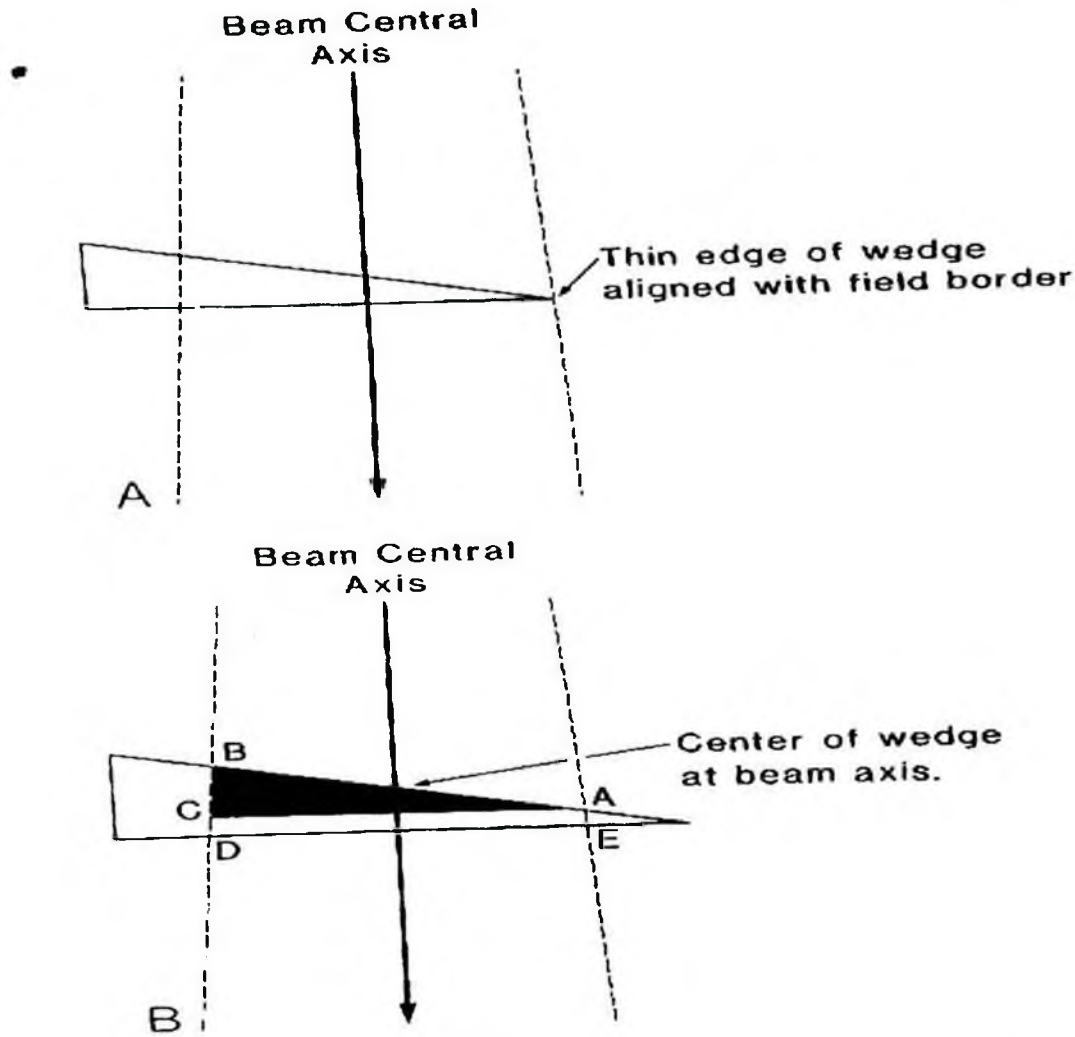

Figure 5.6. Schematic representation of (A) an individualized wedge for a specific field width in which the thin end of the wedge is always aligned with the field border and (B) a universal wedge in which the center of the wedge filter is fixed at the beam axis and the field can be opened to any width.

monoenergetic, the presence of the wedge filter does not significantly alter the central axis percent depth dose distribution. For x-rays, on the other hand, there can be some beam hardening, and consequently, the depth dose distribution can be somewhat altered, especially at large depths.

Although the wedge filters produce some change in beam quality, as noted above, the effect is not large enough to alter other calculation parameters such as the backscatter factor or the equivalent square, which may be assumed to be the same as for the corresponding open beams. Even central axis percent depth doses, TARs or TMRs may be assumed unchanged for small depths (e.g., less than 10 cm). The error caused by this assumption is minimized if the wedge transmission factor has been measured at a reference depth close to the point of interest.

5.3.6 Design of Wedge Filters

The design for wedge filters for megavoltage beams has been described by many authors. Here I will briefly present the design of a universal wedge filter following the technique of Aron and Scapicchio [37]. The principle of this method is to determine the ratio of percent depth doses at various points for wedged and nonwedged fields. The thickness of the wedge filter material at these points is then determined from these ratios and the knowledge of the half-value layer or the attenuation coefficient of the given beam for the filter material.

Figure 5.7 illustrates the design of a wedge filter. A line is drawn at a selected depth across the nonwedged field at the right angle to the central axis. This depth should correspond to the reference depth used for the wedge angle definition. Fan lines, representing rays from the source, are drawn at fixed intervals (e.g., 1 cm) on both sides of the central axis. A series of

parallel lines is drawn making an angle with the central axis equal to the complement of the given wedge angle and intersecting the central axis at the same points of intersections as the nonwedged isodose lines. A table is constructed which includes the percentage depth doses at the points of

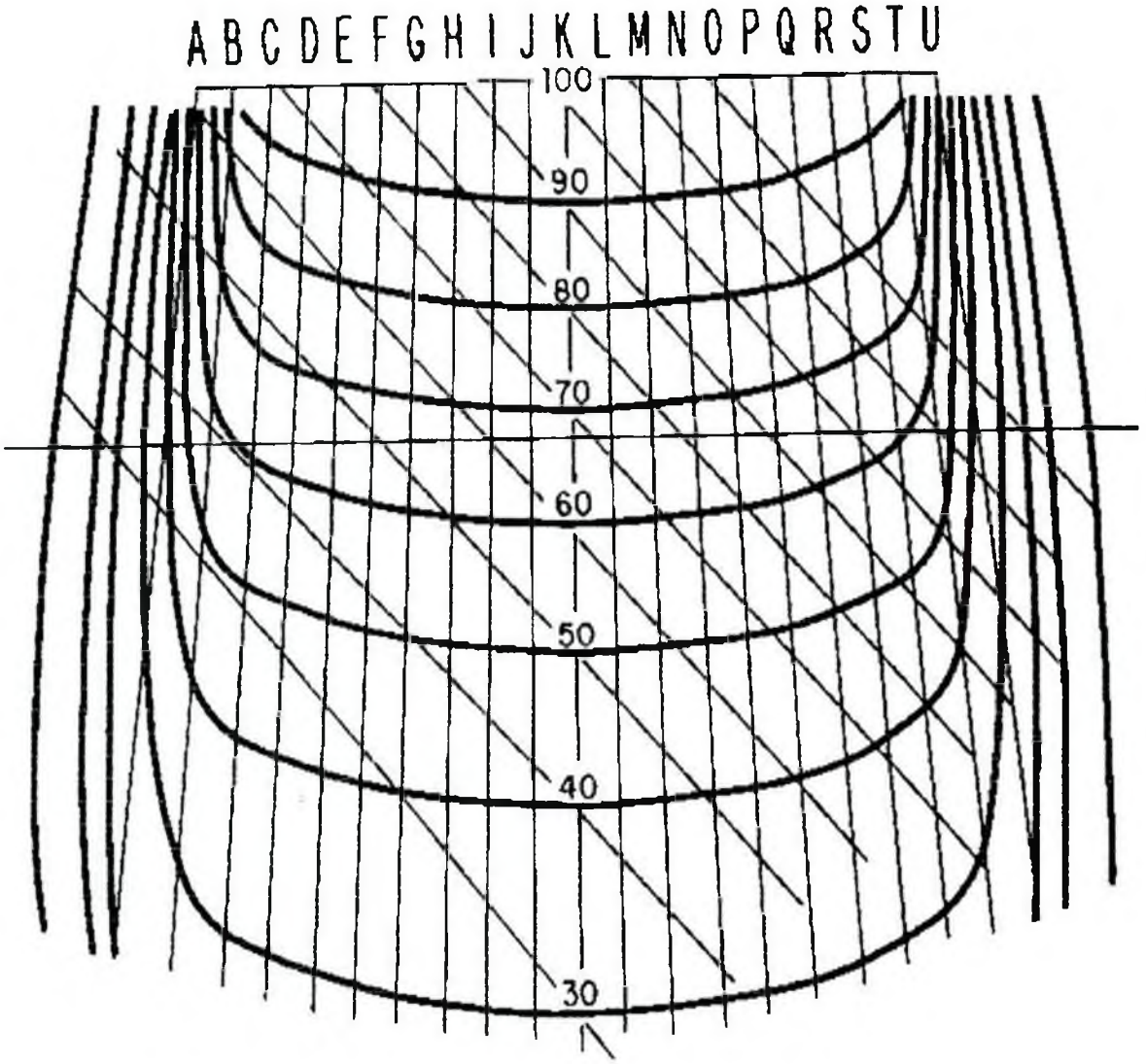

Figure 5.7. New 45^0 lines constructed parallel to one another, intersecting the central axis at same points of intersection as nonwedge isodose lines.

Table 5.2

Transmission Ratios for the construction of Wedge Filter

	A	B	C	E	G	I	K	M	O	Q	S	T	U
Nonwedge	40	55	62	65	67	68	68	68	67	65	62	55	40
isodose Wedge	35	39	41	47	53	60	68	76	86	95	105	110	115
isodose Ratio wedge/ nonwedege Transmission	0.875,	0.710	0.660	0.720	0.790	0.880	1.00	1.12	1.28	1.46	1.70	1.20	2.88
ratio mm Pb	0.387	0.425	0.462	0.515	0.59	0.66	0.75	0.86	1.0				
	15.2	13.6	12.2	10.5	8.3	6.5	4.	2.3	0				

intersection of the fan lines and the reference depth line for the nonwedged isodose curves and the wedged isodose lines (sloping lines). The ratio of the wedged to nonwedged values is calculated as shown in Table 5.2. These ratio are normalized to the highest value within the field (excluding the penumbra region) to give the relative transmission ratio along the designated fan lines. A wedge filter of a given material can then be designed to provide these transmission ratios.

5.4 wedge field technique

5.4.1 Introduction

Relatively superficial tumors, extending from the surface to a depth of several centimeters, can be irradiated by two "wedged" beams directed from the same side of the patient. Figure 5.8 shows isodose distribution of two angled beams with no wedge in the beams. It is seen that in the region of overlap of the beams, the dose distribution is quite nonuniform. The dose is highest in the superficial or proximal region of overlap and falls off to lower values toward the deeper areas. By inserting appropriate wedge filters in the beam and positioning them with thick ends adjacent to each other, the

angled field distribution can be made fairly uniform (Fig-5.8B). Each wedged beam in this has a reduced dose in superficial region relative to the deeper region so that the dose gradient in the overlap region is minimized. The dose falls off rapidly beyond the region of overlap or the "plateau" region, which is clinically a desirable feature.

There are three parameters that affect the plateau region in terms of its depth, shape, and dose distribution: θ, Φ, and S, where θ is the wedge angle Φ is the hinge angel, and S is the separation. These parameters are illustrated in Fig 5.9. The hinge angle is the angle between the central axes of the two beams and the separation S is the distance between the thick ends of the wedge filters as protected on the surface. Cohen and Martin [38] have discussed in detail how θ, Φ, and S can be adjusted to achieve a desired plateau.

There is an optimum relationship between the wedge angle θ and the hinge angle Φ which provides the most uniform distribution of radiation dose in the plateau:

$$\theta = 90^{0} - \Phi/2 \quad \text{..... 5.1}$$

This equation is based on the principle that for a given hinge angle the wedge angle should be such that the isodose curves from each field are parallel to the bisector of the hinge angle (see Fig.5.9). Under these conditions, when the isodoses are combined, the resultant distribution is uniform.

The equation 5.1, although helpful in treatment planning, may not yield an optimum plan for a given patient contour. The relationship assumes that the wedge isodose curves are not modified by the surface contour. In practice, however, contours are usually curves or irregular in shape and thus modify the isodose distribution for the wedged beams. As a result, the isodose curves for the individual fields are no longer parallel to the bisector of the hinge angle, thus giving rise to a nonuniform distribution in the

overlap region. This problem can be solved by using compensators, which make the skin surface effectively flat and perpendicular to each beam.

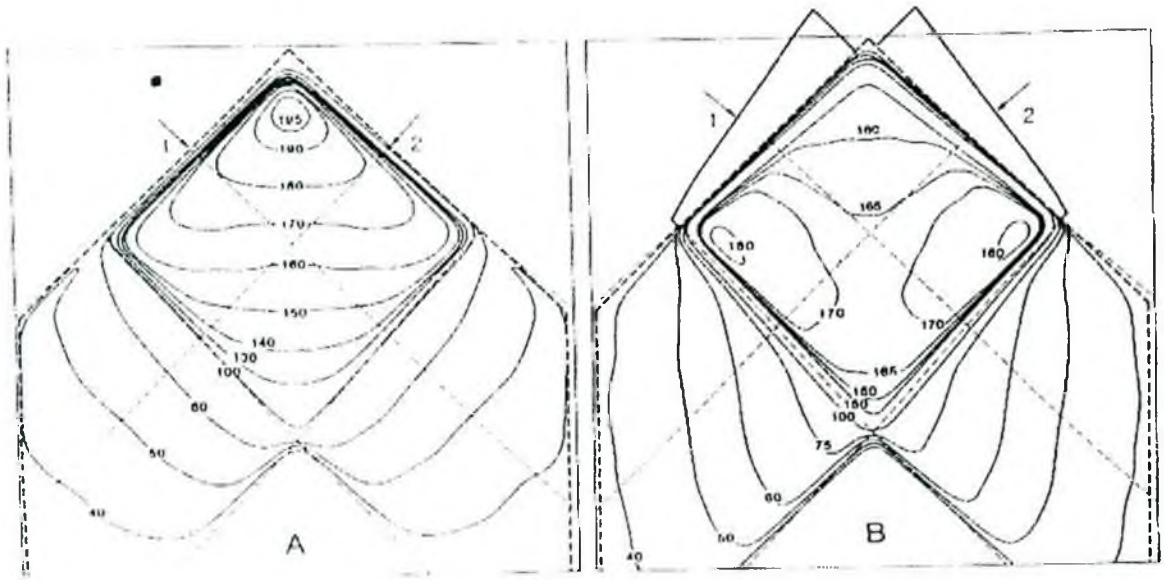

Figure 5.8. Isodose distribution for two angle beams. A, without wedges; B, with wedges; 4 MV, field size= 10×10cm, SSD=80cm, wedge angle=45°

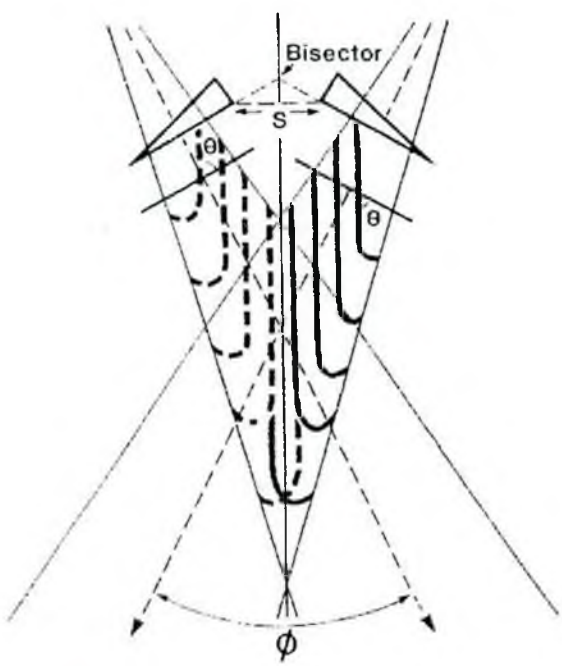

Figure 5.9. Parameters of the wedge beams, θ is wedge angle, Φ is hinge angle, and S is separation. Isodose curves for each wedge field are parallel to the bisector.

An alternative approach is to modify the wedge angle (using a different wedge angle filter from that given by Equation 5.1) so that a part of the wedge angle acts as a compensator and the rest as a true wedge filter. The main objective is to make isodose curves parallel to the hinge angle bisector. Although the latter approach obviates the need for a compensator, the determination of an optimum wedge angle may not be easy if planning is done manually. The former method, on the other hand, is well suited for manual calculations since all you need is a compensator and an atlas of precalculated isodose distributions for a variety of θ, Φ, and S values. This method, however, becomes technically difficult to implement if complicated secondary blocking is required in addition to the compensator and the wedge filter.

Equation 5.1 suggests that for each hinge angle one should use a different wedge angle. However, in practices, selected wedge angle, i.e., 15°, 30°,45°and 60°, are adequate over a fairly wide range of hinge angles.

In modern radiotherapy, complex treatment techniques are frequently used, which may involve wedge filters, compensators, field blocking, and field reductions, all for the same patient. Manual treatment planning is difficult for such cases. For this reason, in many institutions, all complex treatments, including wedged fields, are planned by computer as a matter of standard practices.

5.4.2 Uniformity of Dose Distribution

Since wedge pair techniques are normally used for treating small, superficial tumor volumes, a high dose region (hot spot) of up to +10% within the treatment volume is usually acceptable. These hot spots occur under the thin ends of the wedges and their magnitude increases with field size and wedge angle. This effect is related to the differential attenuation of the beam under the thick end relative to the thin end.

Generally, the wedge filter technique is suitable when the tumor is approximately from 0 to 7 cm deep and when it is necessary to irradiate from

one side of the skin surface. The most desirable feature of this technique is the rapid dose fall off beyond the region of overlap. This fall off can be exploited to protect a critical organ such as the spinal cord. Although wedge filters are invaluable in radiotherapy, some of these techniques are being replaced by electron beam techniques.

5.5 Planning and fabrication

5.5.1. Introduction:

Since 1989 a new protocol has been initiated for stage Ib, IIa and IIb for radical treatment for cancer of the uterine cervix. The irradiation consists of AP/PA external beam delivering 40Gy in 20 fraction over 4 week period (includes initial 10Gy open field and subsequent 30Gy using 'wedge shaped mid-line block) and two intracavitary insertions, at 2nd week of external irradiation and at the end of treatment [34]. The total dose delivered through intracavitary remains 60Gy and 68Gy to Point A for stage Ib, IIa and IIb respectively. The wedge shaped mid-line block was designed using the dose distribution for Fletcher-Suit applicator of typical configuration of ^{137}Cs pellet sources. This block was designed such that the fall of dose rate with an intracavitary application between point A and point B has been compensated by external irradiation. The common modality of treatment of early stage cervical cancers Ib,IIa and IIb cases is by combination if intracavitary applicator and external beam intracavitary irradiation delivers very high dose to the cervix and significantly reduces dose to the surrounding normal tissue and vital organs like rectum and urinary bladder. The dose to the parametrium is delivered by external beam either by AP/PA parallels opposed fields with central shielding for anterior and posterior fields. Although the conventional rectangular block shields cervix, rectum and urinary bladder, the resultant dose fall off is vary rapid beyond point A and results in dose inhomogeneity around target volume [4,5]. To overcome this problem an alternative method of central shielding may be adopted in radiotherapy by using a 'wedge shaped mid-line block (WMLB). The block is

similar to Ben Sischy's block, which was designed for linear arrangements sources for intrauterine and vaginal applicators. In order to get improved dose homogeneity around the target volume a wedge shaped block was introduced on either side of central rectangular block. The shape and thickness of wedge was designed from intracavitary dose distribution pattern. Uniform dose delivery to the treatment volume is prerequisite for the effective management of cancer by radiotherapy. For the treatment of cervical cancer or malignant lesion with radiation, a proper plan for determining the best method of delivering radiation dose to the tumor is mandatory. The dose distribution in the treatment volume should be as homogeneous as possible with necessary measurements, which sufficiently minimizes the radiation dose to the surrounding healthy tissue. Accurate patient dosimetry i.e. planning is only possible when sufficiently accurate dosimetric data are available from experimental measurements.

5.5.2 FIGO Staging for Cancer of the uterine cervix [39]

Stage 0: Carcinoma in situ, intraepithelial carcinoma (Case of 0 should not be included in any therapeutic statistics for invasive carcinoma.)

Stage I: Carcinoma strictly confined to the cervix (Extension to the corpus should be disregarded.)

Stage IA: Invasive cancer identified only microscopically. All gross lesions even with superficial invasion are stage 1B cancers. Invasion is limited to measured stromal invasion with maximum depth of 5.0 mm and no wider than 7.0mm.

IA_1: Measured invasion of stroma no greater than 3.0 mm in depth and no wider than 7.0 mm.

IA_2: Measured invasion of stroma greater than 3.0 mm and no greater than 5.0 mm and no wider than 7.0 mm.

Stage I B: Clinical lesions confined to the cervix or preclinical lesions greater than stage IA.

IB_1: Clinical lesions no greater than 4.0 cm size

IB_2: Clinical lesions greater than 4.0 cm in size.

Stage II: Carcinoma extends beyond the cervix but has not extended onto the pelvic wall. Carcinoma involves the vagina but not as far as the lower third.

IIA: No obvious parametrial involvement.

IIB: Obvious parametrial involvement

Stage **III**: Carcinoma has extended on to the pelvic wall. On rectal examination, there is no cancer free space between the tumor and pelvic wall. Tumor involves the lower third of the vagina. All cases with hydronephrosis or nonfunctioning kidney should be included, unless they are due to other causes.

IIIA: No extension onto the pelvic wall but involvement of the lower third of the vagina.

IIIB: Extension to the pelvic wall or hydronephrosis or nonfunctioning kidney.

Stage **IV**: Carcinoma has extended beyond the true pelvis or has clinically involved the mucosa of the bladder or rectum.

IVA: Spread to adjacent organs.

IVB: Spread to distance organs.

FIGO = International Federation of Gynecology and Obstetrics

5.5.3 Specification of dose tolerance [40]

1. Cervix uteri

Stage **I**A (Patients unsuitable for surgery): 67.5 Gy to point A from two Selection insertions at medium dose rate in 18-24 hours each.

Stage **I**B/**II**A small-volume (CT/MRI negative nodes): 55 Gy to point A from two Selection insertions or 5 to 7 fractions of 5-7 Gy with HDR brachytherapy followed by: external beam therapy to the pelvis with opposing fields and central lead shield.

36-40 Gy in 18 to 20 fractions given in 4 to 5 weeks.

All other stages (External beam therapy): 40-50 Gy in 20 to 25 fractions given in 4 to 5 weeks.

Intracavitary therapy: 25-30 Gy to point A from a single Selection insertion or 21-25 Gy to point A in 3 to 5 fractions (5-7 Gy per fraction) of HDR brachytherapy.

2. Rectum

Pre-operable dose

Eithe 44 Gy in 22 fractions given in 4.5 weeks, followed by surgery often 6to 8 weeks. (for fixed tumor).

Or 25 Gy in 5 fractions given in one week followed immediately by surgery (for mobile tumor).

This must be done using a 3 or 4 field plan.

Postoperative dose

45-50 Gy in 25 fractions given in 5 weeks. Where there is residual macroscopic disease, a further 10-15 Gy in 5-7 fractions may be given to a small volume to a total dose of 55-60 Gy in 6.5 to 7 weeks.

Local control is improved by increasing the total dose, but morbidity due to small bowel damage is often the dose-limiting factor, particularly if mobility is reduced by postoperative adhesions. It is desirable to image small bowel and shield it wherever feasible if high doses are given.

Inoperable or recurrent disease

45-50 Gy in 20-25 fractions given in 4 to 5 weeks.

For maximum local control where prolonged survival is expected, an additional 10- 15Gy in 5-7 fractions may be given to a small volume to a total dose of 55-60 Gy in 6.5 to 7 weeks.

3. Bladder

Radical treatment

Initial target volume (whole pelvis)

44 Gy in 22 fractions given in 4.5 weeks.

Boost to bladder along (after whole pelvis irradiation)

20 Gy in 10 fractions given in 2 weeks.

Small volume (bladder along)

64 Gy in 32 fractions given in 6.5 weeks.

Palliative treatment

35 Gy in 10 fractions given in two weeks

or 21 Gy in 3 fractions given in one week.

5.5.4 Description of wedge shape mid-line block

Wedge shaped mid-line block is not a general rectangular block. It is similar to Ben Sischy's block, which was designed for linear arrangements sources for intrauterine and vaginal applicators. In order to get improved dose homogeneity around the target volume a wedge shaped block was introduced on either side of central rectangular block. The shape and thickness of wedge was designed from intracavitary dose distribution pattern.

The bottom of block is square and the size is 6.8cm×6.8cm such that the magnifying block portion at 80cm SSD is to be 10cm×10cm. The center of the block is rectangular with thickness of 5.5cm and width is 2.72cm. such that the magnifying portion at 80 cm SSD is to be 4cm. From the top towards bottom the width increases by 0.23cm for a decrease of height by 0.5cm. So the side aspect of the block is looked wedge shaped slope. The picture of the block is shown in fig. (5.11).

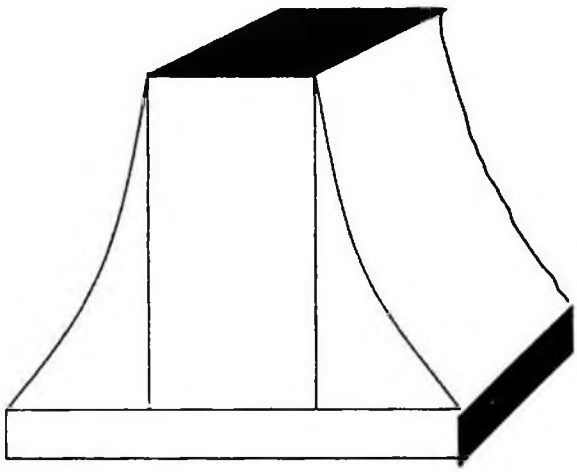

Figure 5.10
"Schematic diagram of "Wedge Shaped Mid-Line Block"

5.5.5 Fabrication

The wedge shaped mid-line block consists of a rectangular block at center and wedge shaped slope on the sides. The central rectangular portion covers with an area 10×4cm² and thickness of 5.5 HVLS ensure nearly 100% shielding up to point A the wedge shaped portion from point A to point B on both sides of the uterine canal gives an overall area of 10×10cm² at 80 cm Source to Surface Distance (SSD). Beyond the point B and up to the edge of the beam, there is no shielding, since the contribution

Figure 5.11

Fabricated wedge shaped mid-line block

of intracavitary dose is minimal. To estimate the thickness of the block between point A and B a lateral 100% dose profile was generated for Fletcher- Suit applicator at point A level using computer (Table 5.3). The fall-off dose between point A and B was estimated in percentage by normalizing the point A dose to100%.

Table-5.3

Estimation of thickness of wedge shape portion between point A and Point B

Off axis Distance from point A	Standard intracavitary dose fall off	Transmission required through block	Thickness required for (cm) ^{60}Co
0.0	100%	0	7.00
0.5	70%	30%	2.10
1.0	54%	46%	1.34
1.5	43%	57%	0.97
2.0	35%	65%	0.75
2.5	29%	71%	0.59
3.0	24%	76%	0.48

Linear attenuation coefficient (per cm) 0.5775

The Block was made in such a way that it blocks 100% open field radiation from central axis up to point A. To accomplish this critical task the standard measurements of table1 is transferred to foam sheet, cut by styroformer (block cutter) and a positive image of required Block [3] as made. This image was placed on a plane table and covered by some thin wet plaster of Paris (mixed with cloths) except the bottom. After it had hardened, the foam image was removed. In this way a negative image of the block was made. Then the molten alloy (lead, tungsten and tin alloy, melting point 70°C) was poured into it and allowed it to harden. In this way the "Wedge Shaped Mid-Line Block" was made. The schematic diagram and photograph of the block is shown in figure 5.11 and 5.12.

Real dimension measurements: In 80 SSD the magnification factor is 1.47. So if we want to block 10cm×10cm areas at 80cm SSD, the bottom of the fabricated alloy block should be 6.8cm×6.8cm (10/1.47=6.8). So the central axis line is 3.4cm (6.8/2=3.4) from the edge of the block. The A point of the

required field is 2cm from central axis and B point is 3cm from A point, so the A point of the fabricated alloy block is 1.36cm from central axis (2/1.47=1.36) and B point is 2.04cm from A point (3/1.47=2.04). Therefore, the rectangular portion of the fabricated alloy block is 2.72cm×6.8cm and height 5.5cm, which covers the field area of 10cm×4cm at 80 SSD. From the top of the rectangular portion the block increases both sides and make a wedge shape pattern. Increase in sideway length from the top towards bottom is calculated as follows:

Total change in length is 2.04cm(From A point to B point), height change (5.5-1)cm=4.5cm, so increase in wedge length per step is 2.04cm/4.5=0.45cm

. Therefore, increase in wedge length per 0.5cm is 0.45/2=0.23.

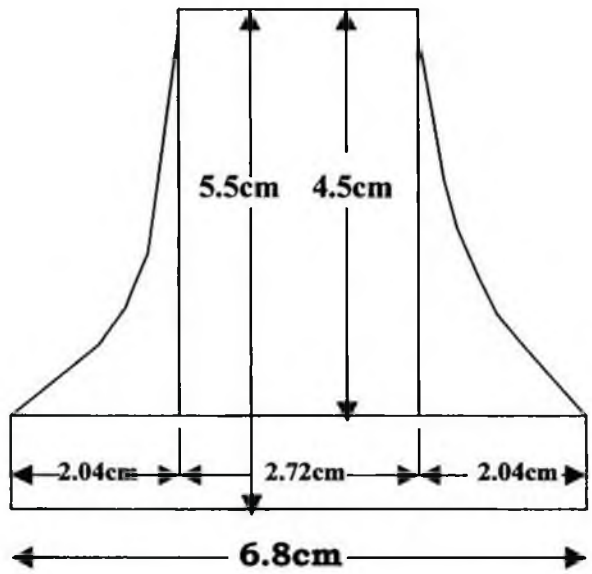

Fig5.12: Dimension measurement for fabricate a alloy block

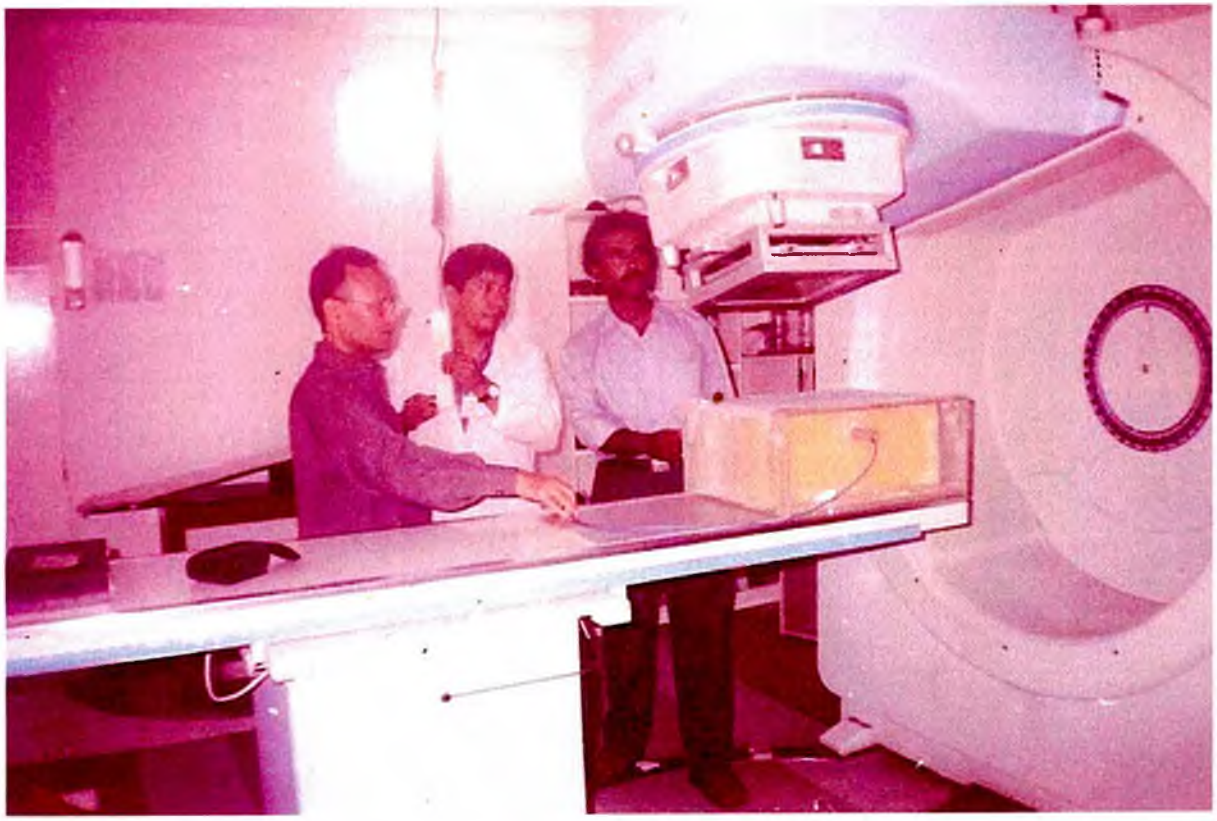

Fig 5.13

Dosimetric measurement by using WMLB

Fig. 5.14

Dosimetric measurement by using WMLB

Chapter 6

6. Results and Discussion

Chapter 6

6.Results and Discussions

6.Introduction:

Before using the WMLB for treatment, dosimetric measurements need to be carried out for symmetry verification, adequacy of thickness and output parameters. The symmetry verification of the block was tested using a check radiograph. Preliminary off axis measurements were carried out to confirm the adequacy of thickness using 0.6 cc ion chamber. An observed small variation of ±4% from the estimated values was corrected by adjusting the thickness of the block. Furthermore, symmetry check and the percentage transmission were confirmed by taking horizontal profile with farmer ion chamber. The symmetry and percentage transmission were found in agreement with the estimated values. The thickness profile and the linear attenuation coefficients for respective energies were measured by treatment planning computer system and isodose curves were generated. The horizontal profiles were found to be quite symmetric. For the purpose of dosimetric calculation with mid-line block the percentage depth dose (vertical profile) and output measurements were carried out in a solid phantom in unshielded region. These parameters were found to be matching with equivalent squares of 10^2-25^2 cm^2 for ^{60}Co gamma rays. The dosimetric measurements were performed from 10^2 to 25^2 sizes and the transmission has been within limited.

We took the open field-scanning dose of different field sizes like 5cm×5cm, 7cm×7cm, 10cm×10cm, 15cm×15cm and 20cm×20cm. We also took the block field-scanning dose of fields of 10cm×10cm, 15cm×15cm, 20cm×20cm and 25cm×25cm. We did not take the scanning dose for field sizes of 5cm×5cm and 7cm×7cm because our WMLB block covers an area of 10cm×10cm in 80 SSD, so no scanning dose found for the field sizes, which are below the field of 10cm×10cm.

Results:

The dose distribution for the field size of 5cm×5cm, 7cm×7cm, 10cm×10cm, 15cm×15cm and 20cm×20cm for the case of open field are shown in Fig. 6.1 to 6.5. It is clear from the graphs that the maximum doses at central axis are 420, 441.6, 485.9, 500 and 528.2 for field sizes of 5cm×5cm, 7cm×7cm, 10cm×10cm, 15cm×15cm and 20cm×20cm respectively. It is clear that the maximum dose increase slightly as the field size increases. It is belief that this increase is due to scattering. From the graph it is also seen that at the edges of any field size, the dose falls to approximately 50% of the central axis dose. The shape of the graph shows that symmetry against the central axis is very good.

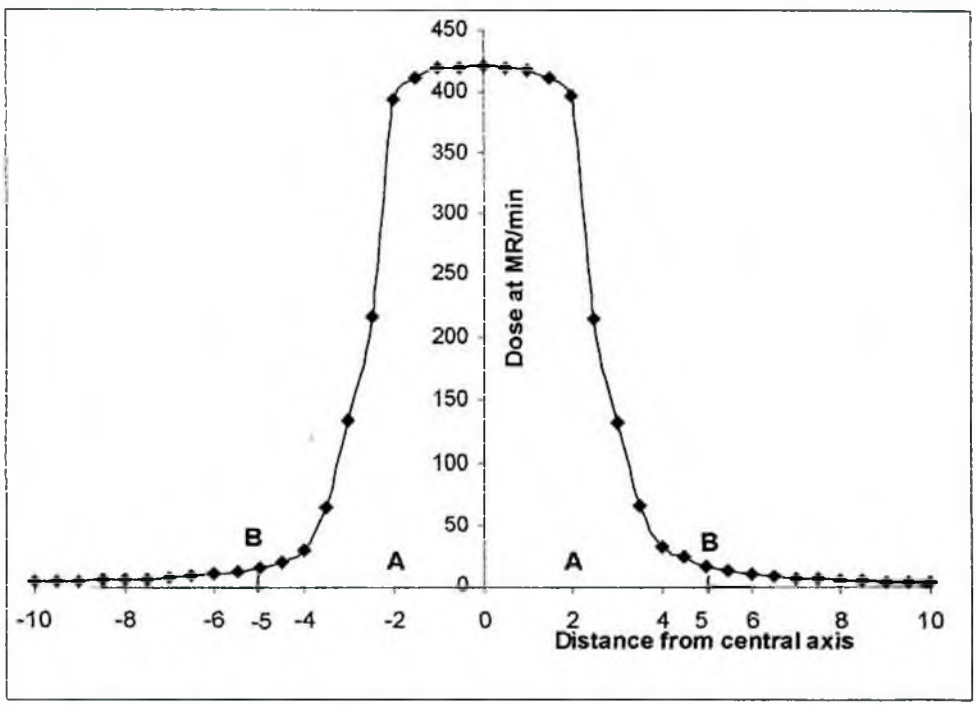

Fig 6.1: Field size 5cm×5cm

Distance vs open field scanning

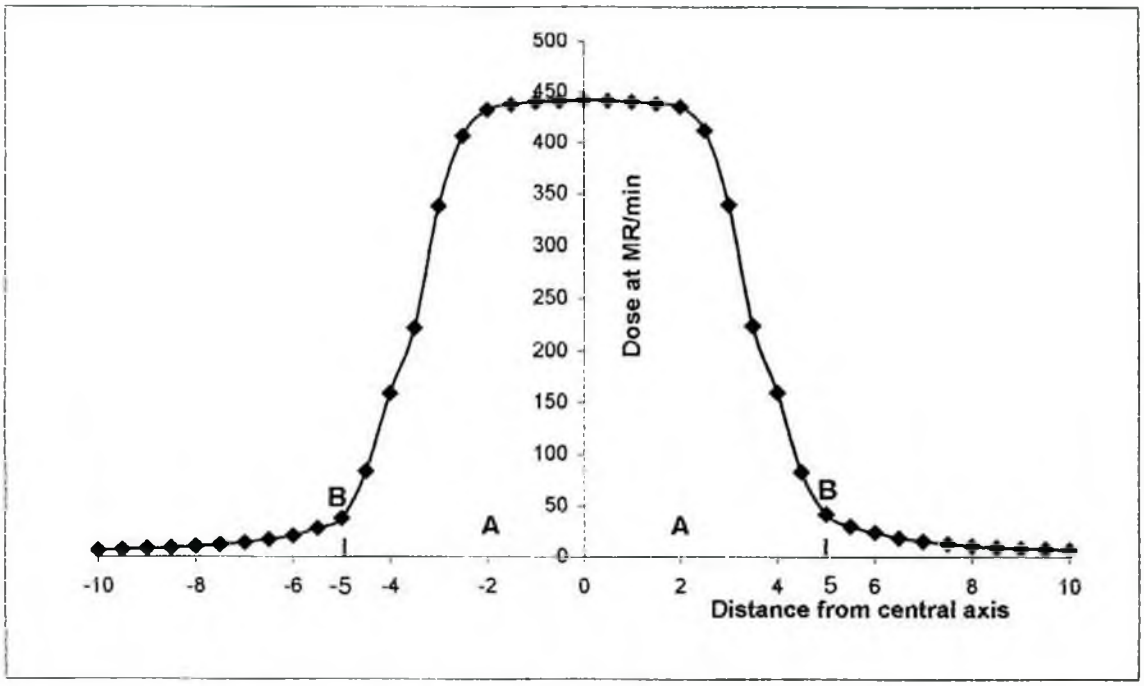

Fig 6.2: Field size 7cm×7cm
Distance vs open field scanning

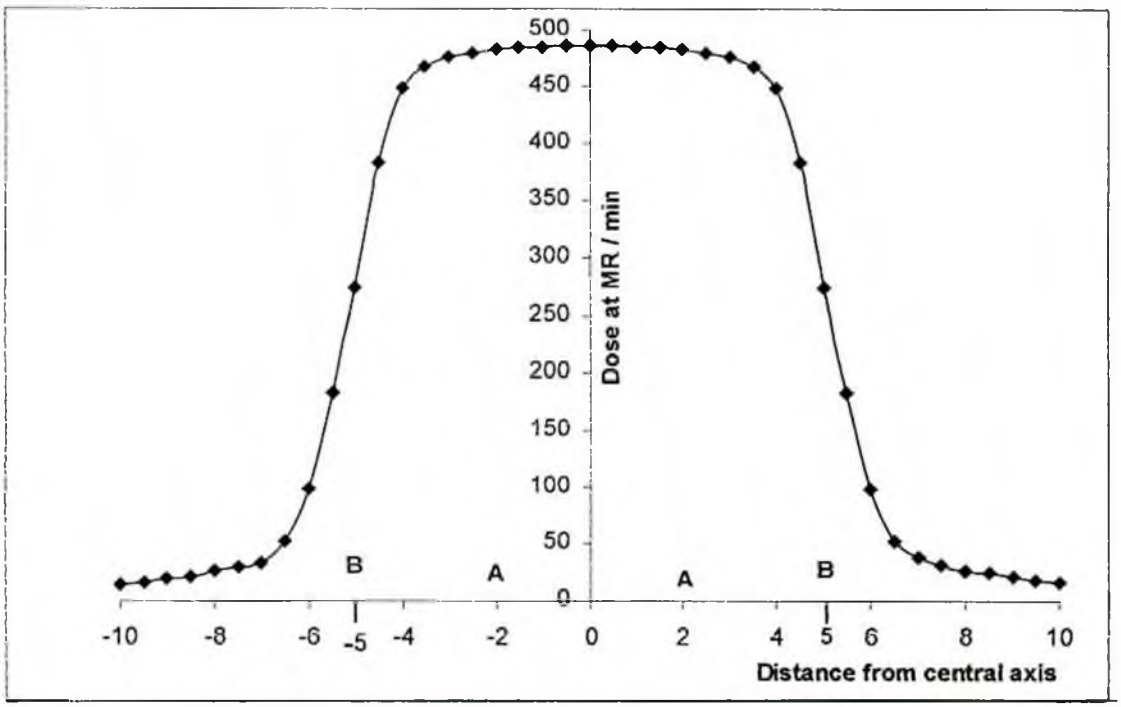

Fig 6.3: Field size 10cm×10cm
Distance vs open field scanning

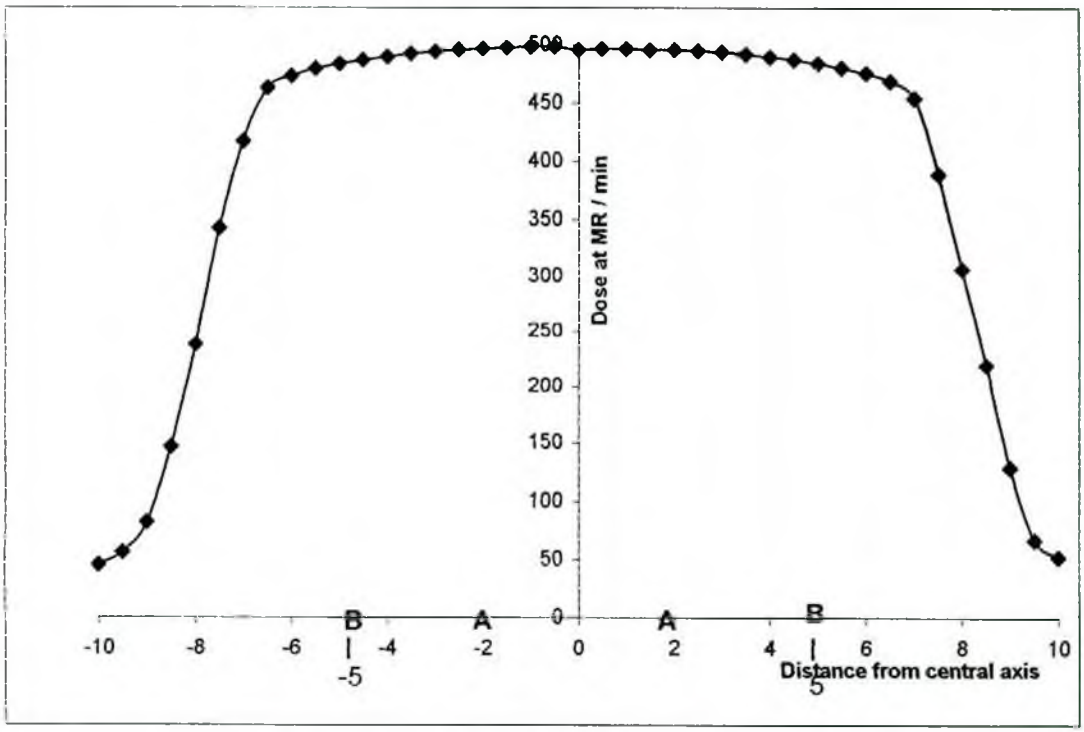

Fig 6.4: Field size 15cm×15cm
Distance vs open field scanning

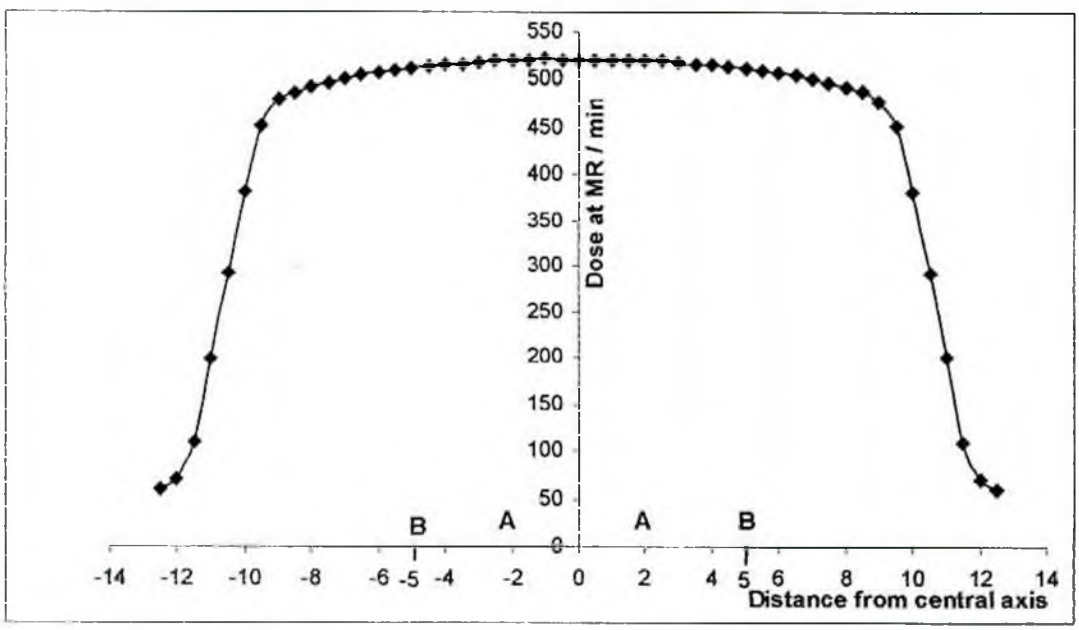

Fig 6.5: Field size 20cm×20cm
Distance vs open field scanning

The dose distribution for the field size of 10cm×10cm, 15cm×15cm, 20cm×20cm and 25cm×25cm for the case of block field are shown in Fig. 6.6 to 6.9. It is clear from the graphs that the maximum doses at central axis are 23.14, 49.29, 62.28 and 73.32 for the field sizes of 10cm×10cm, 15cm×15cm 20cm×20cm and 25cm×25cm respectively. The doses at A point with respect to the central axis dose, was found 1.13, 1.07, 1.19 and 1.10 times respectively (Fig. 6.1 to 6.5). It is clear that there is practically no dose variation from central axis to A point. The shape of the graph shows that symmetry against the central axis is very good.

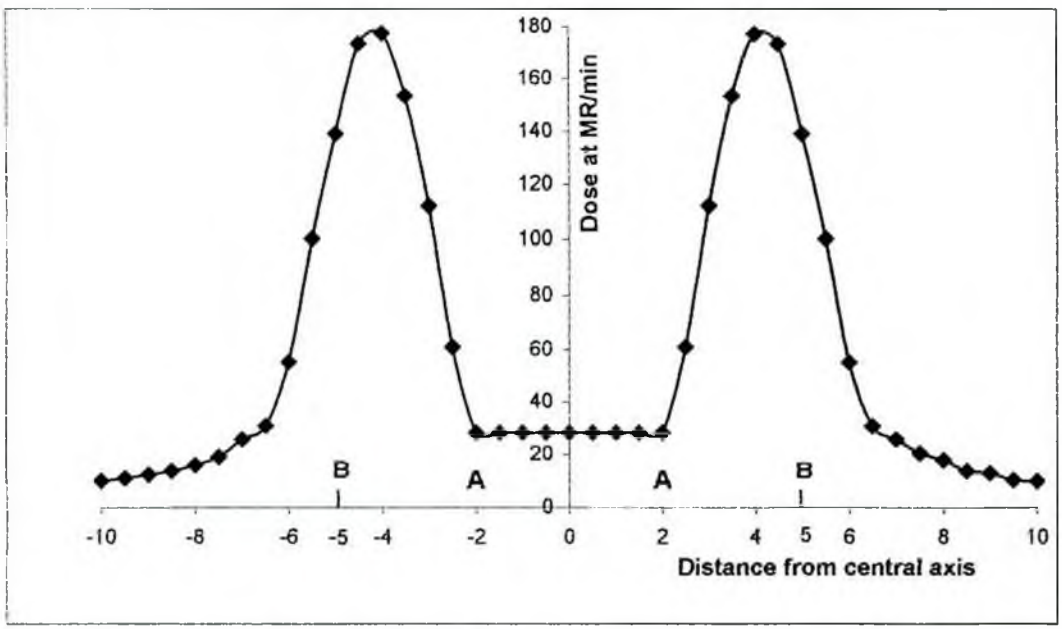

Fig 6.6: Field size 10cm×10cm
Distance vs block field scanning

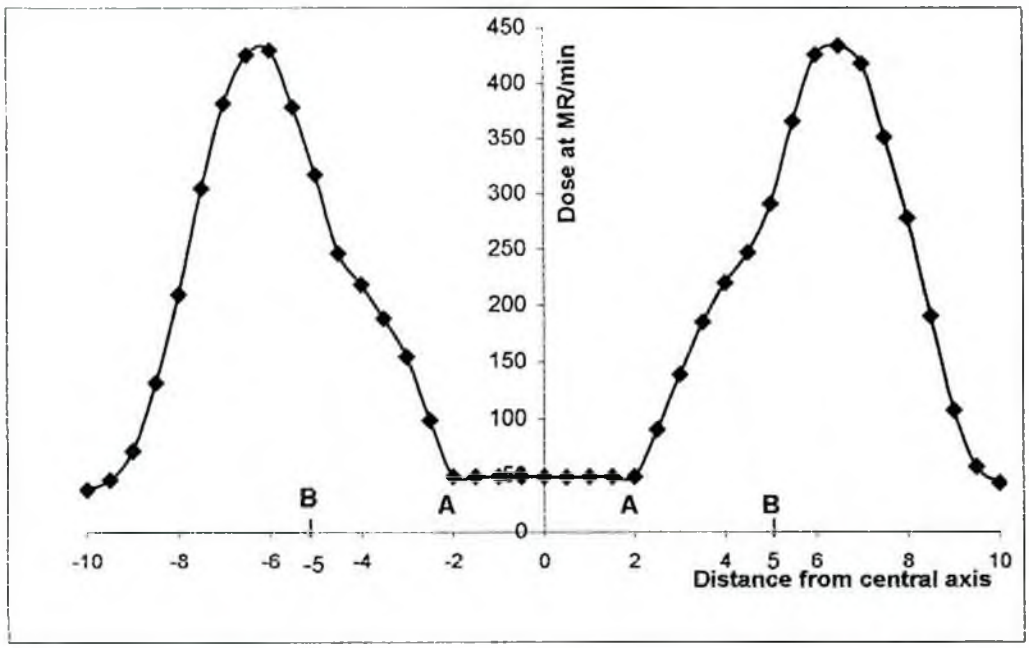

Fig 6.7: Field size 15cm×15cm
Distance vs block field scanning

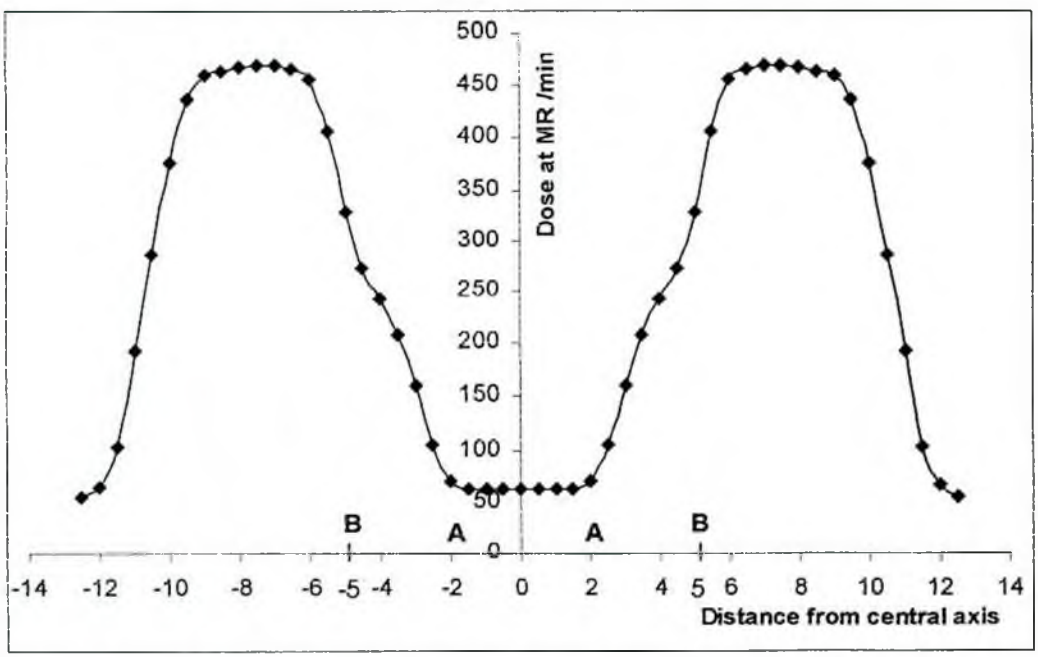

Fig 6.8: Field size 20cm×20cm
Distance vs block field scanning

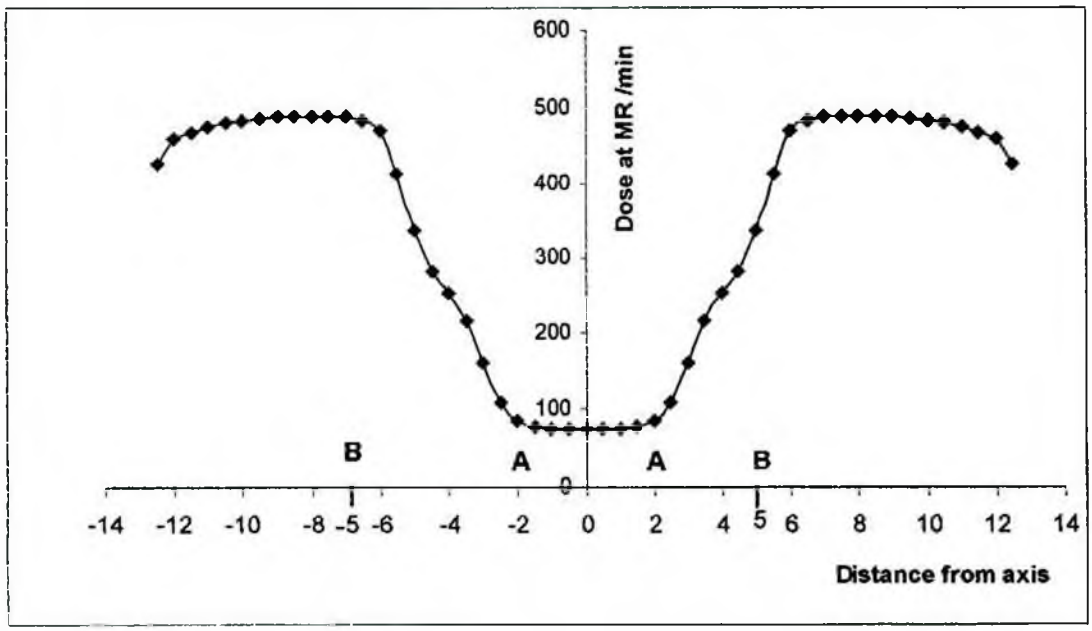

Fig 6.9: Field size 25cm×25cm
Distance vs block field scanning

The dose distribution of open field and block field for the field size of 10cm×10cm, 15cm×15cm and 20cm×20cm and the attenuation of respectively fields are shown in Fig. 6.10 to 6.12. It is clear from the graphs that the maximum attenuation at central axis is 462.76, 446.71 and 458.92 for the field sizes of 10cm×10cm, 15cm×15cm and 20cm×20cm respectively. It is clear that maximum attenuation is shown in the field size of 10×10. The shape of the graph shows that symmetry against the central axis is very good.

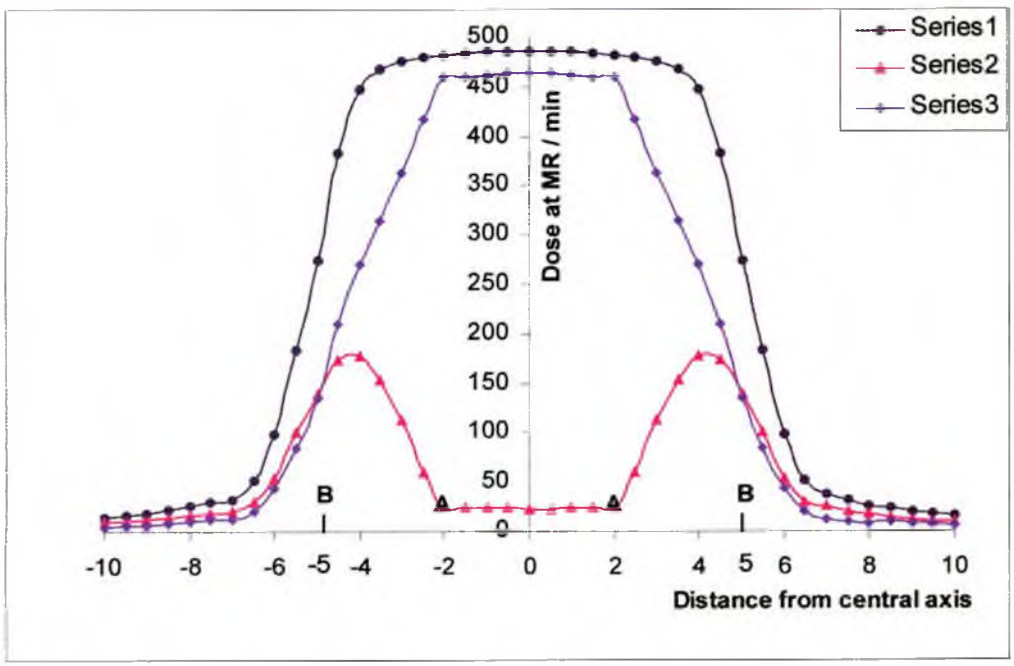

Fig 6.10 Field size 10cm×10cm
Series 1: Distance vs open field exposure
Series 2: Distance vs block field exposure
Series 3: Distance vs attenuation

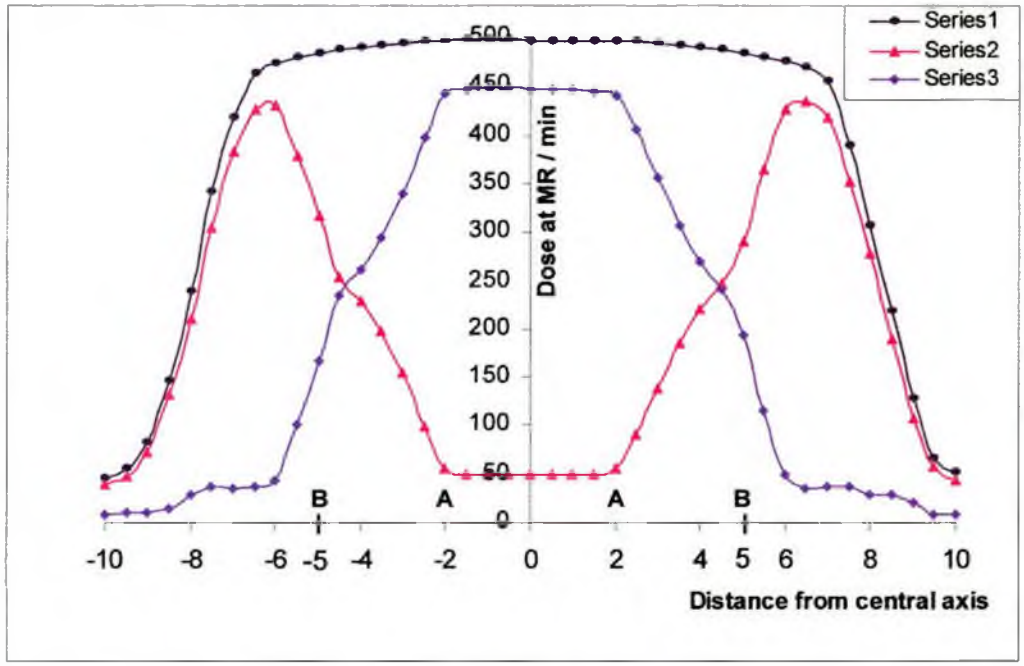

Fig 6.11 15cm×15cm attenuation
Series 1: Distance vs open field exposure
Series 2: Distance vs block field exposure
Series 3: Distance vs attenuation

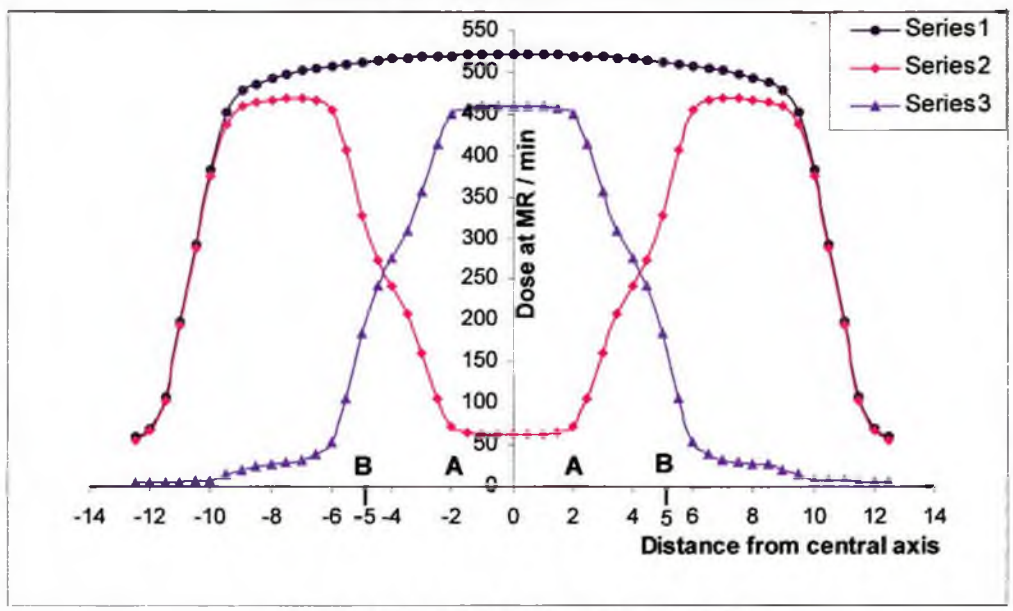

Fig 6.12 Field size 20cm×20cm
Series 1: Distance vs open field exposure
Series 2: Distance vs block field exposure
Series 3: Distance vs attenuation

The open field ratio (A point with scan) vs scan and block field ratio (A point with scan) vs scan are shown in figure 6.13 to 6.15 for the field size of 10cm×10cm, 15cm×15cm and 20cm×20cm. The open field ratio graph shows that the dose is uniform nearly up to the edge of the field for the field size of 10cm×10cm and uniformity increases as the field size increasing but the block field ratio graph shows up to point A (2 cm from central axis) the dose is uniform for every respective field. So it is clear from the graphs that from A point to A point (the area of 10×4 cm) the dose should keep uniform by using alloy block. The shape of the graph shows that symmetry against the central axis is very good.

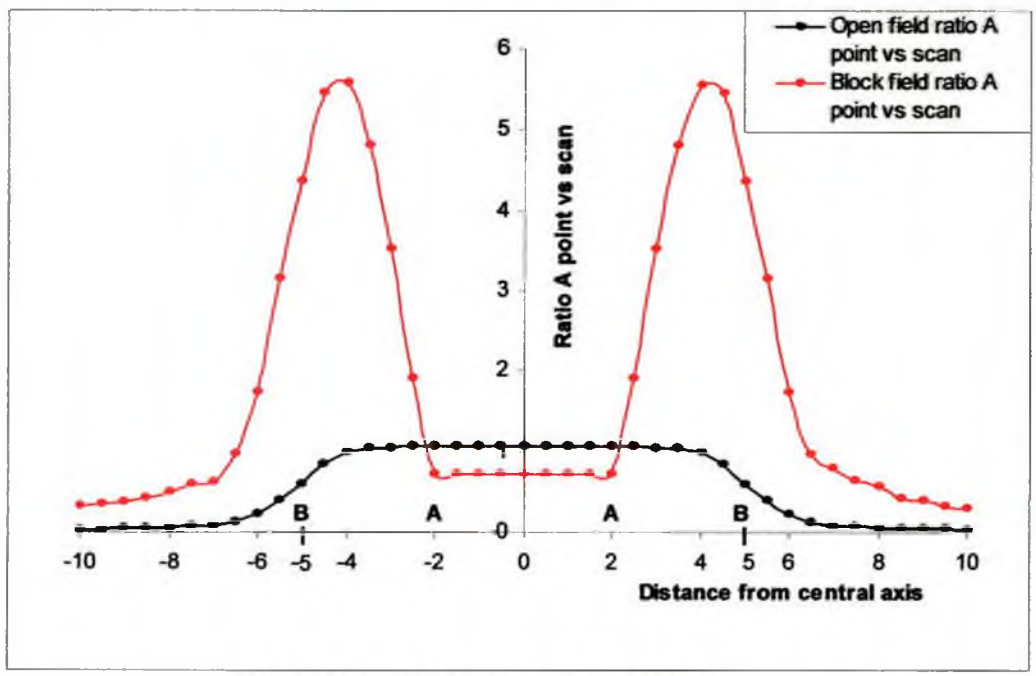

Fig 6.13: Field size 10cm×10cm

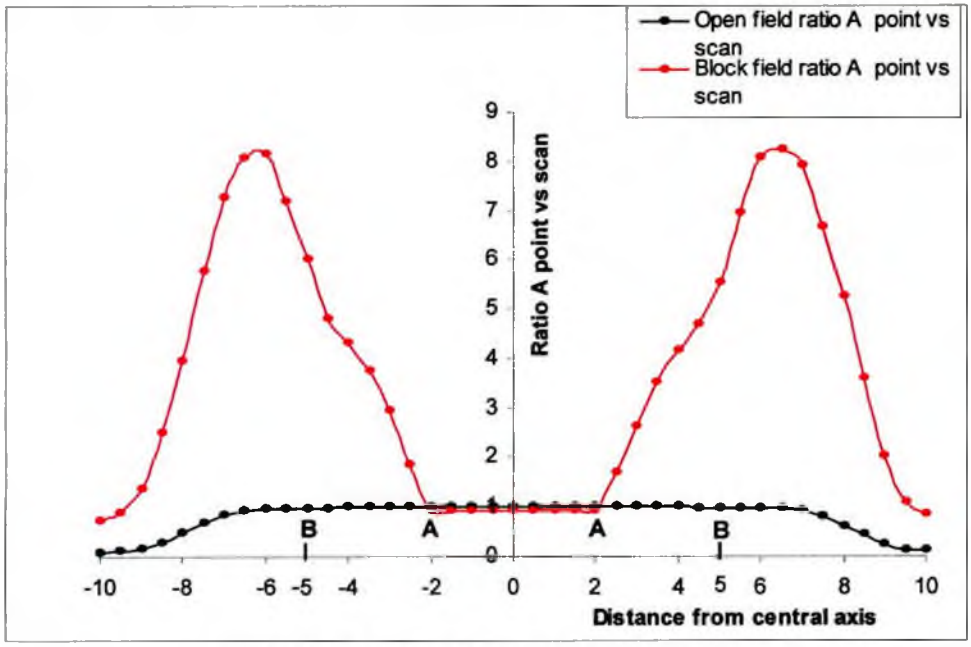

Fig 6.14: Field size 15cm×15cm

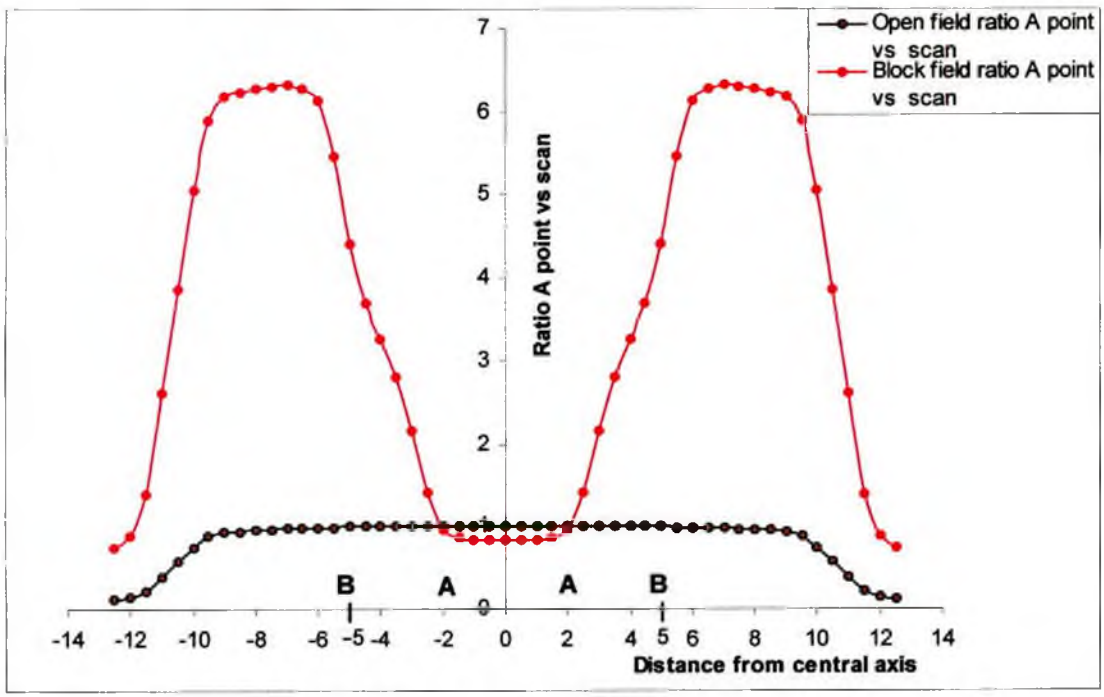

Fig 6.15: Field size 20cm×20cm

The dose distribution of open field and block field for the field size of 10cm×10cm, 15cm×15cm and 20cm×20cm and the attenuation percentage of respectively fields are shown in Fig. 6.16 to 6.18. It is clear from the graphs that the maximum attenuation from central axis to A point are nearly 96%, 90% and 88% for field sizes of 10cm×10cm, 15cm×15cm and 20cm×20cm respectively by using WMLB.

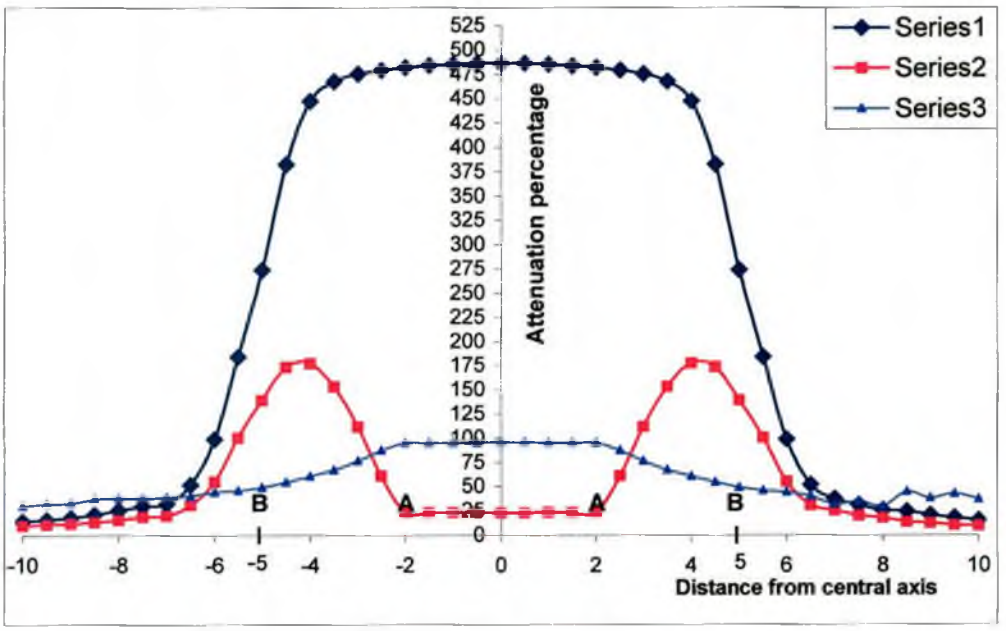

Fig 6.16: Field size of 10cm×10cm;
Series 1: Distance vs open field scanning
Series 2: Distance vs block field scanning
Series 3: Distance vs attenuation percentage

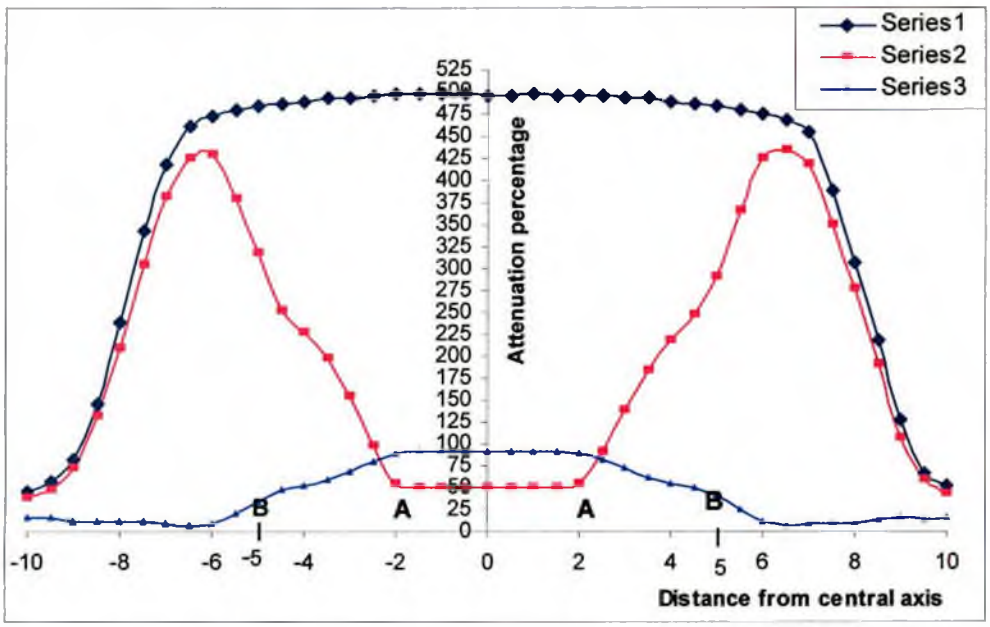

Fig 6.17: Field size of 15cm×15cm
Series 1: Distance vs open field scanning
Series 1: Distance vs block field scanning
Series 1: Distance vs attenuation percentage

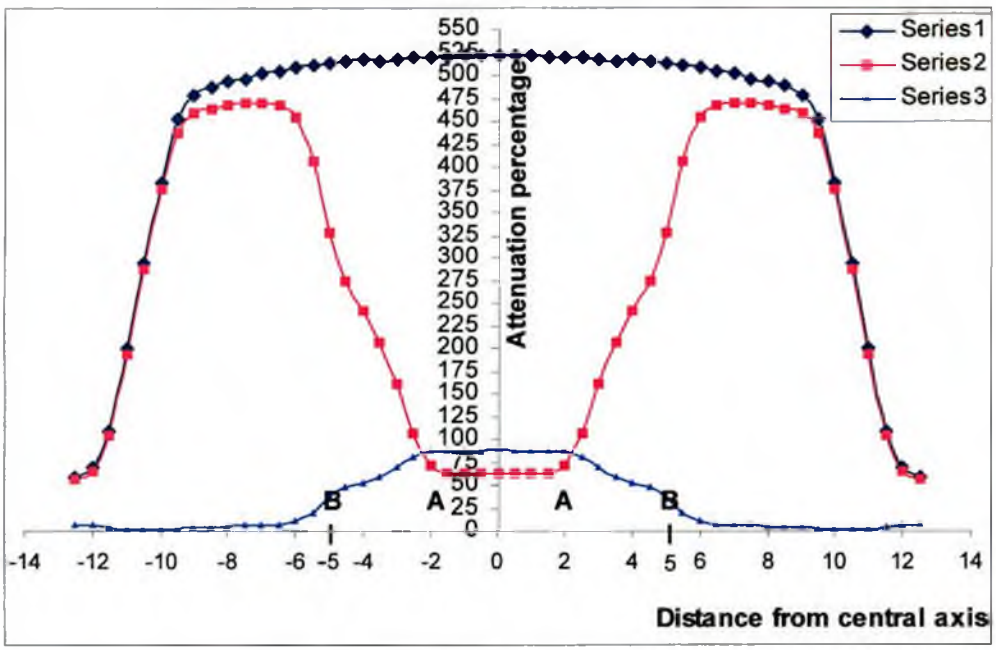

Fig 6.18: Field size of 15cm×15cm
Series 1: Distance vs open field scanning
Series 1: Distance vs block field scanning
Series 1: Distance vs attenuation percentage

Discussions:

The maximum attenuation at the center is found in the case of field size of 10cm×10cm. Here, the scattered dose is found to be minimum. The 10cm×10cm field is found to be optimum as the scattered dose is found to be minimum. From the central axis up to point A the attenuation is found to be approximately 96%(appendix table 10). The 100% attenuation is not possible practically because of the scattered irradiation. The study of the dose distribution characteristics of the fabricated WMLB shows that appropriate dose at the target volume and minimum dose at surrounding is achieved.

Conclusion:

The dose distribution curves shows that 96% attenuation is possible with the fabricated Wedge Shape Mid-Line Block. The WMLB can be used for the radiotherapy treatment of the cervix cancer for (Bangladeshi) female patients. Further improvement on attenuation may be achieved but it needs further study. However, the 100% attenuation from the central axis to A point may not be achieved due to the scattering problem.

References

References

1. 8th International Brachytherapy Conference Nice, France (Paris) 25-28November 1995.

2. FM Khan, The physics of radiotherapy, 2nd edition, Williams & Wilkins publishers, USA, 1987 p 461-62.

3. Cunningham DE, Stryker JA, Velkley DE and Chung CK , Johns HE, Gupta SK, An examination of the definition and the magnitude of backscatter factor for cobalt-60 gamma radiation, Br. J. Radiol. 38:637, 1967.

4. Alecu R Alecu M Prasad SC, "Relation between tolerance dose and treatment field size in radiotherapy", Med Phys 1978 Sep-Oct 5(5):430-3.

5. Mohan R,During IY, Toraskar J, Chui C, Anderson LL and Nori D Chadha M, Nori D, Hilaris, Wong G,et al. Stage II Carcinoma of cervix Managed With Radiation therapy: An analysis of Prognostic factors. Endocurietherapy / Hyperthermi Oncology 1988; 4: 219-28

6. Weeks KJ, Constntinou C, Attix FH, Paliwal BR, "A solid water phantom material for radiotherapy x-ray and gamma ray beam calibrations", Med Phy 1982 May-June 9(3):436-41.

7. Muench PJ and Nath R Fletcher, G.H. Saquamous cell carcinoma of uterine cervix. Text book of Radiotherapy (3rd Edition) pp. 720-733, 1980.

8. Palta JR, Meyer JA and Hogstrom KR Boag JW, Ionization measurements at very high intensities. I. pulsed radiation beams, Br. J. Radiol. 23:601, 1950.

9. Krithivas G. and Rao SN Brahme A., Dosimetric precision requirements in radiotherapy, Acta Radio. Oncol. 23:379,1984.

10. H.Stieve, Der Halsteil menschlichen Gebarmutter, sein Bau und seine Aufgaben wahrend der Schwangerschaft, der Geburt und des wochen beltes, Akadem. Verlags-gesellschaft, Leipzig. 1927.

11. O. Frankl J. Obstet. Gynaec. Br. Commonw. 40, 1933.

12. Grays Anatomy Volume 8.

13. Pierquin B, Wilson JF, Chassagned, eds. Modern Brachytherapy. New York: Masson, 1987.

14. Fletcher GH. Squamous cell carcinoma of the uterine cervix. In: Fletcher GH, ed. Textbook of Radiotherapy. 3rd ed. Philadelphia:lea & Febiger, 1980:720.

15. Schwaz G. An evaluation of the Manchester system of treatment of carcinoma of the cervix. Am J Roentgenol 1969:105:579.

16. A.M. Paterson, J. Anat.47,1912.

17. D.Denny Brown and E.G.Robertson, *Brain,* 58,1935.

18. FM Khan, The physics of radiotherapy, 2nd edition, Williams & Wilkins publishers, USA, 1987 p 51-68.

19. FM Khan, The physics of radiotherapy, 2nd edition, Williams & Wilkins publishers, USA, 1987 p 62-64.

20. FM Khan, The physics of radiotherapy, 2nd edition, Williams & Wilkins publishers, USA, 1987 p 78-81.

21. Mohan R. Secondary field shaping asymmetric collimators and multileaf collimators. American Institute of Physics, 1992:307.

22. Comite Consultatif Pour les Etalons De Measure Des Rayonnements Ionisants (section-1), Correction d'humidity, Recommendation CCEMRI(1) R(1), Bureau International des Poids et Measures, Severs, 1977.

23. Holt JG, Laughlim JS, Moroney JP, Extension of concept of tissue air ratios (TAR) to high energy X-ray beams, Raiol 96:437, 1970.

24. Khan FM, Sewchand W, Lee J, Williamson JF, Revision of tissue maximum ratio and scatter maximum ratio concepts for cobalt-60 and higher energy X-ray beams, Med. Phys. 7:230, 1980.

25. Dobbs J, Barrelt A, Ash D, Practical radiotherapy planning, 2nd edition, British Library cataloging in publication data.

26. Tannous NB, Gagnon WF, Almond PR, "Buildup region and skin-dose measurements for the Therac 6 Linear Accelerator for radiation therapy" Med. Phys. 1981 May-June 8(3):378-81.

27. Boag JW, Currant J, Current collection and ionic recombination in small cylindrical ionization chambers exposed to pulsed radiation, Br. J. Radiol. 53:471, 1980.

28. Almond PR, Svensson H, Ionization chamber dosimetry for photon and electron beams. Theoretical considerations, Acta Radiol., Ther. Phys. Boil. 16:177. 1977.

29. Hendee WR, Medical Radiation Physics, 2nd edition, yearbook medical publishers inc., Chicago, London, 1979.

30. Ter-Pogossian M, The physical aspects of diagnostic radiology, Harper & Raw, New York, 1967.

31. Meredith W, Massey J, Fundamental physics of radiology, Williams & Wilkins Co. Baltimore, 1968.

32. Purdy JA, "Relationship between tissue phantom ratio and percentage depth dose" Med Phys 1977 Jan-Feb 4(1):66-7.

33. Powers WE, Kinzie JJ, Demidecki AJ, Bradfield JS, Feldman A. A new system of field shaping for external beam radiation therapy. Radiology 1973; 108:407.

34. Powers WE, Kinzie JJ, Demidecki AJ, Bradfield JS, Feldman A. A new system of field shaping for external beam radiation therapy. Radiology 1973; 108:407.

35. Brahme FM, Gerbi BJ, Deibel Fc. Dosimetry of asymmetric x-ray collimators. Med Phys 1986; 13:936.

36. Mohan R. Secondary field shaping asymmetric collimators and multileaf collimators. American Institute of Physics, 1992:307.

37. Aron BS, Scapicchio M. Design of universal wedge filter system for a cobalt 60 unites. Am J Roentgenol 1966;96:70.

38. Cohen M, Martin SM, Eds. Atlas of radiation dose distributions. Vol. II of Multiple field isodose charts. Vienna; International Atomic Energy Agency, 1966.

39. Richard PZ, Lawrence RC, William JH. Cancer Management: A Multidisciplinary Approach. 6th edition, page 392.

40. Jane Dobbs, Ann Barrett, Dan Ash. Practical radiotherapy planning. 3rd edition. 1999; page 252, 280,310.

41. Brahme FM, Gerbi BJ, Deibel Fc. Dosimetry of asymmetric x-ray collimators. Med Physics 1986; 13:936.

42. Kase KR, Alder GJ, Bjarngar BE. Comparison of electron beam dose measurements in water and polystyrene using various dosimeters, Med. Phys., 9:13-9, 1982.

43. Mattsson LO, Nahum AE, "Concerning comparisons of electron beam dose measurements in water and polystyrene", Med Phys 1984 Jan-Feb 11(1):85-7.

44. Baird LC, White DR, " A survey of tissue substitutes and phantoms in 98 U.S. medical centers", Med Phys 1982 May-June 9(3):434-5.

45. P.Francois, C. Beurtheret, and A Dutreix, Calculation of the dose delivered to organs outside the radiation beams, Med. Phy. 1988 15(6):879-83.

46. P.H.van der Giessen and CW Hurkmans, Calculation and measurements of the dose to points outside the primary beam for ^{60}Co gamma radiation, International J. Radiation Oncol. Biol.Phys. 27:717-24, 1993.

47. D.Greene, P.G.G. Karup, C. Sims and R.J. Taylor, Dose levels outside radiotherapy beam, Br. J. Radiol. 58, 543, 1985.

48. P.H. van der Giessen, Collimator related radiation dose for different cobalt machines and linear accelerator, International J. of Radiation Oncology Biology Physics 35, 399-405,
1966.

49. T.F. Sandeman, The effects x-ray irradiation on male human fertility, Br. J. Radiol. 39,901, 1966.

50. Hossain T. obayedullah M, Miah NI Specific aspect of cancer prevention and control, Bang. Cancer Reports, 14:24, 1992.

51. Hospital Physicists Association, Central axis depth dose data for use in radiotherapy, Br. J. Radiol. (suppl 11), 1978.

52. Johns HE, Physical aspects of rotation therapy, Am. J. Roentgenol, 79:373, 1958.

53. Gupta SK, Cunningham JR, Measurement of tissue air ratios and scatter functions for large field sizes for cobalt–60 gamma radiation, Br. J. Radiol. 39:7, 1933.

54. Wonf JW, Henkelmen RM, Andrew JW, Dyk JV, Jones HE, "Effect of small inhomogeneities on dose in a cobalt-60 Beam", Med. Phys. 1981 Nov-Dec 8(6):783-91.

55. Ahuja SD, Stroup SL, Bolin MG, Gibbs SJ, "Physical approach to depth dose distributions in a water phantom irradiated by a teleisotope phantom beam", Med phys 1980 Mar-Apr 7(2):120-6.

56. Freim JO, Feldman A, "Cobalt-60 dose calibration: A comparison of method", Mwd phys 1979 Nov-Dec 6(6):530-5.

57. P.H. van der Giessen, Dose outside the irradiated volume in radiotherapy, Dr. Bernard Verbeeten Institute, Tilburg, Netherlands, 1997.

58. Cember H, Introduction to health physics, 2nd edition, McGraw-Hill, Inc. 1992.

59. Martin A and Harbison SA, An introduction to radiation protection, 2nd edition, Chapman and Hall Ltd., 1982.

60. ICRU, publication 60, Vol. 21, No. 1-3, 1990, Recommendations of the international commission on radiological protection, Pergamon Press, Oxford UK, 1991.

61. UNSCEAR, report to the general assembly, genetic and somatic effects of radiation, New York, USA, 1997.

62. Dekaban AS, Abnormalities in children exposed to X-radiation during various stage of gestation; tentative timetable of radiation injury to human fetus, part-2, J. Nucl. Med. 9:471-477, 1986.

63. Spiers F, Dosage in bone, in clinical dosimetry, ICRU, report 10d, national bureau of standards handbook 87, 1963.

64. Almond PR, Svensson H, Ionization chamber dosimetry for photon and electron beams. Theoretical considerations, Acta Radiol., Ther. Phys. Boil. 16:177. 1977.

65. Horton JL, Handbook of radiation therapy physics, Prentice hall inc, Englewood cliffs, n.j., USA, 1987.

66. DR White, Tissue substitutes in experimental radiation physics, Med. Phys. 5(6):467-79, 1978.

67. Satherberg A, Karlsson M, Theoretical and experimental determination of phantom scatter factors for photon fields with different radial energy variation, Phys. Med. Biol. Dec 41(12):2687-94, 1996.

68. Pourquir H. Dabois, J.B. and Delard R: Cancer of the uterine cervix: Dosimetric guideline for prevention of late rectal and recto sigmoid complications at a result of there poutictreatment Int. journal of radiation Oncology, Biology and Physics, Vol. 8, 1987- 1995, 1982.

69. Perez, C.A. Camal. H. M. Kuske, R.R. Kao, M.S. Galakatos, A. Hederman, M.A. and Powers, W.E.Radio alone in treatment of cercinoma of Uterine cervix: A 20 years experience. Gynecological Oncology 23, 127-140; 1986.

70. Perez, C.A. Camal H.M. Kao, M.S. and Askin, F. Randomised study of preoperative radio and surgery or irradiation alone in treatment of stage 1b and 11 11a carcinoma of the uterine cervix: Preliminary Analysis of failures and complications, Cancer 45: 2759-2768, 1980.

71. Perez, C. A. Breaux, S. Bedwinek. J.M. Jones. H.M. Camal, H.M. Purdy, J.A. And Walz. B.J. Radiation therapy alone in the treatment of Carcinoma of cervix. Analysis of complications Cancer 54: 235-246, 1984.

72. Ben Sischy. The design of linear source system for integration with super voltage irradiation in the management of carcinoma of uterine cervix. Endocurietherapy / Hyperthermia, 2; 77-82,1986.

73. Johns H.E. and Cunningham J.R. Physics of Radiology (second edition), pp 138-141, Publisher Charles C. Thomas 1986.

74. Bentel Gunilla, C. Nelson, Charles, E., Treatment planning and dose calculation in radiation oncology. pp 1-3, 34-38,119-138, Publisher; Pergamon press Inc. 1985

75. ICRU ; Dose and volume specifications for reporting intracavitary therapy in gynecology. ICRU publications Washington D.C. 1985.

76. International Commission on Radiation Units and Measurements. Determination of absorbed dose in a patient irradiated by beams of X-ray or gamma rays in radiotherap procedure, ICRU, Rep. 24, ICRU publications, Bethesade, MD, 1976.

77. Technical reports series no 277, Absorbed dose determination in photon and electrons beams, IAEA, Vienna, 1987.

Appendix

Appendix

Table 1:

Specifications of Universal Dosimeter UNIDOS[40]

	Digital resolution	Maximum input rating
Charge mode	10^{14} C	2.2×10^{8} C
Current mode	10^{-15} A	10^{-6}A
Integrated current mode	10^{-14}C	6.5×10^{-2} C
Leakage current	$\leq 10^{-15}$A	
Amplifier zeroing	automatically within 75 second according to IEC	
Linearity	$\leq \pm 0.5$ according to IEC	
Long-term stability typically	±0.05% per year	
Measuring quantities	absorbed dose to water, air kerma, absorbed dose to air, photon equivalent dose, exposure	
Chamber voltage	(0.....400)V, adjustable in 50-Volt increments, polarity selectable	
Temperature range	(10.....40)°C/(50.....104)°F	
Relative humidity	(10....75)% relative humidity, 20 g/m³ max	
Signal input connector	PTW type M. INC or BNT (BNC with banana , Plug on request	
Power supply	line power 115/230 V [50.....6] Hz, or independent of power line, from rechargeable NiCd batteries (operating time: 7 to 9 hours)	
Case dimensions	[H × W × D] 152 × 257 × 262 mm³ (6×10.1×10.3 in)	
Weight	6.4 kg (44.11 lb)	

Table 2:

Technical specification of ionization chamber type 23323[40]

Volume	:	0.10 cm^3
Response	:	3.8×10^{-9} C/Gy
Leakage	:	$\pm4\times10^{-15}$ A
Polarizing Voltage	:	Maximum 500V
Cable Leakage	:	1×10^{-12} C/(Gy.cm)
Wall Material	:	Rubber
		+PMMA $(C_5H_8O_2)_n$
		+Graphite (C)
Wall Density	:	1.20 g/cm^3 (Rubber)
	:	1.19 g/cm^3 (PMMA)
	:	0.82 g/cm^3 (C)
Wall Thickness	:	0.95 mm Rubber
		+0.613 mm PMMA
		+0.125 mm C
Area Density	:	197 mg/cm^2
Electrode	:	Aluminum, Graphite coated;
		0.8 mm φ; 10 mm long
Range of Temperature	:	$+10^0$C to $+40^0$C
Range of Relative Humidity	:	10% to 80% (<20 g/m^3)
Ion Collection Time	:	300V :0.4 ms
		400V :0.03 ms
		500V :0.02 ms

Table 3: Open field scanning 5cm×5cm field size

Distance from central axis in cm	Field size 5*5	Dose at A point	Ratio A point vs scan	Dose at B point	Ratio B point vs scan	Deviation A point vs scan	Deviation B point vs scan
-10	3.27	233.9	71.529	11.55	3.532	230.63	8.28
-9.5	3.6	233.9	64.972	11.55	3.208	230.3	7.95
-9	3.96	233.9	59.066	11.55	2.917	229.94	7.59
-8.5	4.32	233.9	54.144	11.55	2.674	229.58	7.23
-8	4.95	233.9	47.253	11.55	2.333	228.95	6.6
-7.5	5.58	233.9	41.918	11.55	2.070	228.32	5.97
-7	6.48	233.9	36.096	11.55	1.782	227.42	5.07
-6.5	7.71	233.9	30.337	11.55	1.498	226.19	3.84
-6	8.85	233.9	26.429	11.55	1.305	225.05	2.7
-5.5	10.95	233.9	21.361	11.55	1.055	222.95	0.6
-5	14.22	233.9	16.449	11.55	0.812	219.68	-2.67
-4.5	19.35	233.9	12.088	11.55	0.597	214.55	-7.8
-4	28.65	233.9	8.164	11.55	0.403	205.25	-17.1
-3.5	63.54	233.9	3.681	11.55	0.182	170.36	-51.99
-3	133.1	233.9	1.757	11.55	0.087	100.8	-121.55
-2.5	215.5	233.9	1.085	11.55	0.054	18.4	-203.95
-2	393.4	233.9	0.595	11.55	0.029	-159.5	-381.85
-1.5	411.3	233.9	0.569	11.55	0.028	-177.4	-399.75
-1	420	233.9	0.557	11.55	0.028	-186.1	-408.45
-0.5	420.1	233.9	0.557	11.55	0.027	-186.2	-408.55
0	420.6	252.1	0.599	11.55	0.027	-168.5	-409.05
0.5	419.9	252.1	0.600	11.55	0.028	-167.8	-408.35
1	418.4	252.1	0.603	11.55	0.028	-166.3	-406.85
1.5	411	252.1	0.613	11.55	0.028	-158.9	-399.45
2	396.2	252.1	0.636	11.55	0.029	-144.1	-384.65
2.5	213.7	252.1	1.180	11.55	0.054	38.4	-202.15
3	131.5	252.1	1.917	11.55	0.088	120.6	-119.95
3.5	65.4	252.1	3.855	11.55	0.177	186.7	-53.85
4	42.06	252.1	5.994	11.55	0.275	210.04	-30.51
4.5	23.79	252.1	10.597	11.55	0.485	228.31	-12.24
5	16.38	252.1	15.391	11.55	0.705	235.72	-4.83
5.5	12.66	252.1	19.913	11.55	0.912	239.44	-1.11
6	9.96	252.1	25.311	11.55	1.160	242.14	1.59
6.5	8.28	252.1	30.447	11.55	1.395	243.82	3.27
7	6.84	252.1	36.857	11.55	1.689	245.26	4.71
7.5	5.94	252.1	42.441	11.55	1.944	246.16	5.61
8	5.22	252.1	48.295	11.55	2.213	246.88	6.33
8.5	4.5	252.1	56.022	11.55	2.567	247.6	7.05
9	3.99	252.1	63.183	11.55	2.895	248.11	7.56
9.5	3.6	252.1	70.028	11.55	3.208	248.5	7.95
10	3.27	252.1	77.095	11.55	3.532	248.83	8.28

Table 4: Open field scanning 7cm×7cm field size

Distance from central axis in cm	Dose in mR/min	Dose at A point	Ratio A point vs scan	Dose at B point	Ratio B point vs scan	Deviation A point vs scan	Deviation B point vs scan
-10	6.15	405.8	65.984	45.06	7.327	399.65	38.91
-9.5	7.11	405.8	57.075	45.06	6.338	398.69	37.95
-9	8.01	405.8	50.662	45.06	5.625	397.79	37.05
-8.5	8.82	405.8	46.009	45.06	5.109	396.98	36.24
-8	10.23	405.8	39.668	45.06	4.405	395.57	34.83
-7.5	11.67	405.8	34.773	45.06	3.861	394.13	33.39
-7	13.98	405.8	29.027	45.06	3.223	391.82	31.08
-6.5	16.98	405.8	23.899	45.06	2.654	388.82	28.08
-6	20.7	405.8	19.604	45.06	2.177	385.1	24.36
-5.5	28.44	405.8	14.269	45.06	1.584	377.36	16.62
-5	38.22	405.8	10.617	45.06	1.179	367.58	6.84
-4.5	83.65	405.8	4.851	45.06	0.539	322.15	-38.59
-4	158.8	405.8	2.555	45.06	0.284	247	-113.74
-3.5	221.8	405.8	1.830	45.06	0.203	184	-176.74
-3	337.7	405.8	1.202	45.06	0.133	68.1	-292.64
-2.5	406.3	405.8	0.999	45.06	0.111	-0.5	-361.24
-2	432.1	405.8	0.939	45.06	0.104	-26.3	-387.04
-1.5	437.2	405.8	0.928	45.06	0.103	-31.4	-392.14
-1	439.6	405.8	0.923	45.06	0.103	-33.8	-394.54
-0.5	441	405.8	0.920	45.06	0.102	-35.2	-395.94
0	441.6	409.9	0.928	45.06	0.102	-31.7	-396.54
0.5	441.5	409.9	0.928	45.06	0.102	-31.6	-396.44
1	440.1	409.9	0.931	45.06	0.102	-30.2	-395.04
1.5	438.1	409.9	0.936	45.06	0.103	-28.2	-393.04
2	435.1	409.9	0.942	45.06	0.104	-25.2	-390.04
2.5	426.1	409.9	0.962	45.06	0.106	-16.2	-381.04
3	387.1	409.9	1.059	45.06	0.116	22.8	-342.04
3.5	223.9	409.9	1.831	45.06	0.201	186	-178.84
4	159.8	409.9	2.565	45.06	0.282	250.1	-114.74
4.5	82.9	409.9	4.945	45.06	0.544	327	-37.84
5	50.31	409.9	8.147	45.06	0.896	359.59	-5.25
5.5	30.6	409.9	13.395	45.06	1.473	379.3	14.46
6	24.21	409.9	16.931	45.06	1.861	385.69	20.85
6.5	18.69	409.9	21.932	45.06	2.411	391.21	26.37
7	15.54	409.9	26.377	45.06	2.900	394.36	29.52
7.5	12.96	409.9	31.628	45.06	3.477	396.94	32.1
8	10.83	409.9	37.849	45.06	4.161	399.07	34.23
8.5	9.39	409.9	43.653	45.06	4.799	400.51	35.67
9	8.31	409.9	49.326	45.06	5.422	401.59	36.75
9.5	7.47	409.9	54.873	45.06	6.032	402.43	37.59
10	6.66	409.9	61.547	45.06	6.766	403.24	38.4

Table 5: Open field scanning 10cm×10cm field size

Distance from central axis in cm	Dose in mR/min	Dose at A point	Ratio A point vs scan	Dose at B point	Ratio B point vs scan	Deviation A point vs scan	Deviation B point vs scan
-10	14.16	453.5	32.027	316.9	22.380	439.34	302.7
-9.5	16.08	453.5	28.203	316.9	19.708	437.42	300.8
-9	18.18	453.5	24.945	316.9	17.431	435.32	298.7
-8.5	21.54	453.5	21.054	316.9	14.712	431.96	295.4
-8	25.44	453.5	17.826	316.9	12.457	428.06	291.5
-7.5	31.2	453.5	14.535	316.9	10.157	422.3	285.7
-7	37.41	453.5	12.122	316.9	8.471	416.09	279.5
-6.5	51.99	453.5	8.723	316.9	6.095	401.51	264.9
-6	98.76	453.5	4.592	316.9	3.209	354.74	218.1
-5.5	184.1	453.5	2.463	316.9	1.721	269.4	132.8
-5	244.1	453.5	1.655	316.9	1.156	179.4	72.8
-4.5	382.4	453.5	1.186	316.9	0.829	71.1	-65.5
-4	447.5	453.5	1.013	316.9	0.708	6	-130.6
-3.5	467.9	453.5	0.969	316.9	0.677	-14.4	-151.0
-3	475.4	453.5	0.954	316.9	0.667	-21.9	-158.5
-2.5	479.3	453.5	0.946	316.9	0.661	-25.8	-162.4
-2	482.1	453.5	0.941	316.9	0.657	-28.6	-165.2
-1.5	483.8	453.5	0.937	316.9	0.655	-30.3	-166.9
-1	485.6	453.5	0.935	316.9	0.653	-31.6	-168.7
-0.5	485.4	453.5	0.933	316.9	0.652	-32.5	-168.5
0	485.9	453.5	0.933	316.9	0.702	-32.4	-169.0
0.5	485.4	453.5	0.933	316.9	0.702	-32.7	-168.5
1	485.7	453.5	0.934	316.9	0.702	-32.2	-168.8
1.5	484.6	453.5	0.936	316.9	0.704	-31.1	-167.7
2	483.4	453.5	0.938	316.9	0.706	-29.9	-166.5
2.5	480.7	453.5	0.943	316.9	0.710	-27.2	-163.8
3	477.6	453.5	0.950	316.9	0.714	-24.1	-160.7
3.5	473.6	453.5	0.958	316.9	0.720	-20.1	-156.7
4	467.4	453.5	0.970	316.9	0.730	-13.9	-150.5
4.5	391.1	453.5	1.028	316.9	0.773	12.4	-74.2
5	243.2	453.5	1.256	316.9	0.944	92.3	73.7
5.5	186.1	453.5	1.667	316.9	1.254	181.4	130.8
6	96.8	453.5	2.769	316.9	2.082	289.7	220.1
6.5	57.48	453.5	5.184	316.9	3.899	366.02	259.4
7	48.87	453.5	9.280	316.9	6.980	404.63	268.0
7.5	36.81	453.5	12.320	316.9	9.267	416.69	280.1
8	30.24	453.5	14.997	316.9	11.280	423.26	286.7
8.5	24.51	453.5	18.503	316.9	13.917	428.99	292.4
9	20.7	453.5	21.908	316.9	16.478	432.8	296.2
9.5	17.79	453.5	25.492	316.9	19.174	435.71	299.1
10	15.54	453.5	29.183	316.9	21.950	437.96	301.4

Table 6: Open field scanning 15cm×15cm field size

Distance from central axis in cm	Dose in mR/min	Dose at A point	Ratio A point vs scan	Dose at B point	Ratio B point vs scan	Deviation A point vs scan	Deviation B point vs scan
-10	45.57	493.2	10.823	480	10.533	447.63	434.43
-9.5	56.19	493.2	8.777	480	8.542	437.01	423.81
-9	81.96	493.2	6.018	480	5.857	411.24	398.04
-8.5	220.3	493.2	3.371	480	3.281	346.9	333.7
-8	237.8	493.2	2.074	480	2.019	255.4	242.2
-7.5	258.3	493.2	1.441	480	1.402	150.9	137.7
-7	417.1	493.2	1.182	480	1.151	76.1	62.9
-6.5	462.4	493.2	1.067	480	1.038	30.8	17.6
-6	472.9	493.2	1.043	480	1.015	20.3	7.1
-5.5	479.4	493.2	1.029	480	1.001	13.8	0.6
-5	483.4	493.2	1.020	480	0.993	9.8	-3.4
-4.5	487	493.2	1.013	480	0.986	6.2	-7
-4	489.6	493.2	1.007	480	0.980	3.6	-9.6
-3.5	492.3	493.2	1.002	480	0.975	0.9	-12.3
-3	494.2	493.2	0.998	480	0.971	-1	-14.2
-2.5	495.6	493.2	0.995	480	0.969	-2.4	-15.6
-2	496.7	493.2	0.993	480	0.966	-3.5	-16.7
-1.5	497.7	493.2	0.991	480	0.964	-4.5	-17.7
-1	498.4	493.2	0.990	480	0.963	-5.2	-18.4
-0.5	498.6	493.2	0.989	480	0.963	-5.4	-18.6
0	500	493.2	0.994	480	0.968	-2.8	-16
0.5	496.7	493.2	0.993	480	0.967	-3.3	-16.5
1	496.6	493.2	0.993	480	0.967	-3.4	-16.6
1.5	495.7	493.2	0.995	480	0.968	-2.5	-15.7
2	495.7	493.2	0.995	480	0.968	-2.5	-15.7
2.5	494.9	493.2	0.997	480	0.970	-1.7	-14.9
3	493.7	493.2	0.999	480	0.972	-0.5	-13.7
3.5	492.1	493.2	1.002	480	0.975	1.1	-12.1
4	489.7	493.2	1.007	480	0.980	3.5	-9.7
4.5	487.2	493.2	1.012	480	0.985	6	-7.2
5	484.2	493.2	1.019	480	0.991	9	-4.2
5.5	480.1	493.2	1.027	480	1.000	13.1	-0.1
6	475.6	493.2	1.037	480	1.009	17.6	4.4
6.5	455.6	493.2	1.052	480	1.024	24.6	11.4
7	402	493.2	1.086	480	1.057	39.2	26
7.5	260.9	493.2	1.268	480	1.234	104.3	91.1
8	236.2	493.2	1.611	480	1.568	187	173.8
8.5	218.4	493.2	2.258	480	2.198	274.8	261.6
9	128.4	493.2	3.841	480	3.738	364.8	351.6
9.5	66.69	493.2	7.395	480	7.197	426.51	413.31
10	51.84	493.2	9.514	480	9.259	441.36	428.16

Table 7: Open field scanning 20cm×20cm field size

Distance from central axis in cm	Dose in mR/min	Dose at A point	Ratio A point vs scan	Dose at B point	Ratio B point vs scan	Deviation A point vs scan	Deviation B point vs scan
-12.5	59.37	513.7	8.6525	505.8	8.5195	454.33	446.43
-12	70.14	513.7	7.3239	505.8	7.2113	443.56	435.66
-11.5	108.4	513.7	4.7389	505.8	4.6661	405.3	397.4
-11	199	513.7	2.5814	505.8	2.5417	314.7	306.8
-10.5	242.5	513.7	1.7562	505.8	1.7292	221.2	213.3
-10	282.6	513.7	1.3448	505.8	1.3241	131.7	123.8
-9.5	391.7	513.7	1.1373	505.8	1.1198	62	54.1
-9	478.6	513.7	1.0733	505.8	1.0568	35.1	27.2
-8.5	486.3	513.7	1.0563	505.8	1.0401	27.4	19.5
-8	492.7	513.7	1.0426	505.8	1.0266	21	13.1
-7.5	496.7	513.7	1.0342	505.8	1.0183	17	9.1
-7	501.3	513.7	1.0247	505.8	1.0090	12.4	4.5
-6.5	504.7	513.7	1.0178	505.8	1.0022	9	1.1
-6	507.8	513.7	1.0116	505.8	0.9961	5.9	-2
-5.5	510.3	513.7	1.0067	505.8	0.9912	3.4	-4.5
-5	512.4	513.7	1.0025	505.8	0.9871	1.3	-6.6
-4.5	514.4	513.7	0.9986	505.8	0.9833	-0.7	-8.6
-4	516.4	513.7	0.9948	505.8	0.9795	-2.7	-10.6
-3.5	516.1	513.7	0.9953	505.8	0.9800	-2.4	-10.3
-3	518.4	513.7	0.9909	505.8	0.9757	-4.7	-12.6
-2.5	519.4	513.7	0.9890	505.8	0.9738	-5.7	-13.6
-2	520	513.7	0.9879	505.8	0.9727	-6.3	-14.2
-1.5	520.5	513.7	0.9869	505.8	0.9718	-6.8	-14.7
-1	521.3	513.7	0.9854	505.8	0.9703	-7.6	-15.5
-0.5	524.7	513.7	0.9866	505.8	0.9714	-7	-14.9
0	526.2	513.7	0.9856	505.8	0.9705	-7.5	-15.4
0.5	524.4	513.7	0.9852	505.8	0.9701	-7.7	-15.6
1	520.9	513.7	0.9875	505.8	0.9723	-6.5	-14.4
1.5	520.5	513.7	0.9869	505.8	0.9718	-6.8	-14.7
2	520.1	513.7	0.9877	505.8	0.9725	-6.4	-14.3
2.5	518.6	513.7	0.9906	505.8	0.9753	-4.9	-12.8
3	518.3	513.7	0.9911	505.8	0.9759	-4.6	-12.5
3.5	517.4	513.7	0.9928	505.8	0.9776	-3.7	-11.6
4	515.4	513.7	0.9967	505.8	0.9814	-1.7	-9.6
4.5	514.2	513.7	0.9990	505.8	0.9837	-0.5	-8.4
5	512.7	513.7	1.0020	505.8	0.9865	1	-6.9
5.5	509.9	513.7	1.0075	505.8	0.9920	3.8	-4.1
6	509.9	513.7	1.0075	505.8	0.9920	3.8	-4.1
6.5	505.1	513.7	1.0170	505.8	1.0014	8.6	0.7
7	501.5	513.7	1.0243	505.8	1.0086	12.2	4.3
7.5	498.2	513.7	1.0311	505.8	1.0153	15.5	7.6
8	494.1	513.7	1.0397	505.8	1.0237	19.6	11.7
8.5	488.3	513.7	1.0520	505.8	1.0358	25.4	17.5
9	483.5	513.7	1.0625	505.8	1.0461	30.2	22.3
9.5	374.5	513.7	1.0826	505.8	1.0660	39.2	31.3
10	290.5	513.7	1.1378	505.8	1.1203	62.2	54.3
10.5	258.7	513.7	1.3895	505.8	1.3681	144	136.1
11	200.8	513.7	1.8626	505.8	1.8339	237.9	230
11.5	111.8	513.7	2.6783	505.8	2.6371	321.9	314
12	80.1	513.7	4.9825	505.8	4.9059	410.6	402.7
12.5	59.09	513.7	8.6935	505.8	8.5598	454.61	446.71

Table 8: Block field scanning 10cm×10cm field size

Distance from Central axis in cm	Dose in mR/min	Dose at A point	Ratio A point vs scan	Dose at B point	Ratio B point vs scan	Deviation A point vs scan	Deviation B point vs scan
-10	9.9	31.86	3.218182	125.1	12.63636	21.96	115.2
-9.5	10.86	31.86	2.933702	125.1	11.51934	21	114.24
-9	12.18	31.86	2.615764	125.1	10.27094	19.68	112.92
-8.5	13.56	31.86	2.349558	125.1	9.225664	18.3	111.54
-8	15.81	31.86	2.01518	125.1	7.912713	16.05	109.29
-7.5	18.9	31.86	1.685714	125.1	6.619048	12.96	106.2
-7	25.63	31.86	1.243075	125.1	4.880999	6.23	99.47
-6.5	30.87	31.86	1.03207	125.1	4.052478	0.99	94.23
-6	55.35	31.86	0.57561	125.1	2.260163	-23.49	69.75
-5.5	100.2	31.86	0.317964	125.1	1.248503	-68.34	24.9
-5	138.9	31.86	0.229374	125.1	0.900648	-107.04	-13.8
-4.5	173.5	31.86	0.183631	125.1	0.721037	-141.64	-48.4
-4	177.4	31.86	0.179594	125.1	0.705186	-145.54	-52.3
-3.5	153.3	31.86	0.207828	125.1	0.816047	-121.44	-28.2
-3	112.1	31.86	0.284211	125.1	1.115968	-80.24	13
-2.5	60.99	31.86	0.522381	125.1	2.051156	-29.13	64.11
-2	28.24	31.86	1.128187	125.1	4.429887	3.62	96.86
-1.5	28.22	31.86	1.128987	125.1	4.433026	3.64	96.88
-1	28.22	31.86	1.128987	125.1	4.433026	3.64	96.88
-0.5	28.2	31.86	1.129787	125.1	4.43617	3.66	96.9
0	28.14	31.86	1.132196	125.1	4.445629	3.72	96.96
0.5	28.14	31.86	1.132196	125.1	4.445629	3.72	96.96
1	28.22	31.86	1.128987	125.1	4.433026	3.64	96.88
1.5	28.21	31.86	1.129387	125.1	4.434598	3.65	96.89
2	28.25	31.86	1.127788	125.1	4.428319	3.61	96.85
2.5	60.98	31.86	0.522466	125.1	2.051492	-29.12	64.12
3	112.11	31.86	0.284185	125.1	1.115868	-80.25	12.99
3.5	153.3	31.86	0.207828	125.1	0.816047	-121.44	-28.2
4	177.3	31.86	0.179695	125.1	0.705584	-145.44	-52.2
4.5	173.44	31.86	0.183695	125.1	0.721287	-141.58	-48.34
5	138.9	31.86	0.229374	125.1	0.900648	-107.04	-13.8
5.5	100.2	31.86	0.317964	125.1	1.248503	-68.34	24.9
6	55.35	31.86	0.57561	125.1	2.260163	-23.49	69.75
6.5	30.87	31.86	1.03207	125.1	4.052478	0.99	94.23
7	25.65	31.86	1.242105	125.1	4.877193	6.21	99.45
7.5	20.41	31.86	1.561	125.1	6.129348	11.45	104.69
8	17.79	31.86	1.790894	125.1	7.03204	14.07	107.31
8.5	13.56	31.86	2.349558	125.1	9.225664	18.3	111.54
9	12.75	31.86	2.498824	125.1	9.811765	19.11	112.35
9.5	10.25	31.86	3.108293	125.1	12.20488	21.61	114.85
10	9.81	31.86	3.247706	125.1	12.75229	22.05	115.29

Table 9: Block field scanning 15cm×15cm field size

Distance from central axis in cm	Block field dose in mR/min	Dose at A point	Ratoi A point vs scan	Dose at B point	Ratoi B point vs scan	Deviation A point vs scan	Deviation B point vs scan
-10	38.32	52.72	1.375783	301.8	7.875783	14.4	263.48
-9.5	46.65	52.72	1.130118	301.8	6.469453	6.07	255.15
-9	71.85	52.72	0.733751	301.8	4.200418	-19.13	229.95
-8.5	131.3	52.72	0.401523	301.8	2.298553	-78.58	170.5
-8	209.3	52.72	0.251887	301.8	1.441949	-156.58	92.5
-7.5	304.7	52.72	0.173023	301.8	0.990482	-251.98	-2.9
-7	382	52.72	0.13801	301.8	0.790052	-329.28	-80.2
-6.5	425.9	52.72	0.123785	301.8	0.708617	-373.18	-124.1
-6	429.8	52.72	0.122662	301.8	0.702187	-377.08	-128
-5.5	378.7	52.72	0.139213	301.8	0.796937	-325.98	-76.9
-5	317.1	52.72	0.166257	301.8	0.95175	-264.38	-15.3
-4.5	252.3	52.72	0.208958	301.8	1.196195	-199.58	49.5
-4	228.3	52.72	0.230924	301.8	1.321945	-175.58	73.5
-3.5	198.2	52.72	0.265994	301.8	1.522704	-145.48	103.6
-3	154.4	52.72	0.341451	301.8	1.954663	-101.68	147.4
-2.5	98.43	52.72	0.535609	301.8	3.066138	-45.71	203.37
-2	49.72	52.72	1.060338	301.8	6.069992	3	252.08
-1.5	49.42	52.72	1.066775	301.8	6.106839	3.3	252.38
-1	49.32	52.72	1.068938	301.8	6.119221	3.4	252.48
-0.5	49.3	52.72	1.069371	301.8	6.121704	3.42	252.5
0	49.29	52.72	1.069588	301.8	6.122946	3.43	252.51
0.5	49.21	52.72	1.071327	301.8	6.1329	3.51	252.59
1	49.4	52.72	1.067206	301.8	6.109312	3.32	252.4
1.5	49.42	52.72	1.066775	301.8	6.106839	3.3	252.38
2	49.72	52.72	1.060338	301.8	6.069992	3	252.08
2.5	90.33	52.72	0.583638	301.8	3.341083	-37.61	211.47
3	138.6	52.72	0.380375	301.8	2.177489	-85.88	163.2
3.5	184.7	52.72	0.285436	301.8	1.634001	-131.98	117.1
4	219.3	52.72	0.240401	301.8	1.376197	-166.58	82.5
4.5	246.8	52.72	0.213614	301.8	1.222853	-194.08	55
5	290.6	52.72	0.181418	301.8	1.038541	-237.88	11.2
5.5	365.2	52.72	0.144359	301.8	0.826396	-312.48	-63.4
6	425.9	52.72	0.123785	301.8	0.708617	-373.18	-124.1
6.5	433.9	52.72	0.121503	301.8	0.695552	-381.18	-132.1
7	417.6	52.72	0.126245	301.8	0.722701	-364.88	-115.8
7.5	351	52.72	0.150199	301.8	0.859829	-298.28	-49.2
8	277.6	52.72	0.189914	301.8	1.087176	-224.88	24.2
8.5	190	52.72	0.277474	301.8	1.588421	-137.28	111.8
9	107.1	52.72	0.49225	301.8	2.817927	-54.38	194.7
9.5	58.32	52.72	0.903978	301.8	5.174897	-5.6	243.48
10	43.71	52.72	1.206131	301.8	6.904598	9.01	258.09

Table 10: Block field scanning 20cm×20cm field size

Distance from central axis in cm	Dose in mR/min	Dose at A point	Ratio A point vs scan	Dose at B point	Ratio B point vs scan	Deviation A point vs scan	Deviation B point vs scan
-12.5	55.71	74.31	1.333872	274.4	4.925507	18.6	218.69
-12	65.8	74.31	1.129331	274.4	4.170213	8.51	208.6
-11.5	103.5	74.31	0.717971	274.4	2.651208	-29.19	170.9
-11	193.5	74.31	0.384031	274.4	1.418088	-119.19	80.9
-10.5	286.1	74.31	0.259734	274.4	0.959105	-211.79	-11.7
-10	375.3	74.31	0.198002	274.4	0.731148	-300.99	-100.9
-9.5	437.5	74.31	0.169851	274.4	0.6272	-363.19	-163.1
-9	459.2	74.31	0.161825	274.4	0.597561	-384.89	-184.8
-8.5	463	74.31	0.160497	274.4	0.592657	-388.69	-188.6
-8	467.4	74.31	0.158986	274.4	0.587077	-393.09	-193
-7.5	469	74.31	0.158443	274.4	0.585075	-394.69	-194.6
-7	469.4	74.31	0.158308	274.4	0.584576	-395.09	-195
-6.5	466.4	74.31	0.159327	274.4	0.588336	-392.09	-192
-6	455.2	74.31	0.163247	274.4	0.602812	-380.89	-180.8
-5.5	406	74.31	0.18303	274.4	0.675862	-331.69	-131.6
-5	328.2	74.31	0.226417	274.4	0.836076	-253.89	-53.8
-4.5	273.5	74.31	0.2717	274.4	1.003291	-199.19	0.9
-4	242.2	74.31	0.306813	274.4	1.132948	-167.89	32.2
-3.5	207.6	74.31	0.357948	274.4	1.321773	-133.29	66.8
-3	161.1	74.31	0.461266	274.4	1.70329	-86.79	113.3
-2.5	105.9	74.31	0.7017	274.4	2.591124	-31.59	168.5
-2	70.8	74.31	1.049576	274.4	3.875706	3.51	203.6
-1.5	63.91	74.31	1.162729	274.4	4.293538	10.4	210.49
-1	62.48	74.31	1.189341	274.4	4.391805	11.83	211.92
-0.5	62.28	74.31	1.19316	274.4	4.405909	12.03	212.12
0	62.28	74.31	1.19316	274.4	4.405909	12.03	212.12
0.5	62.28	74.31	1.19316	274.4	4.405909	12.03	212.12
1	62.48	74.31	1.189341	274.4	4.391805	11.83	211.92
1.5	63.91	74.31	1.162729	274.4	4.293538	10.4	210.49
2	70.8	74.31	1.049576	274.4	3.875706	3.51	203.6
2.5	105.9	74.31	0.7017	274.4	2.591124	-31.59	168.5
3	161.1	74.31	0.461266	274.4	1.70329	-86.79	113.3
3.5	207.6	74.31	0.357948	274.4	1.321773	-133.29	66.8
4	242.2	74.31	0.306813	274.4	1.132948	-167.89	32.2
4.5	273.5	74.31	0.2717	274.4	1.003291	-199.19	0.9
5	328.3	74.31	0.226348	274.4	0.835821	-253.99	-53.9
5.5	406	74.31	0.18303	274.4	0.675862	-331.69	-131.6
6	455.2	74.31	0.163247	274.4	0.602812	-380.89	-180.8
6.5	466.4	74.31	0.159327	274.4	0.588336	-392.09	-192
7	469.5	74.31	0.158275	274.4	0.584452	-395.19	-195.1
7.5	469	74.31	0.158443	274.4	0.585075	-394.69	-194.6
8	467.4	74.31	0.158986	274.4	0.587077	-393.09	-193
8.5	463	74.31	0.160497	274.4	0.592657	-388.69	-188.6
9	459.2	74.31	0.161825	274.4	0.597561	-384.89	-184.8
9.5	437.5	74.31	0.169851	274.4	0.6272	-363.19	-163.1
10	375.3	74.31	0.198002	274.4	0.731148	-300.99	-100.9
10.5	286.2	74.31	0.259644	274.4	0.95877	-211.89	-11.8
11	193.5	74.31	0.384031	274.4	1.418088	-119.19	80.9
11.5	103.5	74.31	0.717971	274.4	2.651208	-29.19	170.9
12	65.9	74.31	1.127618	274.4	4.163885	8.41	208.5
12.5	55.71	74.31	1.333872	274.4	4.925507	18.6	218.69

Table 11: Block field scanning 25cm×25cm field size

Distance from Central axis in cm	Dose in mR/min	Dose at A point	Ratio A point vs scan	Dose at B point	Ratio B point vs scan	Deviation A point vs scan	Deviation B point vs scan
-12.5	425.4	101	0.2374236	367.3	0.8634227	-324.4	-58.1
-12	460.8	101	0.219184	367.3	0.797092	-359.8	-93.5
-11.5	469.5	101	0.2151225	367.3	0.7823216	-368.5	-102.2
-11	476.5	101	0.2119622	367.3	0.770829	-375.5	-109.2
-10.5	480.4	101	0.2102415	367.3	0.7645712	-379.4	-113.1
-10	484.4	101	0.2085054	367.3	0.7582576	-383.4	-117.1
-9.5	486.9	101	0.2074348	367.3	0.7543643	-385.9	-119.6
-9	489	101	0.206544	367.3	0.7511247	-388	-121.7
-8.5	490.4	101	0.2059543	367.3	0.7489804	-389.4	-123.1
-8	490.7	101	0.2058284	367.3	0.7485225	-389.7	-123.4
-7.5	490.4	101	0.2059543	367.3	0.7489804	-389.4	-123.1
-7	488.4	101	0.2067977	367.3	0.7520475	-387.4	-121.1
-6.5	484.1	101	0.2086346	367.3	0.7587275	-383.1	-116.8
-6	471.9	101	0.2140284	367.3	0.7783429	-370.9	-104.6
-5.5	413.1	101	0.2444929	367.3	0.889131	-312.1	-45.8
-5	335.8	101	0.3007743	367.3	1.0938058	-234.8	31.5
-4.5	281.1	101	0.3593027	367.3	1.3066524	-180.1	86.2
-4	252.2	101	0.4004758	367.3	1.4563838	-151.2	115.1
-3.5	216.5	101	0.4665127	367.3	1.6965358	-115.5	150.8
-3	161.5	101	0.625387	367.3	2.2743034	-60.5	205.8
-2.5	108.5	101	0.9308756	367.3	3.3852535	-7.5	258.8
-2	83.04	101	1.2162813	367.3	4.4231696	17.96	284.26
-1.5	77.01	101	1.311518	367.3	4.7695105	23.99	290.29
-1	74.49	101	1.3558867	367.3	4.9308632	26.51	292.81
-0.5	73.38	101	1.3763968	367.3	5.0054511	27.62	293.92
0	73.32	80.58	1.099018	367.3	5.0095472	7.26	293.98
0.5	73.38	80.58	1.0981194	305	4.1564459	7.2	231.62
1	74.49	80.58	1.0817559	305	4.0945093	6.09	230.51
1.5	77.01	80.58	1.0463576	305	3.9605246	3.57	227.99
2	83.04	80.58	0.9703757	305	3.6729287	-2.46	221.96
2.5	108.5	80.58	0.7426728	305	2.8110599	-27.92	196.5
3	161.5	80.58	0.4989474	305	1.8885449	-80.92	143.5
3.5	216.5	80.58	0.372194	305	1.408776	-135.92	88.5
4	252.2	80.58	0.3195083	305	1.2093577	-171.62	52.8
4.5	281.1	80.58	0.2866596	305	1.0850231	-200.52	23.9
5	335.8	80.58	0.2399643	305	0.9082787	-255.22	-30.8
5.5	413.1	80.58	0.1950617	305	0.73832	-332.52	-108.1
6	471.9	80.58	0.1707565	305	0.6463234	-391.32	-166.9
6.5	484.1	80.58	0.1664532	305	0.6300351	-403.52	-179.1
7	488.4	80.58	0.1649877	305	0.6244881	-407.82	-183.4
7.5	490.4	80.58	0.1643148	305	0.6219413	-409.82	-185.4
8	490.7	80.58	0.1642144	305	0.621561	-410.12	-185.7
8.5	490.4	80.58	0.1643148	305	0.6219413	-409.82	-185.4
9	489	80.58	0.1647853	305	0.6237219	-408.42	-184
9.5	486.9	80.58	0.165496	305	0.626412	-406.32	-181.9
10	484.4	80.58	0.1663501	305	0.6296449	-403.82	-179.4
10.5	480.4	80.58	0.1677352	305	0.6348876	-399.82	-175.4
11	476.5	80.58	0.1691081	305	0.6400839	-395.92	-171.5
11.5	469.5	80.58	0.1716294	305	0.6496273	-388.92	-164.5
12	460.8	80.58	0.1748698	305	0.6618924	-380.22	-155.8
12.5	425.4	80.58	0.1894217	305	0.7169723	-344.82	-120.4

Table 12: Distance vs attenuation 10cm×10cm field size

Distance from Central axis in cm	Open field dose in mR/min	Block field dose in mR/min	Attenuation for use block	Attenuation percentage
-10	14.16	9.9	4.26	30.0847458
-9.5	16.08	10.86	5.22	32.4626866
-9	18.18	12.18	6	33.0033003
-8.5	21.54	13.56	7.98	37.0473538
-8	25.44	15.81	9.63	37.8537736
-7.5	30.2	18.9	11.3	37.4172185
-7	32.41	19.93	12.48	38.5066338
-6.5	51.99	30.87	21.12	40.6231968
-6	98.76	55.35	43.41	43.9550425
-5.5	184.1	100.2	83.9	45.5730581
-5	274.1	138.9	135.2	49.3250638
-4.5	382.4	173.5	208.9	54.6286611
-4	447.5	177.4	270.1	60.3575419
-3.5	467.9	153.3	314.6	67.236589
-3	475.4	112.1	363.3	76.419857
-2.5	479.3	60.99	418.31	87.275193
-2	482.1	23.24	458.86	95.1794234
-1.5	483.8	23.22	460.58	95.2004961
-1	485.1	23.22	461.88	95.2133581
-0.5	486	23.2	462.8	95.2263374
0	485.9	23.14	462.76	95.2377032
0.5	486.1	23.14	462.96	95.2396626
1	485.01	23.22	461.79	95.2124698
1.5	483.7	23.21	460.49	95.2015712
2	482	23.25	458.75	95.1763485
2.5	479.3	60.98	418.32	87.2772794
3	475.5	112.11	363.39	76.4227129
3.5	467.8	153.3	314.5	67.2295853
4	447.4	177.3	270.1	60.3710326
4.5	382.4	173.44	208.96	54.6443515
5	274	138.9	135.1	49.3065693
5.5	184.1	100.2	83.9	45.5730581
6	98.76	55.35	43.41	43.9550425
6.5	51.99	30.87	21.12	40.6231968
7	37.43	25.65	11.78	31.4720812
7.5	31.31	20.41	10.9	34.8131587
8	25.46	17.79	7.67	30.1256874
8.5	24.51	13.56	10.95	44.6756426
9	20.7	12.75	7.95	38.4057971
9.5	17.79	10.25	7.54	42.3833614
10	15.54	9.81	5.73	36.8725869

Table 12: Distance vs attenuation 15cm×15cm field size

Distance from central axis in cm	Open field dose in mR/min	Block field dose in mR/min	Attenuation for use block	Attenuation for percentage
-10	45.57	38.32	7.25	15.91
-9.5	56.19	46.65	9.54	16.98
-9	81.96	71.85	10.11	12.34
-8.5	146.3	131.3	15	10.25
-8	237.8	209.3	28.5	11.98
-7.5	342.3	304.7	37.6	10.98
-7	417.1	382	35.1	8.42
-6.5	462.4	425.9	36.5	7.89
-6	472.9	429.8	43.1	9.11
-5.5	479.4	378.7	100.7	21.01
-5	483.4	317.1	166.3	34.40
-4.5	487	252.3	234.7	48.19
-4	489.6	228.3	261.3	53.37
-3.5	492.3	198.2	294.1	59.74
-3	494.2	154.4	339.8	68.76
-2.5	495.6	98.43	397.17	80.14
-2	496.7	55.17	441.53	88.89
-1.5	497.7	50.22	447.48	89.91
-1	498.4	49.32	449.08	90.10
-0.5	498.6	49.3	449.3	90.11
0	496	49.29	446.71	90.06
0.5	496.5	49.21	447.29	90.09
1	496.6	49.4	447.2	90.05
1.5	495.7	50.24	445.46	89.86
2	495.7	55.61	440.09	88.78
2.5	494.9	90.33	404.57	81.75
3	493.7	138.6	355.1	71.93
3.5	492.1	184.7	307.4	62.47
4	489.7	219.3	270.4	55.22
4.5	487.2	246.8	240.4	49.34
5	484.2	290.6	193.6	39.98
5.5	480.1	365.2	114.9	23.93
6	475.6	425.9	49.7	10.45
6.5	468.6	433.9	34.7	7.41
7	454	417.6	36.4	8.02
7.5	388.9	351	37.9	9.75
8	306.2	277.6	28.6	9.34
8.5	218.4	190	28.4	13.00
9	128.4	107.1	21.3	16.59
9.5	66.69	58.32	8.37	12.55
10	51.84	43.71	8.13	15.68

Table 12: Distance vs attenuation 20cm×20cm field size

Distance from central axis in cm	Open field Dose in mR/min	Block field Dose in mR/min	Attenuation for use block	Attenuation percentage
-12.5	59.37	55.71	3.66	6.16
-12	70.14	65.8	4.34	6.19
-11.5	108.4	103.5	4.9	4.52
-11	199	193.5	5.5	2.76
-10.5	292.5	286.1	6.4	2.19
-10	382	375.3	6.7	1.75
-9.5	451.7	437.5	14.2	3.14
-9	478.6	459.2	19.4	4.05
-8.5	486.3	463	23.3	4.79
-8	492.7	467.4	25.3	5.13
-7.5	496.7	469	27.7	5.58
-7	501.3	469.4	31.9	6.36
-6.5	504.7	466.4	38.3	7.59
-6	507.8	455.2	52.6	10.36
-5.5	510.3	406	104.3	20.44
-5	512.4	328.2	184.2	35.95
-4.5	514.4	273.5	240.9	46.83
-4	516.4	242.2	274.2	53.10
-3.5	516.1	207.6	308.5	59.78
-3	518.4	161.1	357.3	68.92
-2.5	519.4	105.9	413.5	79.61
-2	520	70.8	449.2	86.38
-1.5	520.5	63.91	456.59	87.72
-1	521.3	62.48	458.82	88.01
-0.5	520.7	62.28	458.42	88.04
0	521.2	62.28	458.92	88.05
0.5	520.7	62.28	458.42	88.04
1	521.2	62.48	458.72	88.01
1.5	520.5	63.91	456.59	87.72
2	520.1	70.8	449.3	86.39
2.5	519.6	105.9	413.7	79.62
3	518.3	161.1	357.2	68.92
3.5	516.1	207.6	308.5	59.78
4	516.4	242.2	274.2	53.10
4.5	514.3	273.5	240.8	46.82
5	512.5	328.3	184.2	35.94
5.5	510.3	406	104.3	20.44
6	507.9	455.2	52.7	10.38
6.5	504.6	466.4	38.2	7.57
7	501.5	469.5	32	6.38
7.5	496.7	469	27.7	5.58
8	492.6	467.4	25.2	5.12
8.5	488.3	463	25.3	5.18
9	478.5	459.2	19.3	4.03
9.5	451.6	437.5	14.1	3.12
10	382.3	375.3	7	1.83
10.5	292.5	286.2	6.3	2.15
11	199.5	193.5	6	3.01
11.5	108.4	103.5	4.9	4.52
12	70.15	65.9	4.25	6.06
12.5	59.37	55.71	3.66	6.16

Table 15: Open field vs Block field A point Ratio 10cm×10cm field size

Distance from Central axis in cm	Open field ratio A point vs scan	Block field ratio A point vs scan
-10	32.02683616	3.218181818
-9.5	28.20273632	2.933701657
-9	24.9449945	2.615763547
-8.5	21.0538533	2.349557522
-8	17.82625786	2.015180266
-7.5	15.01655629	1.685714286
-7	13.99259488	1.598595083
-6.5	8.722831314	1.032069971
-6	4.591940057	0.575609756
-5.5	2.463335144	0.317964072
-5	1.654505655	0.22937365
-4.5	1.185930962	0.183631124
-4	1.013407821	0.179594138
-3.5	0.969224193	0.207827789
-3	0.95393353	0.284210526
-2.5	0.9461715	0.522380718
-2	0.940676208	1.37091222
-1.5	0.937370814	1.372093023
-1	0.934858792	1.372093023
-0.5	0.933127572	1.373275862
0	0.933319613	1.376836646
0.5	0.93293561	1.376836646
1	0.935032267	1.372093023
1.5	0.937564606	1.372684188
2	0.940871369	1.370322581
2.5	0.9461715	0.522466382
3	0.953732913	0.284185175
3.5	0.969431381	0.207827789
4	1.013634332	0.179695431
4.5	1.185930962	0.183694649
5	1.655109489	0.22937365
5.5	2.463335144	0.317964072
6	4.591940057	0.575609756
6.5	8.722831314	1.032069971
7	12.11594977	1.242105263
7.5	14.48419035	1.56099951
8	17.81225452	1.790893761
8.5	18.50265198	2.349557522
9	21.90821256	2.498823529
9.5	25.49184935	3.108292683
10	29.18275418	3.247706422

Table 17: Open field vs Block field A point Ratio 20cm×20cm field size

Distance from central axis in cm	Open field ratio A point vs scan	Block field ratio A point vs scan
-12.5	8.652518107	1.333871836
-12	7.323923581	1.129331307
-11.5	4.738929889	0.717971014
-11	2.581407035	0.384031008
-10.5	1.756239316	0.259734359
-10	1.344764398	0.198001599
-9.5	1.137259243	0.169851429
-9	1.073338905	0.161824913
-8.5	1.056343821	0.16049676
-8	1.042622285	0.158985879
-7.5	1.034225891	0.158443497
-7	1.024735687	0.158308479
-6.5	1.017832376	0.159326758
-6	1.011618748	0.163246924
-5.5	1.006662747	0.183029557
-5	1.00253708	0.226416819
-4.5	0.998639191	0.271700183
-4	0.994771495	0.306812552
-3.5	0.995349738	0.357947977
-3	0.990933642	0.461266294
-2.5	0.989025799	0.701699717
-2	0.987884615	1.049576271
-1.5	0.986935639	1.162728837
-1	0.985421063	1.189340589
-0.5	0.986556558	1.193159923
0	0.98561013	1.193159923
0.5	0.986556558	1.193159923
1	0.98561013	1.189340589
1.5	0.986935639	1.162728837
2	0.987694674	1.049576271
2.5	0.988645112	0.701699717
3	0.991124831	0.461266294
3.5	0.995349738	0.357947977
4	0.994771495	0.306812552
4.5	0.998833366	0.271700183
5	1.002341463	0.226347853
5.5	1.006662747	0.183029557
6	1.011419571	0.163246924
6.5	1.018034086	0.159326758
7	1.024327019	0.15827476
7.5	1.034225891	0.158443497
8	1.042833942	0.158985879
8.5	1.052017203	0.16049676
9	1.073563218	0.161824913
9.5	1.137511072	0.169851429
10	1.343709129	0.198001599
10.5	1.756239316	0.259643606
11	2.574937343	0.384031008
11.5	4.738929889	0.717971014
12	7.322879544	1.127617602
12.5	8.652518107	1.333871836

Table 16: Open field vs Block field A point Ratio 15cm×15cm field size

Distance from central axis in cm	Open field ratio A point vs scan	Block field ratio A point vs scan
-10	10.82290981	1.375782881
-9.5	8.77736252	1.130117899
-9	6.017569546	0.73375087
-8.5	3.371155161	0.401523229
-8	2.074011775	0.251887243
-7.5	1.440841367	0.173022645
-7	1.182450252	0.138010471
-6.5	1.066608997	0.123784926
-6	1.042926623	0.122661703
-5.5	1.028785982	0.139213097
-5	1.020273066	0.166256701
-4.5	1.012731006	0.20895759
-4	1.007352941	0.230924223
-3.5	1.001828154	0.265993946
-3	0.997976528	0.341450777
-2.5	0.995157385	0.535609062
-2	0.992953493	0.955591807
-1.5	0.990958409	1.049780964
-1	0.989566613	1.068937551
-0.5	0.989169675	1.069371197
0	0.994354839	1.069588152
0.5	0.993353474	1.071326966
1	0.993153443	1.067206478
1.5	0.994956627	1.049363057
2	0.994956627	0.94803093
2.5	0.996564963	0.583637773
3	0.998987239	0.38037518
3.5	1.002235318	0.285435842
4	1.007147233	0.240401277
4.5	1.012315271	0.213614263
5	1.018587361	0.181417756
5.5	1.027285982	0.144359255
6	1.037005887	0.123784926
6.5	1.052496799	0.12150265
7	1.086343612	0.126245211
7.5	1.268192337	0.15019943
8	1.610711953	0.189913545
8.5	2.258241758	0.277473684
9	3.841121495	0.492250233
9.5	7.395411606	0.903978052
10	9.513888889	1.20613132

List of publication:

Alok Kumar Dey[1], M.Jahangir Alam[2] , Md. Adnan Kiber[1], S.Reza.Husain[2]
"Measuring the accuracy of dose distribution of a wedge shaped mid-line block for the treatment of cancer patients in Bangladesh." Bangladesh Journal of Medical physics, Vol.3 p45-48, 2004.

1. Department of Physics, University of Dhaka, Dhaka-1000

2. Oncology Units, Delta Medical Center Ltd., Mirpur, Dhaka